Investigation into Heating and Hyperfine Loss Mechanisms in Magnetically Trapped Ultra-Cold Rubidium

by

Chenchong Zhu

A THESIS SUBMITTED IN PARTIAL FULFILLMENT
OF THE REQUIREMENTS FOR THE DEGREE OF

Bachelor of Science

in

THE FACULTY OF SCIENCE
(Physics and Astronomy)

The University Of British Columbia
(Vancouver)

April 2010

Abstract

This thesis describes our investigation into elastic collisions between an ultra-cold, magnetically trapped atom ensemble of rubidium-87 or rubidium-85, and background, room-temperature rubidium. We investigated two specific phenomena: low scattering angle elastic collisions that change the trapped ensemble energy distribution without resulting in immediate trap loss, or "heating collisions", and the dependence of elastic collisional loss cross-sections on the hyperfine state of the trapped rubidium ensemble. A theoretical description of quantum scattering theory is given, along with how this theory can be utilized to calculate heating collision rates. A theoretical and technical description of our rubidium magnetic/magneto-optical trap follows, including descriptions of two new additions to the system: an RF coil and a Zeeman optical pumping system. We then describe the methods used to experimentally determine trap loss rates and the energy distribution in the trap. Our results show that the average rate of energy imparted to a trapped atom in our system is on the order of 1 μK per second. We also show that the Rb-Rb loss rate slope $\langle \sigma v \rangle$ is independent of hyperfine state, indicating that any loss dependency on hyperfine state rests with collisions with other species, or other forms of loss.

Revision: ubcdiss.cls r26

Table of Contents

List of Tables

List of Figures

Acknowledgments

My undergraduate thesis, and the NSERC-USRA research term that preceded and inspired it, has spanned an entire year of study and research at the Quantum Degenerate Gases laboratory. During this time, the researchers at QDG have been extremely supportive and encouraging of my work. I would like to thank Dr. Kirk Madison for his assistance with the theoretical aspects of the project, insightful observations during brainstorming, and helpful advice. I would also like Dr. James Booth for his invaluable help with experiment calibration and maintenance, control and analysis code programming assistance, and for the many thoughtful discussions over the details and ramifications of the project. Thanks also to Gabriel Dufour, who built the bulk of the numerical simulator, and participated in much of the data taking and brainstorming in the later months of the project. Thanks to Zhiying Li for using her multi-channel collision code to provide theoretical confirmation of our experimental results, and for helping me understand the operation and results of said code. Thanks to David Fagnan, who worked on this project a year before I did and whose thesis and cross-section calculation code have been invaluable resources in my work. And thanks to Janelle van Dongen, whose laser and optical table expertise has saved many an experiment from ending before they started.

Last, but not least, I would like to thank my friends and family, many of whom, in addition to providing emotional support and encouragement, provided helpful advice on everything from programming and mathematical simulation to thesis-writing.

Chapter 1

Introduction

1.1 Overview

Cold atomic and molecular physics, the study of particle behaviour at temperatures near and below 1 K, has become one of the fastest growing fields of physics. Experiments investigating, for example, Bose-Einstein condensation (BEC) and atomic spin statistics can be performed at these temperatures. The procedure of cooling and trapping atoms in order to perform these experiments is currently accomplished using several methods. Laser cooling atoms and transferring them into a position-dependent potential is one such method, and two devices based on of this procedure, the magneto-optical trap and the magnetic trap, have become ubiquitous in cold atomic physics [13, 24].

The process by which cold trapped atoms can be ejected from their traps, or trap loss, is an active area of study, important both in its relation to the study of atomic collision properties, and its relation to the application of trapped cold atoms.

This project is part of the University of British Columbia Quantum Degenerate Gases (QDG) laboratory's ongoing investigation into trapped atom loss, in collaboration with the British Columbia Institute of Technology.

1.2 Background

The magneto-optical trap (MOT) is composed of a set of laser beams and a position-dependent magnetic field acting on a vacuum housing containing trace gases. The lasers and magnetic field gradient are used to trap an ensemble of atoms from the gas, and cool them into the mK range [24]. If the lasers are subsequently turned off and the magnetic field gradient increased, then the gradient alone holds the atoms in place; this is known as a magnetic trap. A number of magnetic trap configurations exist, including the anti-Helmholtz trap and Ioffe-Pritchard trap, but all work on the principle of creating a trapping potential with a magnetic field [7, 13].

Whenever a cloud of cold atoms, known as an ensemble, is trapped in a magnetic trap or

magneto-optical trap, the cloud is subject to a number of processes that result in its constituent atoms being lost from the trap. The most prominent is collisions with background gases. The high-temperature gas from which the ensemble is drawn will remain in the system after the ensemble is trapped, as will trace amounts of other gases. Because these background gases will still be at a much higher temperature than the trapped atoms, collisions between background and trapped atoms can potentially give trapped atoms enough kinetic energy to escape the trap [14]. Interactions between the trapped atoms themselves can also result in losses, as can complex collision channels involving a number of bodies, or interaction with the cooling lasers. Under our experimental conditions, however, such losses are minor compared to collisions with background gases.

1.3 Motivation for Studying Trap Loss

Loss of atoms from traps plays an important part in cold atomic physics. In many experiments it can be a nuisance, or even an extreme hindrance. An experiment to produce a Bose-Einstein condensate, for example, requires radio frequency evaporative cooling for up to 60 seconds, and losses must not be significant over this period of time [22]. It is possible, given certain conditions, for the entire ensemble to disappear over this timescale due to various loss processes. It is for this reason that BECs are created at pressures of around 10^{-11} Torr [2]. These losses can also provide empirical insight into various areas of scattering theory. Atomic cross-sections, for example, can be deduced through magnetic or magneto-optical trap loss rates [14].

Aside from scientific insight, the magneto-optical/magnetic trap platform could also have a number of practical applications. There has been progress in miniaturizing traps, which currently have dimensions on the order of metres, by creating them on atom chips, several centimetres to a side and only millimetres thick [15]. These chips could give rise to extremely sensitive atom detectors [15, 22]. Early work also exists on utilizing these chips as quantum gates, and has led to proposals of experimental quantum processors using arrays of atom chips [9, 15, 22].

Considering that these traps have only come into common use in the last two decades, their full range of applications cannot yet be forseen. These applications will require trap loss be minimized or controlled. Atom loss, for example, is equivalent to data loss and calculation error in quantum computing devices [14, 15]. Bose-Einstein condensate-based applications will require long-lived condensates which can be continuously fabricated over short time scales. Therefore, the study of loss rates from magnetic traps can have far-reaching applications in both theory and application.

1.4 Motivation for Our Work

Over the last year, QDG has been numerically and experimentally determining the cross-section of collisions leading to trap loss between trapped rubidium and various room-temperature gases. Our experimental apparatus, delightfully named the Miniature Atom Trap (MAT), is designed to trap

^{87}Rb and ^{85}Rb in a magneto-optical or magnetic trap at background gas pressures of around 10^{-9} Torr. The apparatus is attached to a gas injection system, which is able to insert other gases, such as argon, in controlled amounts. The gas injection system allows us to investigate the loss rates of trapped ^{87}Rb or ^{85}Rb with respect to collisions with room-temperature gases.

Throughout 2008 and 2009, Fagnan *et al.* experimentally characterized and numerically determined the loss rate of ^{87}Rb due to elastic collisions with background ^{40}Ar as a function of trap potential well depth (henceforth called "trap depth" for convenience) [13, 14]. A magnetic trap was used to create traps with depths below $\sim$10 mK, and a magneto-optical trap was used to create $\sim$2000 mK traps [1]. As seen in Fig. 1.1, there is a clear contribution to the total collisional cross-section from low scattering angle quantum diffractive collisions, and as the trap depth increases past $\sim$ 10 mK the depth becomes too high for quantum diffractive collisions to contribute to trap loss. This clear relationship between experiment and numerical results beautifully verifies the quantum scattering theory used by Fagnan *et al.* (summarized and expanded upon in Chapter 2).

While experimental data does show a close match between theory and experiment, additional data taken in June of 2009 at trap depths ranging from $\sim$ 2 - 10 mK show a small systematic deviation from numerical calculations, which can be seen in Fig 1.1. Loss rates of ^{87}Rb and ^{85}Rb due to elastic collisions with background Rb were also investigated in July-August 2009 in order to produce Fig. 1.2. When the magnetically trapped $|F = 3\rangle$ ^{85}Rb hyperfine state lifetime was compared to that of $|F = 2\rangle$, $|F = 2\rangle$ had a lifetime three times longer than $|F = 3\rangle$, contrary to our theoretical predictions.

Because our numerical calculations only consider trap losses due to single-channel elastic collisions following a Lennard-Jones interaction potential, we believe these data indicate additional loss dependencies, and possibly alternative loss processes, for trapped Rb that have yet to be considered. Obtaining a complete picture of trap loss phenomena in QDG's magnetic/magneto-optical trap would be beneficial both to future experiments and to understanding trap loss in general. We, therefore, set out to investigate the properties of heating due to elastic collisions with background gases, and the nature and cause of the loss dependence on hyperfine state.

[1] At the time, it was believed that the MOT had a depth of 800 ± 300 mK; subsequent direct measurements provided corrected values of 2200 ± 300 mK for ^{87}Rb and 1800 ± 300 mK for ^{85}Rb.

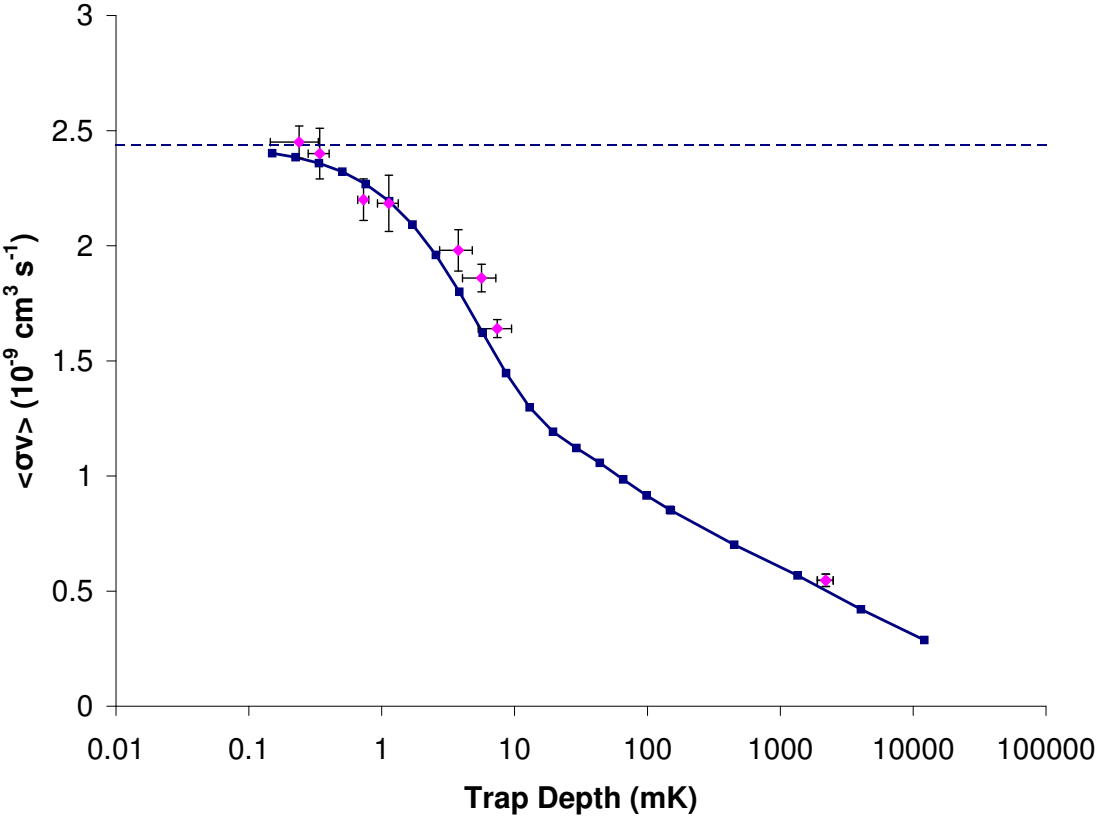

Figure 1.1: Semi-log plot of Rb-Ar $\langle \sigma v \rangle$ versus trap depth. ($\langle \sigma v \rangle$ is defined in Eq. 2.13, and is linearly proportional loss rate.) to The blue line is the numerically calculated $\langle \sigma v \rangle$, while the magenta points are experimentally determined. The blue, horizontal dashed line is the numerically calculated $\langle \sigma v \rangle$ at zero trap depth (i.e. the Boltzmann average of the total collisional cross section multiplied by v). The single point to the far right was determined using the MOT, while the magnetic trap was used for the other points to the left. The three points near 2 - 10 mK are systematically upward deviated.

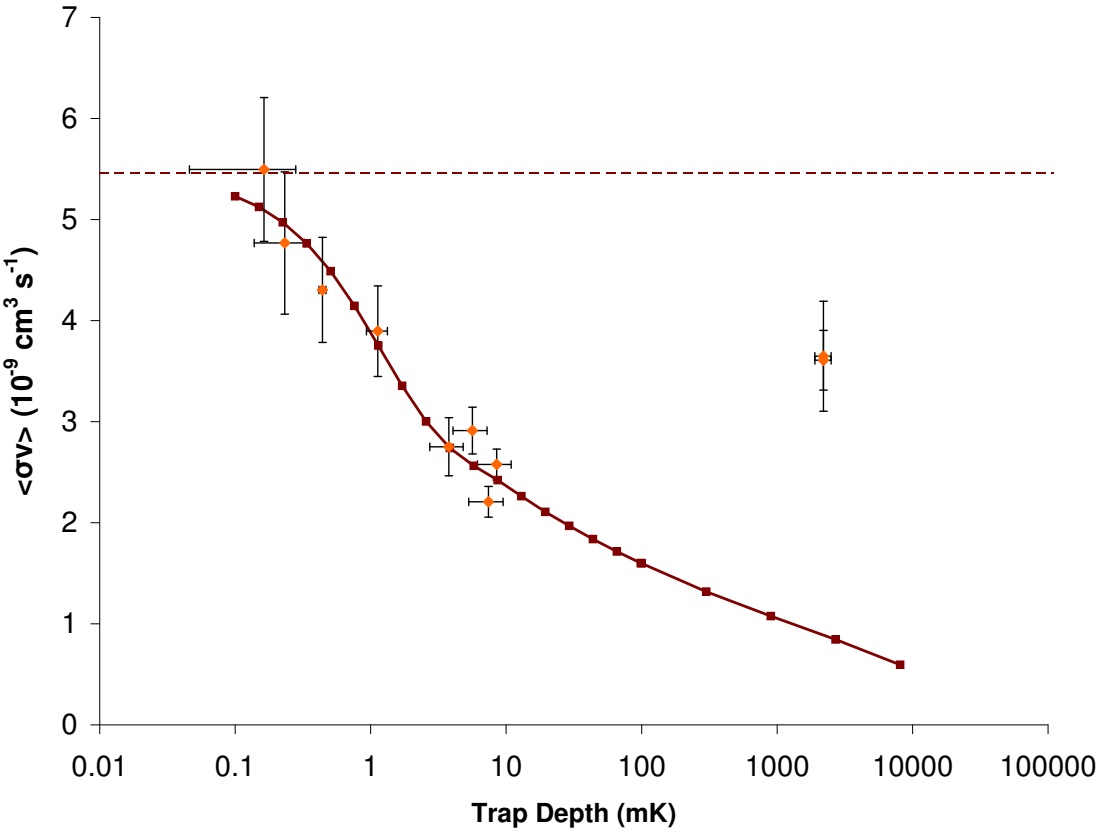

Figure 1.2: Semi-log plot of Rb-Rb $\langle\sigma v\rangle$ versus trap depth. ($\langle\sigma v\rangle$ is defined in Eq. 2.13, and is linearly proportional loss rate.) The brown line is the numerically calculated $\langle\sigma v\rangle$, while the magenta points are experimentally determined. The brown, horizontal dashed line is the numerically calculated $\langle\sigma v\rangle$ at zero trap depth (i.e. the Boltzmann average of the total collisional cross section multiplied by v). The number density of Rb is known only up to a constant scaling factor, and the experimental points were artificially rescaled using a constant scaling factor to fit on the theoretical line. Following rescaling the two follow each other closely, except for the 1800 mK MOT point, which is significantly larger than theoretical calculations. This is likely due to excited state collisions not accounted for in theory that significantly increase the value of $\langle\sigma v\rangle$.

Chapter 2

Theory

In this section, I will describe the theoretical bases for the experiments and numerical calculations completed during the course of the research project.

When a background atom collides with an atom in a magnetic trap, the centre-of-mass scattering angle may be large, in which case the collision can be approximated classically. In cases where the de Broglie wavelength associated with the momentum transfer in the collision exceeds the classical impact parameter, classical approximation is no longer valid, and we must rely on quantum scattering theory [10, 14]. Equivalently, we can consider Child's statement that approximately half of the total cross-section arises from scattering that can be found through classical analysis, while the other half arises from quantum diffractive collisions [10]. Quantum diffractive collisions correspond to low scattering angle collisions which, as we will see in Section 2.1, correspond to lower energies imparted to trapped atoms. Therefore, we must consider scattering from a quantum mechanical standpoint whenever we wish to describe low angle collisions, as we must for this thesis. I will describe only a quantum treatment of scattering theory (since it naturally reduces to classical scattering at large scattering angles).

I will frequently state position, energy, and Lennard-Jones C_6 and C_{12} coefficient values in atomic units (a.u.). These units are defined in Table 2.1 for convenience.

Table 2.1: Table of atomic units, and their equivalent SI values, from [26]. Often, a value in atomic units will simply be given the label a.u., rather than dimensions such as Bohr radii or Hartrees.

Value	Atomic Unit	Eqv. SI Value
position	Bohr radius	$5.2917720859(36) \times 10^{-11}$ m
energy	Hartree	$4.35974394(22) \times 10^{-18}$ J
C_6	Hartree Bohr^6	$9.57343447(48) \times 10^{-80}$ J m^6
C_{12}	Hartree Bohr^{12}	$2.10220253(11) \times 10^{-141}$ J m^{12}

2.1 Collision Mechanics

2.1.1 Energy Imparted to Trapped Atoms From Collisions

Assume an inbound background particle of mass m_{Bg} and laboratory frame velocity $\mathbf{v}_{Bg}$ collides with a trapped particle of mass m_t and velocity $\mathbf{v}_t$ in a MOT or magnetic trap. We introduce the reduced mass and centre of mass (CM) and relative velocities: $\mu = \frac{m_t m_{Bg}}{m_t + m_{Bg}}$, $\mathbf{V}_{CM} = \frac{m_t \mathbf{v}_t + m_{Bg}\mathbf{v}_{Bg}}{m_t + m_{Bg}}$, and $\mathbf{v}_r = \mathbf{v}_{Bg} - \mathbf{v}_t$. Denoting physical values following the collision with primes, for an elastic collision conservation of momentum gives us $\mathbf{V}_{CM} = \mathbf{V}'_{CM}$; this expression and conservation of energy gives us $|\mathbf{v}_r| = |\mathbf{v}'_r|$, i.e. the magnitude of the relative velocity stays constant [13]. Taking the angle between $\mathbf{v}_r$ and $\mathbf{v}'_r$ to be θ, the CM scattering angle, the cosine law gives [13]:

$$|\Delta\mathbf{v}_r|^2 = |\mathbf{v}_r|^2 + |\mathbf{v}'_r|^2 - 2|\mathbf{v}_r||\mathbf{v}'_r|\cos\theta = 2|\mathbf{v}_r|^2(1-\cos\theta) \tag{2.1}$$

Conservation of momentum requires that $m_t\Delta\mathbf{v}_t = -m_{Bg}\Delta\mathbf{v}_{Bg}$. If we combine this with the fact that $\Delta\mathbf{v}_t = \Delta\mathbf{v}_{Bg} - \Delta\mathbf{v}_r$, we obtain $\Delta\mathbf{v}_t = -\mu\Delta\mathbf{v}_r/m_t$. The change in kinetic energy of the trapped atom, in the lab frame, is [13]:

$$\Delta E = \frac{1}{2}m_t((\mathbf{v}_t + \Delta\mathbf{v}_t)^2 - \mathbf{v}_t^2). \tag{2.2}$$

Assuming the initial velocity of the trapped particle is around zero (or, rather, $|\Delta\mathbf{v}_t| \gg |\mathbf{v}_t|$), this gives us [13]:

$$\Delta E \approx \frac{1}{2}m_t(\Delta\mathbf{v}_t)^2 = \frac{\mu^2}{m_t}\mathbf{v}_r^2(1-cos\theta). \tag{2.3}$$

($\mathbf{v}_r^2 = \mathbf{v}\cdot\mathbf{v}$.) This is a direct relation between θ and ΔE imparted to the trapped atom in the lab frame. The minimum ΔE required to eject an atom with zero initial kinetic energy is the potential energy of the trap, U_0. This minimum energy corresponds to a minimum θ:

$$\theta_{min} = \arccos\left(1 - \frac{m_t U_0}{\mu^2|\mathbf{v}_r|^2}\right). \tag{2.4}$$

We can, of course, imagine that some atoms in the trap may begin with potential energies larger than zero. If U_s is the non-zero starting potential energy of a trapped particle, U_0 should be replaced with $\Delta U = U_0 - U_s$, and Eq. 2.4 still holds. However, the atom will then explore the volume of the trap accessible to it, then it will have non-zero kinetic energy in all regions where its (position dependent) potential energy is smaller than the atom's initial potential energy. Under these situations, particularly low angle collisions will impart velocity changes that do not obey $|\Delta\mathbf{v}_t| \gg |\mathbf{v}_t|$. The same would be true if the atoms in the trap begin with a significant amount of kinetic energy.

Table 2.2: A table of calculated CM and laboratory frame scattering angles for Rb-Ar collisions. Energy scale is the energy imparted to the trapped atom (U). θ is CM scattering angle, and Θ is laboratory frame scattering angle. All values were calculated assuming background Ar has an initial velocity $\mathbf{v}_{Bg}$ = 353.09 m/s (most probable velocity at 300 K).

Energy Scale (mK)	θ (rads)	$\Delta\mathbf{v}_{Bg}$ (m/s)	Θ (rads)
0.1	0.001243	0.2039	7.172×10^{-7}
1	0.003931	0.6447	7.163×10^{-6}
10	0.01243	2.039	7.135×10^{-5}
100	0.03931	6.447	7.046×10^{-4}
1000	0.1244	20.39	6.774×10^{-3}

2.1.2 Determining Laboratory Frame Scattering Angle

We may also convert the CM deflection angle θ into a laboratory frame deflection angle Θ. If we combine $m_t\Delta\mathbf{v}_t = -m_{Bg}\Delta\mathbf{v}_{Bg}$ and $\Delta\mathbf{v}_t = \Delta\mathbf{v}_{Bg} - \Delta\mathbf{v}_r$, we can obtain $\Delta\mathbf{v}_{Bg} = \mu\Delta\mathbf{v}_r/m_{Bg}$. We may set up a coordinate system such that all vectors lie in the xy-plane and $\mathbf{v}_r$ lies on the x-axis. Then,

$$\Delta\mathbf{v}_{Bg} = \frac{\mu}{m_{Bg}}|\Delta\mathbf{v}_r|(\cos\theta\mathbf{i} + \sin\theta\mathbf{j}), \tag{2.5}$$

where $|\Delta\mathbf{v}_r|$ is given by Eq. 2.1. We may switch to the laboratory frame by subtracting $\mathbf{V}_{CM}$ from all values of velocity, and due to our choice of coordinates $\mathbf{V}_{CM}$ lines entirely along the x-axis (this means $\mathbf{v}_{Bg}$ lies along the x-axis in the laboratory frame). Because the shift to the centre of mass frame is a Galilean transform, changes in velocity are unaffected. Therefore, Eq. 2.5 also describes the change in $\mathbf{v}_{Bg}$ in the laboratory frame. Since we know $\mathbf{v}_{Bg}$ and $\mathbf{v}'_{Bg}$, we can determine the scattering angle in the laboratory frame:

$$\Theta = \arctan\frac{|\Delta\mathbf{v}_{Bg}|\sin\theta}{|\Delta\mathbf{v}_{Bg}|\cos\theta + |\mathbf{v}_{Bg}|}, \tag{2.6}$$

where θ is given by $\theta = \arccos(1 - m_t U/\mu^2\mathbf{v}_{Bg}^2)$ (a restatement of Eq. 2.4, where U is the energy given to the trapped atom by the collision) and $\Delta\mathbf{v}_{Bg}$ by Eq. 2.5. Some sample calculations can be found in Tables 2.2 and 2.3. They use the most probable velocity for a particle in a Maxwell-Boltzmann distribution of a certain temperature: $v_{most\ probable} = \sqrt{2k_BT/m}$.

The CM scattering angles can be compared to the first diffraction minimum of the scattering. The reduced mass μ travelling with relative velocity $\mathbf{v}_r$ has a de Broglie wavelength of $\lambda = h/\mu|\mathbf{v}_r|$. The first diffraction minimum is given by

$$\theta_{diff} = \arcsin(1.22\frac{\lambda}{d}) \tag{2.7}$$

We can estimate diameter d by assuming that the scattering target is a sphere, or $\sigma_{total} = \pi d^2/4$, which gives us $d = \sqrt{4\sigma/\pi}$. How σ_{total} may be calculated is given in Section 2.2 and Section 2.4.1.

Table 2.3: A table of calculated CM and laboratory frame scattering angles for Rb-Rb collisions. Energy scale is the energy imparted to the trapped atom (U). θ is CM scattering angle, and Θ is laboratory frame scattering angle. All values were calculated assuming background Rb has an initial velocity $\mathbf{v}_{Bg}$ = 239.42 m/s (most probable velocity at 300 K).

Energy Scale (mK)	θ (rads)	$\Delta\mathbf{v}_{Bg}$ (m/s)	Θ (rads)
0.1	0.001155	0.1382	6.663×10^{-7}
1	0.003651	0.4371	6.655×10^{-6}
10	0.01155	1.3823	6.628×10^{-5}
100	0.03652	4.3711	6.546×10^{-4}
1000	0.1155	13.8228	6.294×10^{-3}

Table 2.4: A table presenting estimated values for the CM θ_{diff} of Rb-Ar and Rb-Rb collisions, calculated using Eq. 2.7. The de Broglie wavelength calculated assumes the CM relative velocity in the collision is given by $v_{most\ probable} = \sqrt{2k_BT/m_{Bg}}$, where T = 300 K. σ_{total} is estimated from $\langle\sigma_{total}v\rangle / v_{mean}$, where $v_{mean} = \sqrt{8k_BT/\pi m_{Bg}}$ (T = 300 K).

Collision	de Broglie Wavelength (m)	σ_{total} (m^2)	First Diffraction Minimum (rads)
Rb-Ar	2.8×10^{-11}	6.1×10^{-18}	0.012
Rb-Rb	2.0×10^{-11}	2.0×10^{-17}	0.0047

An estimate of the first diffraction minimum is given in Table 2.4.

2.2 Rate Equations

The rate at which a background flux of atoms, all at some velocity $\mathbf{v}_{Bg}$, is scattered into some angle $d\Omega$ due to a collision with a single trapped Rb atom is (see Fig. 2.1):

$$d(\mathbf{v}_{Bg}) = n_{Bg}|\mathbf{v}_{Bg}|\frac{d\sigma}{d\Omega}d\Omega. \tag{2.8}$$

$n_{Bg}|\mathbf{v}_{Bg}|$ represents an incoming flux of background atoms, and $\frac{d\sigma}{d\Omega}$ is the differential cross-section, the fraction of cross-section that results in incoming particles scattering into some $d\Omega$. $d\Omega$ is specified by two scattering angles: inclination angle θ and azimuthal angle ϕ.

We assume a Lennard-Jones potential for our scattering, given by

$$V = \frac{C_{12}}{r^{12}} - \frac{C_6}{r^6}, \tag{2.9}$$

with a C_6 value of 280 atomic units for Rb-Ar collisions, and 4430 for Rb-Rb collisions, cited from Bali *et al.* [3]. The fact this potential is central makes scattering symmetric about ϕ. Integrating $d\sigma$ over all applicable solid angles, we obtain the total elastic collision rate,

$$S(\mathbf{v}_{Bg}) = n_{Bg}|\mathbf{v}_{Bg}|\sigma_{total} = 2\pi n_{Bg}|\mathbf{v}_{Bg}|\int_0^\pi \sin(\theta)\frac{d\sigma}{d\Omega}d\theta, \tag{2.10}$$

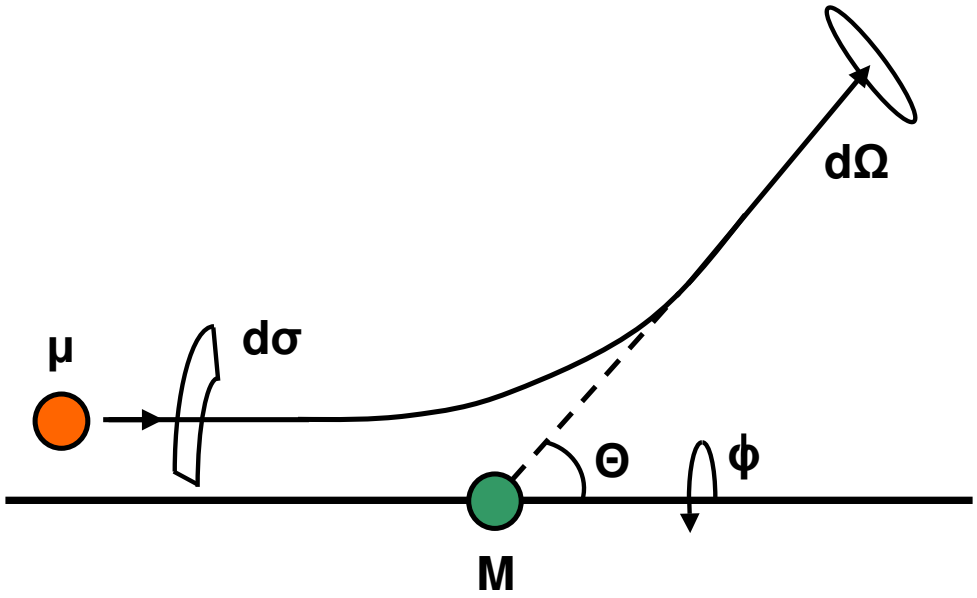

Figure 2.1: A schematic of classical scattering in the centre of mass frame, useful for understanding the terms used in quantum scattering rates. The reduced mass (μ, in orange) with some impact parameter passes through an incident area $d\sigma$, and is scattered by the centre mass (M, in teal) into some solid angle $d\Omega$, defined by two scattering angles: inclination angle θ and azimuthal angle ϕ. In our system, the scattering caused by M is modelled by a Lennard-Jones interaction potential, and because this potential is central, the scattering is symmetrical about ϕ.

where wavevector $k = \mu|\mathbf{v}_r|/\hbar$. If we instead wanted to determine the rate at which atoms are lost in the trap, we must only include collisions with scattering angles larger than θ_{min}, the minimum scattering angle of a collision that results in trap loss. This value, the rate at which background atoms collide with a single particle to produce trap loss, is

$$\Gamma(\mathbf{v}_{Bg}) = 2\pi n_{Bg}|\mathbf{v}_{Bg}| \int_{\theta_{min}}^{\pi} \sin(\theta)\frac{d\sigma}{d\Omega}d\theta = n_{Bg}|\mathbf{v}_{Bg}|\sigma(\mathbf{v}_{Bg}). \tag{2.11}$$

It is implicit in this equation that the trapped atom has negligible kinetic energy. σ is the loss cross section,

$$\sigma(\mathbf{v}_{Bg}) = 2\pi \int_{\theta_{min}}^{\pi} \sin(\theta) \frac{d\sigma}{d\Omega} d\theta, \tag{2.12}$$

and will be denoted σ instead of σ_{loss} in the rest of this work for the sake of brevity.

If our background gas has a thermal distribution of velocities, we must average $\Gamma(\mathbf{v}_{Bg})$ over the Maxwell-Boltzmann distribution. Defining (for brevity) $v \equiv |\mathbf{v}_{Bg}|$:

$$\langle \Gamma \rangle = n_{Bg} \langle \sigma v \rangle = 4\pi n_{Bg} \int_0^{\infty} v^3 \sigma(v) (\frac{m_{Bg}}{2\pi k_B T})^{3/2} exp(-\frac{m_{Bg} v^2}{2k_B T}) dv. \tag{2.13}$$

This is the Boltzmann-averaged trap loss rate given one background species. For multiple background species, we must sum up all individual Γ:

$$\langle \Gamma_{total} \rangle = \sum_{all\, species} \langle \Gamma_i \rangle = \sum_{all\, species} n_i \langle \sigma v \rangle_i . \tag{2.14}$$

Assuming no other loss mechanisms, such as Majorana losses or intra-ensemble collisions, the rate at which atoms are lost in the trap is

$$\frac{dN}{dt} = -\langle \Gamma_{total} \rangle N, \tag{2.15}$$

which is trivial to integrate to

$$N(t) = N_0 \exp(-\langle \Gamma_{total} \rangle t). \tag{2.16}$$

Therefore, we may experimentally determine $\langle \Gamma_{total} \rangle$ by determining N as a function of t and fitting an exponential decay to the result. In later sections, I will refer to $\langle \Gamma_{total} \rangle$ as Γ for brevity. If we wished to determine the loss rate due to a single species of gas, we may do this by measuring $\langle \Gamma_{total} \rangle$ as a function of n_i, the background number density of a single species of gas. Eq. 2.11 predicts a linear relationship between the two values, the slope of the relationship being $\langle \sigma v \rangle_i$. In general, n_{Bg} is an experimentally controlled property of the system. Therefore, it is more useful to quote $\langle \sigma v \rangle$ values than $\langle \Gamma \rangle$. I will commonly, then, just quote $\langle \sigma v \rangle$.

2.3 Trapped Atom Heating

While only those collisions with CM scattering angles larger than θ_{min} result in immediate trap loss, all collisions will impart kinetic energy to trapped atoms. Because the kinetic energy of the trapped atoms are being changed, the trap's effective temperature is being changed, and therefore this effect is often referred to as "heating" [3, 4]. If we assume all atoms initially have no kinetic energy, the rate of collisions, between a trapped particle and a background flux of atoms of some given velocity, that do not (immediately) result in trap loss is

$$Q(\mathbf{v}_{Bg}) = 2\pi n_{Bg}|\mathbf{v}_{Bg}| \int_0^{\theta_{min}} \sin(\theta)\frac{d\sigma}{d\Omega}d\theta. \tag{2.17}$$

(Compare this with Eq. 2.11.) This can also be averaged over a Maxwell-Boltzmann distribution to determine the velocity-averaged heating collision rate. Note that if we define

$$q = 2\pi \int_0^{\theta_{min}} \sin(\theta)\frac{d\sigma}{d\Omega}d\theta \tag{2.18}$$

and compare this to the definitions of σ and σ_{total} (Eqs. 2.10 and 2.12), we obtain:

$$\sigma_{total} = \sigma + q \tag{2.19}$$

We are, in particular, concerned with how much energy is actually being imparted to the atom. This "heating rate" is given simply by:

$$\frac{dE}{dt}(\mathbf{v}_{Bg}) = 2\pi n_{Bg}|\mathbf{v}_{Bg}| \int_0^{\theta_{min}} \Delta E \sin(\theta)\frac{d\sigma}{d\Omega}d\theta, \tag{2.20}$$

where ΔE is given by Eq. 2.3 [3, 4]. Unfortunately, this estimate can only be used in situations where all the atoms have no kinetic energy and the same potential energy, and therefore is only a good estimate over short periods of time. If it were the case that all atoms had no kinetic energy and the same potential energy at some time t_0, it would soon no longer be the case due to all the heating collisions! By "short" periods, I mean a period of time where the average number of collisions experienced by a single atom is less than 1.

In our traps, it is never the case that all the atoms have negligible kinetic energy and identical potential energies, and therefore Eqs. 2.17 and 2.20 cannot be used. Instead, we are planning for heating rates to be calculated by a numerical simulator that keeps track of the kinetic and potential energies of the trapped atoms, and handles collisions for each trapped atom individually, in accordance with the probabilistic interpretation of $\frac{d\sigma}{d\Omega}$.

2.4 Scattering Amplitude

We now attempt to determine the elastic scattering $\frac{d\sigma}{d\Omega}$. I will use the standard method and terminology found in a number of sources, and I will only summarize the procedure to arrive at $\frac{d\sigma}{d\Omega}$. For more details, consult [10, 13, 16, 23].

2.4.1 Determining the Scattering Amplitude

In CM coordinates, the three-dimensional Schrödinger equation can be written as (M is the total mass of the entire system):

$$(\nabla_r^2 + k^2 - U(\mathbf{r}_r, t))\psi = 0, \tag{2.21}$$

where $k = \sqrt{2mE}/\hbar = \mu|\mathbf{v}_r|/\hbar$ and $U = 2\mu V/\hbar^2$ [16, 23]. Using a Lennard-Jones potential for V (or any potential that decreases faster than $1/r$), at long ranges the third term is nearly 0, and Eq. 2.21 reduces to

$$(\nabla_r^2 + k^2)\psi = 0. \tag{2.22}$$

We can therefore approximate the asymptotic wavefunction by a form that satisfies Eq. 2.22. We pick a form most useful for scattering analysis:

$$\psi = A(e^{ikz} + f(k,\theta)\frac{e^{ikr}}{r}). \tag{2.23}$$

This is a superposition of an incoming plane wave and an outgoing spherical wave with an angular amplitude dependence $f(k,\theta)$ [16, 23]. The probability that an incident particle will travel through some region $d\sigma$ in time dt is given by $dP = |A|^2 v dt d\sigma$ [16]. This must be equal to the probability that the particle scatters into some $d\Omega$: $dP = |A|^2|f|^2 v dt d\Omega$ [16]. Equating the two expressions give

$$\frac{d\sigma}{d\Omega} = |f(k,\theta)|^2 \tag{2.24}$$

Because the potential is central, the scattering is cylindrically symmetric and we may write the wavefunction out in terms of Legendre polynomials [14]:

$$\psi(r,\theta) = \sum_{l=0}^{\infty} R_l(k,r)P_l(\cos\theta). \tag{2.25}$$

(Note that Griffiths uses spherical harmonics instead of directly using Legendre polynomials. I will follow Marković's method of directly using Legendre polynomials.) Each l term is known as a partial wave. A similar expansion done for the hydrogen atom eventually results in spherical Bessel ($j_l(kr)$) and Neumann ($n_l(kr)$) functions, and therefore it is not surprising that [23]

$$\lim_{r\to\infty} R_l(k,r) = B_l j_l(kr) + C_l n_l(kr). \tag{2.26}$$

We can translate e^{ikz} directly into Legendre polynomial form. Eq. 2.23 then becomes:

$$\psi(r,\theta) \approx A(e^{ikz} + f(k,\theta)\frac{e^{ikr}}{r}) = A(\sum_{l=0}^{\infty} i^l(2l+1)j_l(kr)P_l(\cos\theta) + \sum_{l=0}^{\infty} f_l(k)P_l(\cos\theta)\frac{e^{ikr}}{r}). \tag{2.27}$$

(Note that Marković sets $A = 1$, as the value of A is inconsequential if we only wish to determine

$f(k,\theta)$ [23]). We can compare each l term of this expression for ψ to the asymptotic expression for ψ given by Eqs. 2.25 and 2.26. This gives us:

$$f(k,\theta) = \frac{1}{k}\sum_{l=0}^{\infty}(2l+1)e^{i\delta_l(k)}\sin(\delta_l(k))P_l(\cos(\theta)), \tag{2.28}$$

where $\delta_l(k) = \arctan(-C_l/B_l)$.

If we wish to determine the total cross-section, without the use of integrals [16, 23],

$$\sigma = \frac{4\pi}{k^2}\sum_{l=0}^{\infty}(2l+1)sin^2(\delta_l(k)). \tag{2.29}$$

2.4.2 The S, K and T Matrix Values

The S, K and T matricies values are convenient ways of encoding the information of the equations described at the end of Section 2.4.1. For general (potentially inelastic) scattering S, K and T are matricies, but for single-channel elastic scattering they are scalar values.

Let us define the T "matrix" as:

$$T_l(k) \equiv e^{i\delta_l(k)}\sin(\delta_l(k)), \tag{2.30}$$

S as:

$$S_l(k) \equiv 1 + 2iT_l(k), \tag{2.31}$$

and K using:

$$S_l(k) \equiv \frac{1+iK_l(k)}{1-iK_l(k)}. \tag{2.32}$$

Marković shows that we can write $K_l(k)$ in terms of the asymptotic Bessel and Neumann function coefficients in Eq. 2.26 [23],

$$K_l(k) = \tan(\delta_l(k)) = -\frac{C_l}{B_l}. \tag{2.33}$$

Using these definitions, we can rewrite Eqs. 2.28 and 2.29.

$$\sigma = \frac{4\pi}{k^2}\sum_{l=0}^{\infty}(2l+1)|T_l(k)|^2. \tag{2.34}$$

$$f(k,\theta) = \frac{1}{k}\sum_{l=0}^{\infty}(2l+1)T_l(k)P_l(\cos\theta), \tag{2.35}$$

This is not generally useful for analytical calculations (for the obvious reason that they are no

easier to obtain than $\delta_l(k)$), but they can be highly useful in numerical calculations of the cross-section, and are utilized in Fagnan's cross-section calculator (Section 5.1). S, K and T also play more significant roles in inelastic collisions.

2.5 Other Forms of Collisions

The theory outlined above, which was used to calculate $\langle \sigma v \rangle$, is for elastic collisions interacting along a single collision channel [20]. The particles were described as structure-less objects deflecting off one another. A more general treatment must consider the internal structure of each collision constituent.

Inelastic scattering occurs when the collision changes the internal energies of collision constituents [23]. These types of collisions are required for any understanding of quantum chemistry, as reactions must be described through atomic structure. Analyzing the simplest of inelastic collisions, however, requires a theoretical treatment much more complex than what has been described in Section 2.4.1 [23]. In our case, inelastic collisions come in the form of collisions that can change the $|F\, m_F\rangle$ states of the collision constituents. Generally, elastic collisions also depend on the internal states of collision constituents.

For Rb-Rb collisions, the fact that the trapped atom could be identical to the background atom if they had identical spin states leads to different scattering amplitudes. Burke showed that in situations where the incident and/or outgoing atoms are identical, $|f(k,\theta)|$ is given only by partial waves with even l:

$$f(k,\theta) = \frac{A_{ch}}{k} \sum_{l=even}^{\infty} (2l+1) e^{i\delta_l(k)} \sin(\delta_l(k)) P_l(\cos(\theta)), \tag{2.36}$$

where A_{ch} is determined by whether only the incoming constituents are identical (an inelastic collision), only the outgoing constituents are identical (inelastic), or both are identical (elastic) [8]. This significantly changes the loss cross section compared with that found using Eq. 2.13 at trap depths above 10 mK.

When a collision between two alkali atoms occurs, the valence electron of each Rb atom will be close enough to require consideration of spin addition. The cross-section of the collision will vary depending on whether the combined spin state is a triplet or a singlet [8].

A single-channel program was used to determine the scattering amplitude for Rb-Ar collisions; this program was applicable because argon, being a noble gas, does not react with rubidium. The complexities of calculating elastic Rb-Rb collisions must be addressed using a more complex, multi-channel numerical simulation. It is possible that the hyperfine state dependency we observed is due to additional channels that modify the value of $\langle \sigma v \rangle$.

Chapter 3

Experimental Apparatus Background

Our apparatus, the MAT (Miniature Atom Trap), is a magneto-optical/magnetic trap designed to trap ^{85}Rb and ^{87}Rb and test trap loss rates due to various background gases. In this section, the theoretical basis behind how the MAT operates will be described. Many of the concepts covered in this section, including the operation of a magneto-optical trap, are elucidated with significantly more (mathematical) detail in Fagnan's thesis [13]. Only the magnetic trap will be described in detail, as it is the primary trap used in the experiments detailed in this thesis.

3.1 The Magneto-Optical Trap

The magneto-optical trap is not the focus of this thesis, but it was used in all experiments both to load atoms into a magnetic trap and to measure indirectly Rb pressure. It, therefore, will be conceptually detailed below.

The magneto-optical trap captures and holds atoms by a combination of laser cooling and a potential well created by a magnetic field in conjunction with the cooling lasers. Laser cooling uses a series of laser-beams tuned to a wavelength slightly longer (colloquially, "red-detuned") than a specific hyperfine transition of the atoms that are to be trapped. The detuning significantly reduces the rate at which laser photons are absorbed by stationary atoms. Atoms moving toward the laser, however, will see laser photons Doppler shifted toward resonance, and therefore they will absorb laser photons at optimal efficiency, leading to a drop in their momenta parallel to the laser (due to conservation of momentum) [24]. Once the photon is absorbed, it will eventually be re-emitted due to spontaneous or stimulated emission. The change in momentum due to these emitted photons, however, is small and randomly directed, while the reduction in momentum due to absorption is systematic along one axis [24]. The random momentum changes largely cancel each other out; the systematic momentum reduction cools the atom from a kinetic enenergy corresponding to room temperature to a one in the μK level. Eventually the kinetic energy of the cooled atoms will still be non-zero from random changes in momentum due to laser absorption and re-emission; this kinetic

energy is the so-called "recoil limit", corresponding to the lowest ensemble temperature that can be reached using laser cooling [24].

An array of multiple beams aimed along three orthogonal directions can reduce momentum along any direction, and therefore can cool an ensemble of atoms [24]. The result of cooling is the creation of an optical molasses, a cloud of cold atoms with an effective temperature in the mK to μK regime [24]. Because particles in this optical molasses are not at zero temperature, random motion of cooled atoms will eventually disperse it.

In order to keep atoms trapped, a magnetic field gradient is used in conjunction with the lasers. At a distance from the centre of the trap, the gradient changes the energy levels of hyperfine transitions via the Zeeman splitting effect. When this Zeeman splitting is used in conjunction with circularly polarized, red-detuned laser light, hyperfine transition energies due to the laser light become position dependent. The position dependence is such that all imparted momentum from the transitions serve to move atoms back into the minimum of the magnetic field. This, then, constitutes a position dependent trapping force (see Fig. 3.1 for a diagram of this effect)[24]. In our trap, the magnetic gradient is provided by a pair of quadrupole coils in an anti-Helmholtz configuration.

In a two-state system, a single laser, call the "pump" laser, can be used to perform trapping. In a multi-state system, however, transition selection rules for the hyperfine states make it possible for an excited atom to transition to a hyperfine state not coupled to the trapping laser. In these situations, a "repump" laser is used to couple this state to an excited state where the atom could eventually return to the ground state coupled by the trapping laser.

When we trap ^{87}Rb in our MOT, the cooling/trapping laser is set to create transitions from the $5^2S_{1/2}\ |F=2\rangle$ state to the $5^2P_{3/2}\ |F'=3\rangle$ state (red-detuned to create cooling and position dependent trapping forces). The repump beam creates transitions from $5^2S_{1/2}\ |F=1\rangle$ to $5^2P_{3/2}\ |F=2\rangle$. When we trap ^{85}Rb in our MOT, the cooling/trapping laser is set to create transitions from $5^2S_{1/2}\ |F=3\rangle$ to $5^2P_{3/2}\ |F'=4\rangle$ (red-detuned). The repump beam creates transitions from $5^2S_{1/2}\ |F=2\rangle$ to $5^2P_{3/2}\ |F'=3\rangle$.

The equation for the number of atoms in a MOT is given by

$$N_{MOT}(t) = \frac{R}{\Gamma_{total}}(1-\exp(-\Gamma_{total}t)), \tag{3.1}$$

where

$$R = \frac{2}{\pi} n_{Rb} A \frac{v_c^4}{v_{th}^3} \tag{3.2}$$

where n_{Rb} is the background Rb number density, A is the trap surface area, $v_{th} = \sqrt{8k_BT/\pi m_{Rb}}$ is the mean speed of the background atoms, and v_c is the velocity under which atoms will be captured [13]. It is difficult to calculate many of the values listed here, such as A and v_c; what is important is that R is linearly proportional to n_{Rb}, and therefore can (and is) used as an indirect measure of

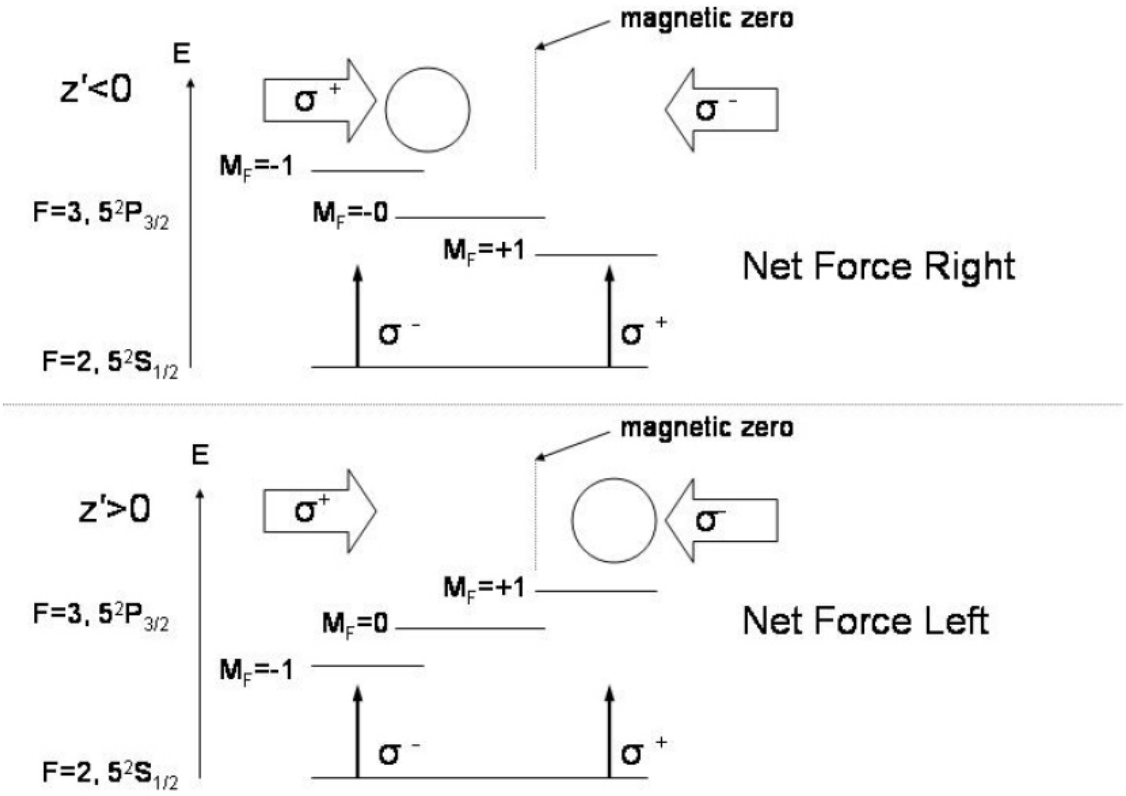

Figure 3.1: A diagram of the position-dependent forces in a magneto-optical trap. σ_+ circularly polarized light drives $5^2S_{1/2}|F=2\ m_F\rangle \rightarrow 5^2P_{3/2}|F'=2\ m_F+1\rangle$, and σ_- circularly polarized light drives $5^2S_{1/2}|F=2\ m_F\rangle \rightarrow 5^2P_{3/2}|F'=2\ m_F-1\rangle$. The Zeeman splitting caused by the position-dependent magnetic field from the quadrupole coils brings the σ_+ light further from its corresponding transition, and the σ_- light closer to its corresponding transition, when $z>0$, When $z<0$, the opposite is the case. Because one laser is preferentially absorbed over the other at different points in the trap, the forces between the two lasers are imbalanced. The MOT is designed such that this imbalance drives atoms back into the centre of the trap. Diagram from [13], courtesy of David Fagnan.

background Rb number density.

3.2 The Magnetic Trap

In contrast to the MOT, the magnetic trap uses only magnetic forces to trap atoms. In our magnetic trap configuration, room temperature Rb is first laser-cooled and trapped in a MOT. The trapped ensemble is then transferred to a magnetic trap, which uses the same quadrupole coils as the MOT does, making our system a MOT/magnetic trap hybrid.

3.2.1 Magnetic Trap Potential

The magnetic trap uses Zeeman splitting to create a position dependent potential to trap the atoms. If the magnetic field is sufficiently small, then the Zeeman splitting can be treated as a perturbation to the hyperfine splitting of Rb [16]. Our trap, however, can create magnetic fields of sufficient strength that changes in energy state due to Zeeman splitting are comparable to changes in energy due to hyperfine splitting. In these circumstances, the combined Zeeman and hyperfine splitting Hamiltonian must analyzed (as a perturbation to fine splitting) [16].

The full Zeeman-hyperfine Hamiltonian for a $5^2S_{1/2}$ Rb electron is [16]:

$$H = \frac{e}{2m}B(\mathbf{L}_z + 2\mathbf{S}_z) + \frac{\mu_0 g_p e^2}{m_p m_e}\left(\frac{3(\mathbf{I}\cdot\hat{r})(\mathbf{S}\cdot\hat{r}) - \mathbf{I}\cdot\mathbf{S})}{8\pi r^3} + \frac{\mathbf{I}\cdot\mathbf{S}\delta^3(\mathbf{r})}{3}\right) \tag{3.3}$$

$\mathbf{I}$ is the total nuclear angular momentum, or "nuclear spin", and $\mathbf{S}$ is the spin of electron (in our case, the hydrogen-electron-like valence electron of Rb). B is the magnitude of the magnetic field. Here, $\frac{e}{2m}B(\mathbf{L}_z + 2\mathbf{S}_z)$ is the Zeeman contribution to the Hamiltonian, and $\frac{\mu_0 g_p e^2}{m_p m_e}\left(\frac{3(\mathbf{I}\cdot\hat{r})(\mathbf{S}\cdot\hat{r}) - \mathbf{I}\cdot\mathbf{S})}{8\pi r^3} + \frac{\mathbf{I}\cdot\mathbf{S}\delta^3(\mathbf{r})}{3}\right)$ is the magnetic dipole contribution to hyperfine splitting. To perform perturbation theory on this Hamiltonian requires a certain degree of patience. Luckily, when the hyperfine splitting energy shifts are small compared to those of the fine splitting (as is the case in our magnetic trap), we can use IJ coupling to approximate the Hamiltonian [30]. Our Hamiltonian simplifies to [30]:

$$H = \frac{e}{2m}B(\mathbf{L}_z + 2\mathbf{S}_z) + A\mathbf{I}\cdot\mathbf{J} \tag{3.4}$$

The value of A can be experimentally determined, and the value we use was found from Steck's ^{87}Rb and ^{85}Rb rubidium line data [28–30]. Note that this Hamiltonian is only valid for the ground states of ^{87}Rb and ^{85}Rb. For excited states, the electric quadrupole and magnetic octupole contributions to the Hamiltonian must be considered, and Eq. 3.4 must be expanded to include these contributions [28, 29].

Through the use of the mathematical trick $(\mathbf{I}+\mathbf{J})^2 = I^2 + J^2 - 2\mathbf{I}\cdot\mathbf{J}$, we can rewrite the Hamiltonian as:

$$H = \frac{e}{2m}B(\mathbf{L}_z + 2\mathbf{S}_z) + A(F^2 - I^2 - J^2) \tag{3.5}$$

$\mathbf{F}$, the hyperfine spin number, is defined as $\mathbf{I}+\mathbf{J}$. The number of spin operators in this Hamiltonian suggests the use of $|F\, m_F\rangle$ states as the basis for the (to use Griffith's terminology) $\mathbf{W}$ matrix.

$$W_{ij} = \langle\psi_i|H|\psi_j\rangle \tag{3.6}$$

While the atomic states are expressed in $|F\, m_F\rangle$, the matrix elements given by Eq. 3.6 are most easily calculated using the $|I\, m_I\rangle\,|J\, m_J\rangle$ basis. Conversion between the two can be done using Clebsh-Gordan coefficients. For example, the $|2\,1\rangle$ state for ^{87}Rb $^2S_{1/2}$ can be expanded into:

$$|2\,1\rangle = \sqrt{\frac{1}{4}}|\frac{1}{2}\ -\frac{1}{2}\rangle|\frac{3}{2}\ \frac{3}{2}\rangle + \sqrt{\frac{3}{4}}|\frac{1}{2}\ -\frac{1}{2}\rangle|\frac{3}{2}\ \frac{1}{2}\rangle. \tag{3.7}$$

This is one of eight eigenstates for ^{87}Rb $5^2S_{1/2}$. Choosing $\psi_1 = |F=2\ m_F=2\rangle$, $\psi_2 = |2\,-2\rangle$, $\psi_3 = |2\,1\rangle$, $\psi_4 = |2\,0\rangle$, $\psi_5 = |2\,-1\rangle$, $\psi_6 = |1\,1\rangle$, $\psi_7 = |1\,0\rangle$, and $\psi_8 = |1\,-1\rangle$, we can create the **W** matrix:

$$\begin{pmatrix}
\frac{1}{2}\mu B+\frac{3}{2}\gamma & 0 & 0 & 0 & 0 & 0 & 0 & 0 \\
0 & -\frac{1}{2}\mu B+\frac{3}{2}\gamma & 0 & 0 & 0 & 0 & 0 & 0 \\
0 & 0 & \frac{1}{4}\mu B+\frac{3}{2}\gamma & 0 & 0 & -\frac{\sqrt{3}}{4}\mu B & 0 & 0 \\
0 & 0 & 0 & \frac{3}{2}\gamma & 0 & 0 & -\frac{1}{2}\mu B & 0 \\
0 & 0 & 0 & 0 & -\frac{1}{4}\mu B+\frac{3}{2}\gamma & 0 & 0 & \frac{\sqrt{3}}{4}\mu B \\
0 & 0 & -\frac{\sqrt{3}}{4}\mu B & 0 & 0 & -\frac{1}{4}\mu B-\frac{5}{2}\gamma & 0 & 0 \\
0 & 0 & 0 & -\frac{1}{2}\mu B & 0 & 0 & -\frac{5}{2}\gamma & 0 \\
0 & 0 & 0 & 0 & \frac{\sqrt{3}}{4}\mu B & 0 & 0 & \frac{1}{4}\mu B-\frac{5}{2}\gamma
\end{pmatrix}$$

Where:

$$\gamma = \frac{\hbar^2 A}{2}$$
$$\mu = \frac{e\hbar}{m}$$

Once **W** is obtained, the matrix can be diagonalized. The functional relationship between potential energy splitting and magnetic field amplitude can be created by determining the eigenvalues at various field amplitudes, and the superpositions of hyperfine states each energy curve correspond to can be determined by finding the corresponding eigenvector to each eigenvalue. A Breit-Rabi diagram can be created with these functions; Fig. 3.2 is an example of such a diagram, for ^{87}Rb $|F=2\rangle$. States whose energies decrease as B is increased are known as "strong-field seeking", or paramagnetic (since the derivative of the energy curve is magnetic force), and states whose energies increase are known as "weak-field seeking", or diamagnetic.

To finally determine the potential energy of an Rb atom in the magnetic trap as a function of position, we must find the magnetic field amplitude of the trap as a function of position. The magnetic field of a generic set of quadrupole coils in an anti-Helmholtz configuration can be found using the Biot-Savart law. The results indicate that the anti-Helmholtz coils create a field with one point where $B = 0$; this is the centre of the trap, to which I will give the coordinates $\mathbf{r} = 0$. The magnetic field near this region can be approximated as [13]:

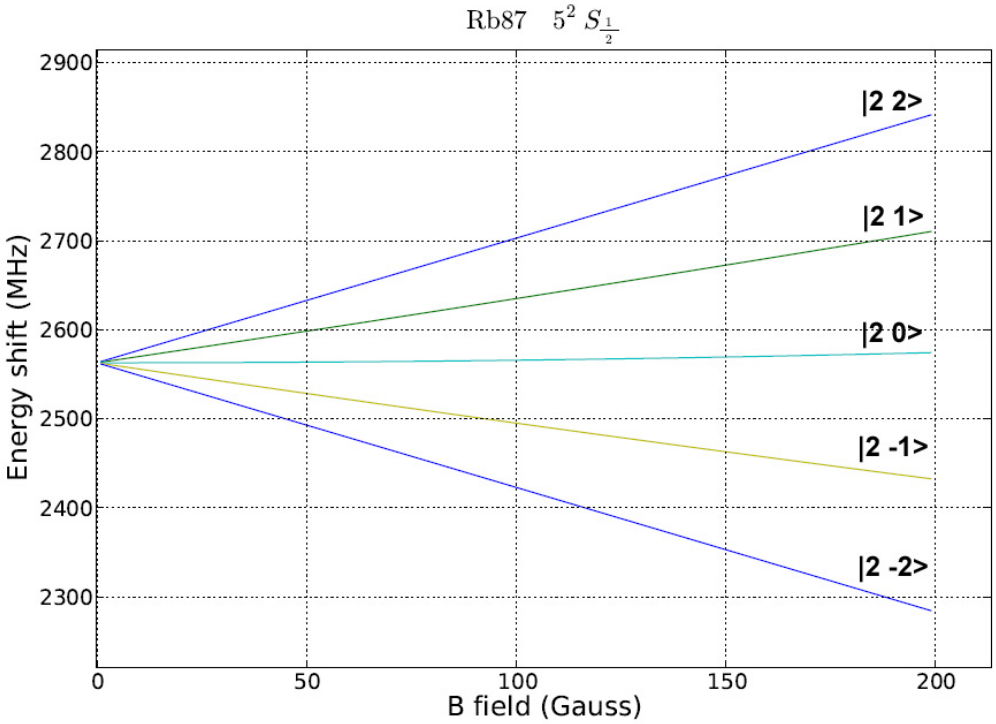

Figure 3.2: A Breit-Rabi diagram of the Zeeman splitting of ^{87}Rb $5^2S_{1/2}$ $|F=2\rangle$. The hyperfine states corresponding to each Zeeman-hyperfine splitting are labelled on the right. The energy shift at $B=0$ is the shift for the $|F=2\rangle$ hyperfine splitting from the $5^2S_{1/2}$ fine splitting of ^{87}Rb. The weak-field seeking, or diamagnetic, states are $|2\,2\rangle$, $|2\,1\rangle$, and $|2\,0\rangle$. This figure was created using [17].

$$\mathbf{B} = \frac{3\mu_0 IDR^2}{(D^2+R^2)^{5/2}}\left(-\frac{1}{2}x\hat{\mathbf{x}} - \frac{1}{2}y\hat{\mathbf{y}} + z\hat{\mathbf{z}}\right). \tag{3.8}$$

Inserting the field magnitude B into the energy curves calculated from the eigenvalues of the $\mathbf{W}$ matrix determines the value of potential energy with respect to position. Because an anti-Helmholtz trap has $B=0$ at the trap centre, and $B>0$ off of the centre, only diamagnetic hyperfine states are trappable.

3.2.2 Magnetic Trap Majorana Losses

The notion of a trapped particle experiencing a definite position dependent potential energy in a magnetic trap is based on the assumption that a trapped $|F\,m_F\rangle$ state will remain in the same state indefinitely despite a position-dependent magnetic field. Meyrath states that under the condition

$$\frac{\mathbf{v}\cdot\nabla B}{\omega_L B} \ll 1, \tag{3.9}$$

the trapped particle's magnetic moment will adiabatically follow the trap's magnetic field lines [25]. (B is the magnitude of the $\mathbf{B}$ field, and ω_L is the Larmor precession frequency, given by $\omega_L = \gamma B = \mu \cdot \mathbf{B}/\hbar$.) Normally in a magnetic trap this is true, but close to the centre of the trap, B becomes quite small, resulting in the violation of the inequality [25]. Then, the rapidly varying magnetic field results in spin-flips, called Majorana spin-flips, that potentially result in transitions of trapped atoms to untrappable m_F states [13, 25].

A simple model can be constructed of Majorana losses by assuming that in atoms are definitively lost in all regions where $\mathbf{v} \cdot \nabla \mathbf{B}/\omega_L B > 1$. We find the equation for the border, $\mathbf{v} \cdot \nabla \mathbf{B}/\omega_L B = 1$, along the z-axis (the same could be done along the x or y axes, to similar results). Noting that near $z = 0$ $B = B'z$,

$$z^2 = \frac{v_z}{\gamma B'}. \tag{3.10}$$

From the definition of loss rate, $\Gamma = n\sigma v \approx n\pi z^2 v$, and the conversion of KE into an effective temperature (assuming $v_x = v_y = v_z$), $\frac{3}{2} m {v_z}^2 = kT$:

$$\Gamma \approx \frac{2n\pi kT}{3m\gamma B'}. \tag{3.11}$$

This is an order of magnitude estimate of Γ at best, but it does indicate that Γ should scale with trapped atom number density n, and should scale inversely with magnetic field gradient B'.

3.3 RF Coil-Induced Hyperfine Transitions

An effect commonly utilized in nuclear magnetic resonance and RF spectroscopy is the inducing of m_F state transitions through the use of a time-varying magnetic field [16, 30]. In our system, the source of the RF field is a small coil connected to an AC current driver, which we call an RF coil, or RF knife. A rigorous treatment of the functioning of an RF knife is difficult to create, and a full mapping of the RF transitions in our system would likely require numerical calculations. I will give a conceptual description of the operation of the RF knife only.

Due to the AC current passed through the coil, the RF knife emits a time-varying magnetic field. The magnetic field induces magnetic dipole transitions in the trapped atoms, which follow the selection rules $\Delta F = 0$ $\Delta m_F = \pm 1$ [6, 11]. During the transition, the potential energy of the trapped atoms changes by $h\nu_{RF}$, where ν_{RF} is the frequency of the AC current. This means the RF knife can only induce transitions between two hyperfine magnetic sublevels at points where the energy difference between the two sublevels is $h\nu_{RF}$. The efficacy of the RF knife is dependent on the position of the trapped atom, because of the position dependence of the alignment between the RF magnetic field and the trap magnetic field. The RF knife cannot induce transitions at any point where the magnetic field from the RF knife is parallel to the field from the quadrupole coils.

It is important to note that the frequency ν_{RF} of the RF knife is not related to the energy of the atoms being ejected simply by $E_{\Delta m_F} = h\nu_{RF}$. For example, we trap $|1\,-1\rangle$ of ^{85}Rb, and use an RF knife with frequency ν to couple to the untrappable $|1\,0\rangle$ state, leading to trap loss (see Fig. 3.3). The difference in Zeeman splitting energy between $|1\,-1\rangle$ and $|1\,0\rangle$ reaches $\Delta E = h\nu_{RF}$ along a surface **x** in the trap, and it is on this surface that the RF knife can induce transitions. The potential energy of $|1\,-1\rangle$ atoms at points **x** is $E(\mathbf{x})$, which is smaller than $h\nu_{RF}$. The general relationship between RF knife frequency and the trap depth at which transitions occur is a complicated one, and we have written a number of programs to help with the calculation.

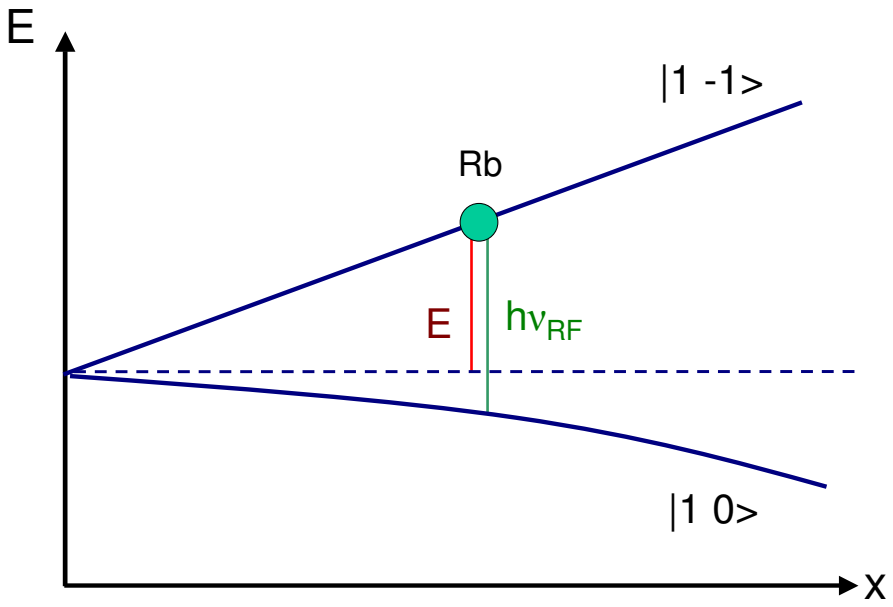

Figure 3.3: A diagram of a transition from ^{87}Rb $|1\,-1\rangle$ to $|1\,0\rangle$. The RF knife couples the two hyperfine states at a point **x** where the difference in Zeeman splitting curves is $h\nu_{RF}$. Atoms ejected from the $|1\,-1\rangle$ state at **x** are at potential E ($E < h\nu_{RF}$), and thereby atoms that can reach potential E are eventually lost from the trap due to the RF knife.

Bouyer *et al.* noted an important feature of RF transitions in situations where many m_F states are trappable [6]. Because the selection rule for RF transitions is $\Delta F = 0$ and $\Delta m = \pm 1$, an attempt at driving a stretched state into an untrappable state requires multiple transitions, as shown in Fig. 3.4 for the example of ^{87}Rb $|2\,2\rangle$. So long as the atom is still in a trappable state, there is also a

non-zero probability for the atom to transition from $|F\ m_F\rangle$ to $|F\ m_F+1\rangle$ [6]. The end result is that the probability of ever reaching an untrappable state is often less than 10%.

Many of the finer details of our particular RF knife were determined experimentally, and can be found in the MAT Trap section.

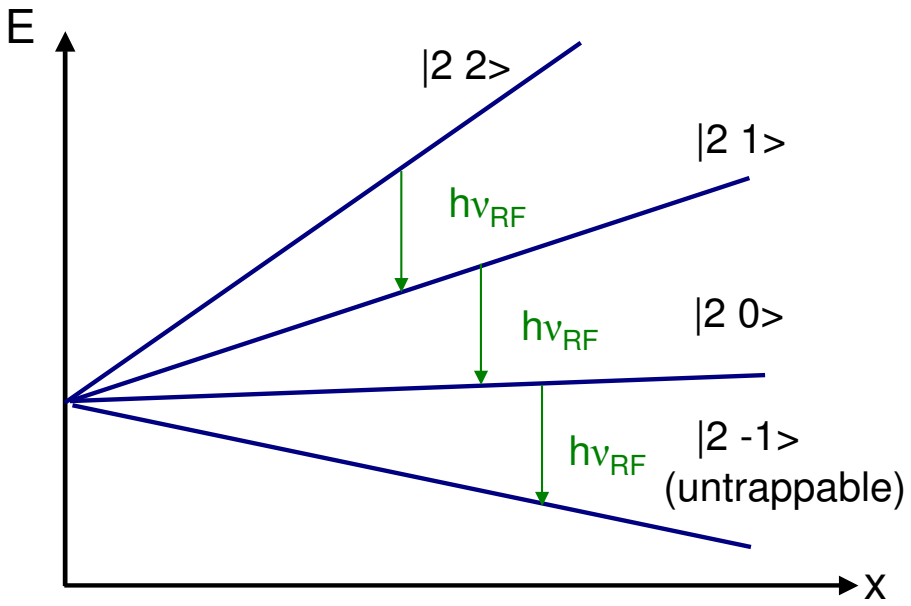

Figure 3.4: A diagram showing how difficult it would be to use the RF knife to transition a trapped ^{87}Rb $|2\,2\rangle$ atom to untrappable state $|2-1\rangle$, as described by Bouyer *et al.*. Three transitions would have to be made before the atom is ejected. The probability of ever reaching the $|2-1\rangle$ or lower is less than 10% [6].

3.4 Zeeman-Optical Pumping

Zeeman-optical pumping (or just "Zeeman pumping" for short) operates on the same physical principles as the position dependent trapping force of the MOT. A set of circularly polarized laser beams provide electric dipole transitions that guide all $|F\,m_F\rangle$ states in a cold ensemble to a particular "stretched" state $|F\ \pm F\rangle$. A uniform magnetic field provides an axis of quantization.

The process by which this pumping works is best described with a diagram. Fig. 3.5 shows an

example of ^{87}Rb Zeeman-optical pumping. Let us assume that the ^{87}Rb trapped ensemble initially starts out entirely in the $|2\,0\rangle$ state. The incoming laser beams are circularly polarized and we may orient the magnetic field in such a way that it drives $\Delta m = +1$ (i.e. the beams are σ_+ polarized). The pump beam therefore creates transitions between $5^2S_{1/2}\,|F = 2\ m_F\rangle$ and $5^2P_{3/2}\,|F' = 2\ m_F + 1\rangle$ for any given m_F value, and the repump beam creates transitions between $5^2S_{1/2}\,|F = 1\ m_F\rangle$ and $5^2P_{3/2}\,|F' = 2\ m_F + 1\rangle$. Recall that primed values inside hyperfine spin numbers indicate that the atom is in the $5^2P_{3/2}$ excited state, and non-primed values indicate the $5^2S_{1/2}$ ground state. The pump beam drives $|2\,0\rangle \rightarrow |2'\,1\rangle$ transitions. Due to the selection rules for electric dipole transitions ($\Delta F = 0, \pm 1$ and $\Delta m = 0 \pm 1$) this excited state can spontaneously transition back down to $|2\,0\rangle$ (which is not a problem, since a laser is already in place to force it back to $|2'\,1\rangle$), $|2\,1\rangle$, $|2\,2\rangle$, $|1\,0\rangle$ or $|1\,1\rangle$. Any atoms falling to $|2\,1\rangle$ will, due to the pump laser, transition to $|2'\,2\rangle$. From there, they fall to the $|2\,2\rangle$, $|2\,1\rangle$ and $|1\,1\rangle$ states. Atoms falling into $|1\,0\rangle$ or $|1\,1\rangle$ will, via the repump laser, transition to $|2'\,1\rangle$ and $|2'\,2\rangle$, respectively. With this maze of transitions in place, eventually all atoms are funnelled into the dark state $^2S_{1/2}\,|2\,2\rangle$.

To Zeeman pump into $5^2S_{1/2}\,|1\,-1\rangle$, we reverse the magnetic field, making the circularly polarized light σ_- light driving $\Delta m = -1$ transitions. The problem is that the repump beam will actually drive $|1\,-1\rangle$ to $|2'\,-2\rangle$ transitions, past which it may drop into $|2\,-2\rangle$, which cannot be coupled to anything using σ_- light. To perform Zeeman pumping to $|1\,-1\rangle$ we must tune our repump beam to the $|1\,0\rangle \rightarrow |2'\,-1\rangle$, which makes the beam off resonance to the $|1\,-1\rangle \rightarrow |2'\,-2\rangle$ transition. This reduces the rate at which the transitions occur. Additionally, the repump beam is turned off first, allowing both excited atoms and those in the $|F = 2\rangle$ ground state to fall to $|1\,-1\rangle$, without any repump beam to force $|1\,-1\rangle$ to undergo transitions.

The ^{85}Rb Zeeman optical pumping system works on nearly identical principles, except, due to the increased number of states, the series of transitions set up is generally more complex.

It is important to note that with this system it is impossible to set up a series of transitions leading to an ensemble composed only of, for example, $|1\,0\rangle$ or $|2\,1\rangle$ states. Only the states with the largest absolute value magnetic numbers can be reached with Zeeman pumping (and then only one out of the two states will be trappable).

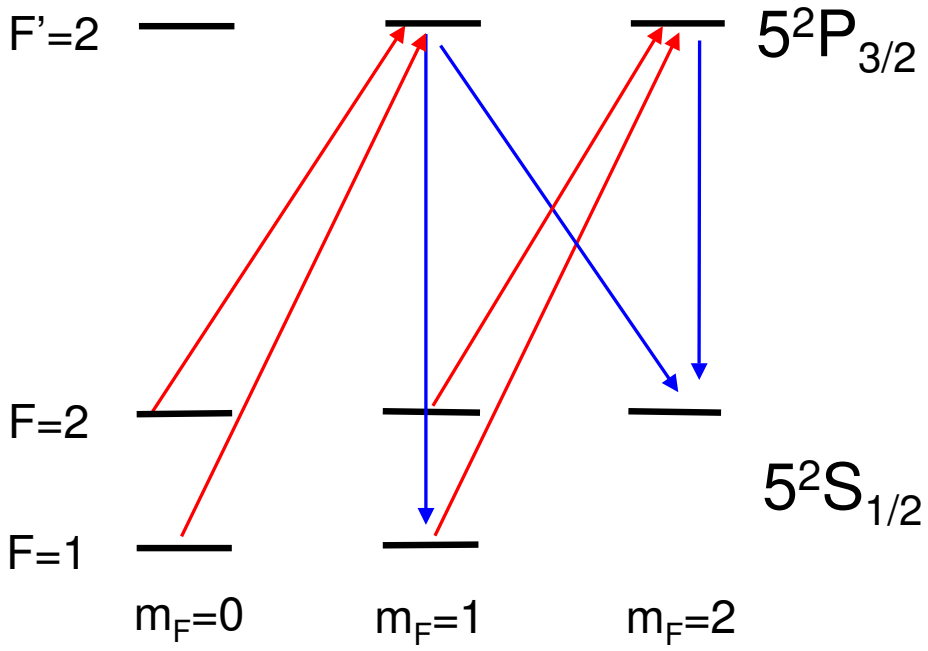

Figure 3.5: A schematic of the Zeeman pumping process described in Section 3.4, showing a few possible transition paths for a trapped atom. Each bar is a hyperfine state with some F and m_F number indicated by the labels. Red arrows are transitions due to the laser, and blue arrows are spontaneous emission transitions. For example, an atom starts in $|2\,0\rangle$. $\sigma+$ pump laser light excites it to $|2'\,1\rangle$, from which it can decay to any of the $5^2S_{1/2}$ states shown, including the desired $|2\,2\rangle$. If the decay is to $|1\,1\rangle$, then $\sigma+$ repump light boosts it to $|2'\,2\rangle$, where it can potentially drop to $|2\,2\rangle$. All other possible decay paths of the excited atom are accounted for by the pump and repump beams such that the $|2\,2\rangle$ becomes the most likely final state of any trapped atom.

Chapter 4

The Miniature Atom Trap (MAT)

Our magneto-optical/magnetic trapping system is built, as previously stated, to laser cool and trap either ^{87}Rb or ^{85}Rb. It can be seen in cartoon form in Fig. 4.1, and in labelled photographic form in Fig. 4.2. Many of the details of the system have been thoroughly described in Fagnan's thesis and other works; these details will be summarized very briefly here. For further details, please see [12, 13, 19].

4.1 Vacuum System

The average pressure in the system at any given time of experiment taking is 10^{-7} to 10^{-10} Torr. To maintain this pressure, three separate vacuum pumping systems are used: a Thermionics IP-011 ion pump, two (now one) Varian Turbo-V 70 turbomolecular pumps attached to a Varian SH-100 roughing pump, and a set of chemical getter pumps which relies on a chemical reaction between the pump's active material and the background atoms [13]. The three pumps work in tandem to keep the pressure both low and consistent over time, though the ion pump is sometimes turned off during experiments because pumping in the test region may distort pressure readings [13].

During the summer of 2009, one of the two Varian Turbo-V 70 pumps failed. From July 19$^{\text{th}}$, 2009, to late November, the system ran on only the ion and getter pumps, and therefore had to be tightly sealed. Only Rb-Rb measurements were made during this time, since the seal prevented the injection of any other background gases. Starting in December, the turbo pump system was reactivated with only one pump. The current readout on the ion pump (the current is to maintain the electromagnetic field that performs the ionization and pumping) has climbed from below 1 μA in July to nearly 80 μA in April 2010, leading to fears that the ion pump will soon fail. As of this writing, this has yet to happen.

When performing loss rate measurements against background gases other than Rb, the gas injection system, see in Fig. 4.1 is used. A residual gas analyzer determines the pressure of gas entering the system. As these systems were not used during the course of this project, they are noted here

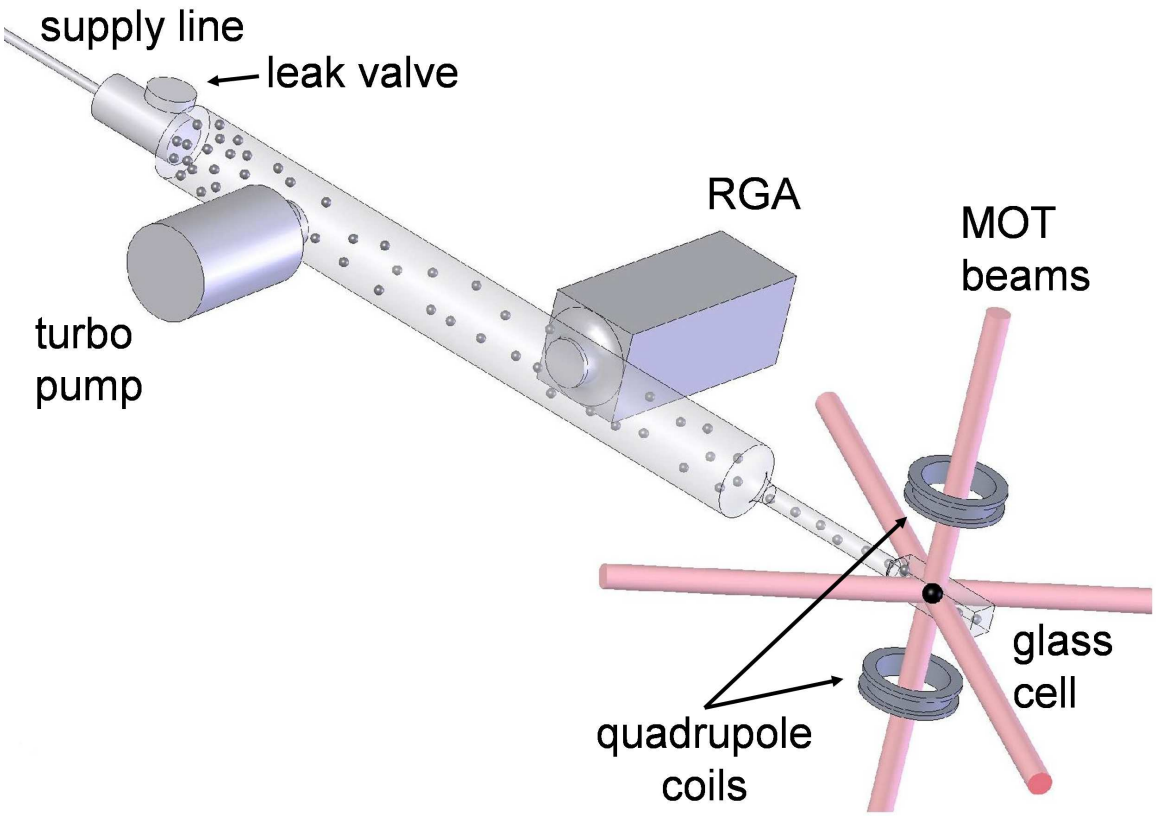

Figure 4.1: A simplified schematic of the MAT magneto-optical/magnetic trap. Diagram from [13], courtesy of David Fagnan.

simply for completion.

4.2 Rubidium Injection System

A commercially available electrically-activated rubidium source (Alvatec As-2-Rb-25-V 2mm 25mg source) is used to re-supply Rb to the vacuum chamber. Because the ion and getter pumps remove Rb from the system over time, re-supply must be performed periodically to maintain enough Rb for acceptable MOT fluorescence signal and signal-to-noise ratio. Refill procedure involves slowly increasing the current to the source up to 5.0 A using a Sorensen DLM40-15 power supply, and leaving the current at that value for 1 to 5 minutes before ramping the current back down. The time during which the current is at 5.0 A determines roughly how much Rb is injected into the system. The amount of Rb injected into the system cannot be controlled like those of the other background gases.

Once loading is complete the Rb number density takes approximately 12-14 hours to equilibriate [13]. During equilibration, the number density falls exponentially from some initial level to its final

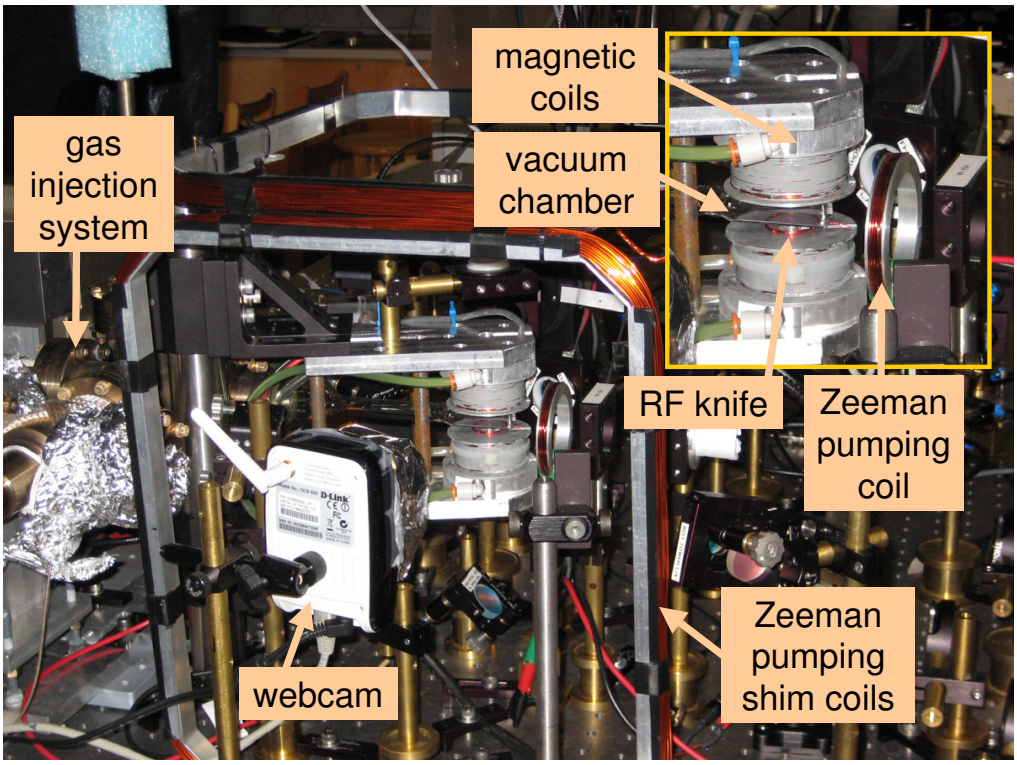

Figure 4.2: A photograph of the MAT, labelled to indicate significant components of the system. The insert photo is a close-up of the MAT components surrounding the vacuum cell.

equilibrium level, as seen in Fig. 4.3. Once equilibration occurs, the number density will still very slowly drop, over the course of days or weeks.

One unfortunate aspect of the injection system design is that the source is not part of the gas injection system. There is then no real way of determining the rubidium pressure in the system. Throughout our Rb-Rb collision experiments, we have had to use the MOT loading rate R as an indirect measurement for rubidium pressure to compensate.

4.3 Imaging Systems

4.3.1 Photodiode

The fluorescence of the MOT due to the cooling lasers is determined through the use of a photodiode, a device that absorbs incoming light and outputs a corresponding voltage/current. A focusing lens is

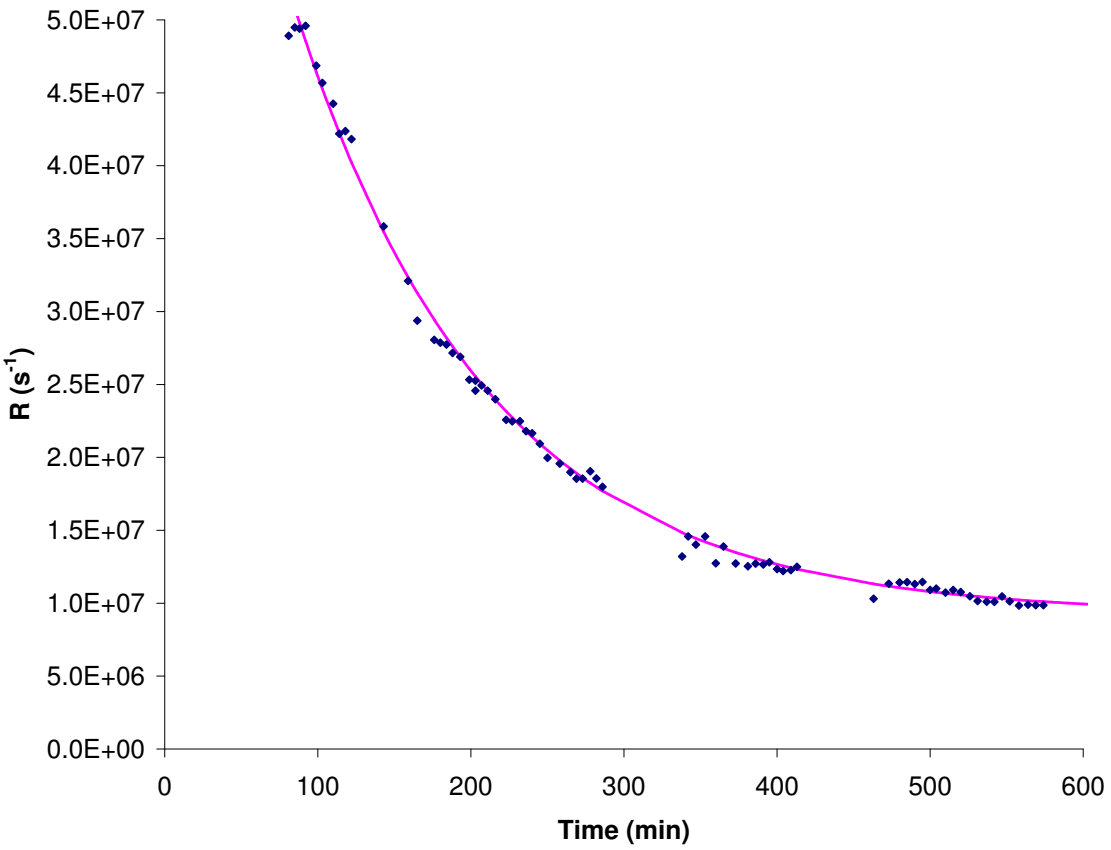

Figure 4.3: An example of an Rb equilibration curve. MOT loading rate R is used as a proxy for Rb background number density. An exponential decay has been fitted to the data, indicating that R decreases exponentially from a t = 0 value of $(8.15 \pm 0.11) \times 10^7$ s^{-1} to a steady state value of $(9.249 \pm 0.084) \times 10^6$ s^{-1}.

placed in front of the cell in order to focus MOT fluorescence onto the photodiode aperture. Fagnan gives the relationship between power from the light passing through the lens to MOT fluorescence as

$$P \approx 0.92 h\nu \frac{r_{lens}^2}{d_{lens}^2} N R_{scatter} \tag{4.1}$$

where $R_{scatter}$ is the scatter rate of photons off of a trapped atom, and N is the total number of trapped atoms, which is linear to P. Practically, this conversion is used to determine the initial loading rate of atoms into the MOT, R, in units of number of atoms per second. It is worthwhile to note the alignment of the photodiode that maximizes both signal and signal-to-noise ratio is dependent on the exact position of the MOT trapped ensemble, and Eq. 4.1 does not include this effect. In practice, at the start of any given experiment the photodiode is realigned to maximize signal and

signal-to-noise ratio.

4.3.2 CCD Camera

Instead of giving a power value, the CCD camera measures intensity, and therefore has two-dimensional resolution. This is important to our experiments largely in that we use our FLI-MX0053307 CCD camera to properly align the MOT. We are not concerned with the exact shape of the MOT ensemble, only that it remains consistent over the course of an experiment, and does not rapidly change shape or develop non-spherical patterns. The CCD was also used by Fagnan to determine the temperature of the MOT trapped ensemble through absorptive imaging, yielding a value of 40-100 μK [13].

4.3.3 Webcam

We have recently installed a DLink DCS920 colour webcam to supplement the CCD camera. Other than giving us a slightly different axis by which to view the atoms, and the ability to view the MOT in real time, the camera can be viewed remotely. The webcam is part of a larger project to control the entire MAT remotely, with a variety of applications from classroom demonstrations to remote monitoring of experimental progress.

4.4 Laser Systems

The lasers used to generate the pump and repump beams are external cavity diode lasers, whose wavelengths are controlled by changing the orientation of the cavity grating and the laser injection current. When the lasers are locked to a particular wavelength, the grating and current are electronically controlled to compensate for any wavelength drift. A set of injection-locked slave lasers are used to amplify the laser light before it reaches the MOT system. On the MAT table, the pump laser provides 20 mW of power, while the repump laser provides 0.8 mW of power.

When we trap ^{87}Rb in our MOT, the cooling laser is red-detuned 12 MHz from the $5^2S_{1/2}$ $|F=2\rangle$ to $5^2P_{3/2}$ $|F'=3\rangle$ transition. The repump beam is set to the transition $5^2S_{1/2}$ $|F=1\rangle$ to $5^2P_{3/2}$ $|F'=2\rangle$. When we trap ^{85}Rb in our MOT, the cooling laser is red-detuned 12 MHz from the $5^2S_{1/2}$ $|F=3\rangle$ to $5^2P_{3/2}$ $|F'=4\rangle$ transition. The repump beam is set to the transition $5^2S_{1/2}$ $|F=2\rangle$ to $5^2P_{3/2}$ $|F'=3\rangle$. Refer to [19] for more details.

Red-detuning is determined by a set of acoustic optical modulators (AOMs). As stated above, we typically shift the cooling/trapping beam by 12 MHz. During magnetic trap loadings, we typically shift the beam to 40 MHz in order to obtain a colder distribution of atoms [13].

Light activation/deactivation is also achieved through the AOMs. A set of solenoid-powered shutters prevents stray light from entering the system. These shutters have operation times generally less than 20 ms, but within this regime they are sometimes quite variable [13].

4.5 The Magnetic Coils

Our set of magnetic quadrupole coils is composed of two identical water-cooled copper coils situated above and below our MOT. The exact technical specifications can be found in Djuricanin [12]. The coils have an $\frac{3\mu_0 DR^2}{(D^2+R^2)^{5/2}}$ (in accordance with Eq. 3.8) value of 55.7 G cm^{-1} A^{-1}, and have been tested up to 30 A. In practice, no more than 14 A has been used for experiments, due to even small changes in coil temperature having an effect on the trap shape and number of atoms trapped.

In general, we run a 0.5 A (27.8 G cm^{-1} along the z-axis, or 13.9 G cm^{-1} along the x) current through our coils to supply the Zeeman splitting necessary for the MOT.

4.6 The RF Knife

The RF knife is a coil of 10 turns of copper wire 2.2 cm in diameter attached to the base of the MAT glass vacuum chamber, as seen in Fig. 4.2. It is connected to a digital frequency synthesizer and amplifier (that also controls our AOMs), which outputs a specific user-defined frequency. The RF knife is electronically controlled via a UTBus computer driver through a LabView/Python command console.

The RF knife has an effective frequency range of approximately 2 MHz to around 120 MHz (see Fig. 4.4). Below 1 MHz and above 120 MHz, the amplitude of the RF knife output drops considerably, and should no longer be considered effective. The Nyquist sampling frequency for the frequency synthesizer is 150 MHz, and therefore it is impossible for the RF knife to operate at a frequency higher than this value.

The RF knife drives hyperfine transitions at exactly one potential energy in the trap. During experimentation, we commonly sweep the RF knife over a range of frequencies, in order to eliminate all atoms of a certain energy or higher. The RF knife must be able to reach all values of potential energy in the trap, and because 120 MHz is the upper RF frequency limit, this forces us to use the RF knife only with traps of around 5 mK or less.

An atom with total energy E will explore the regions of the trap where the potential $V < E$. It is then theoretically possible that setting the RF knife to a single frequency will eliminate all atoms of a corresponding total energy or higher given enough time. (This is also the reason why we cannot perform RF "surgery", where all atoms of a narrow band of energy ΔE are removed from the trap.) The amount of time this takes has not yet been determined, but testing whether setting a constant RF frequency is an effective method of eliminating all atoms of a specific energy or higher should be considered for future work.

The effectiveness over time of the RF knife was determined experimentally. Over the course of 125 ms, all atoms in a 3.12 ± 0.84 mK trap were eliminated by an RF knife sweep from 0 to 90 MHz. 125 ms has become the standard sweep time for all RF knife measurements.

Because RF sweeping eliminates all atoms from the trap of some energy or higher, RF sweeping

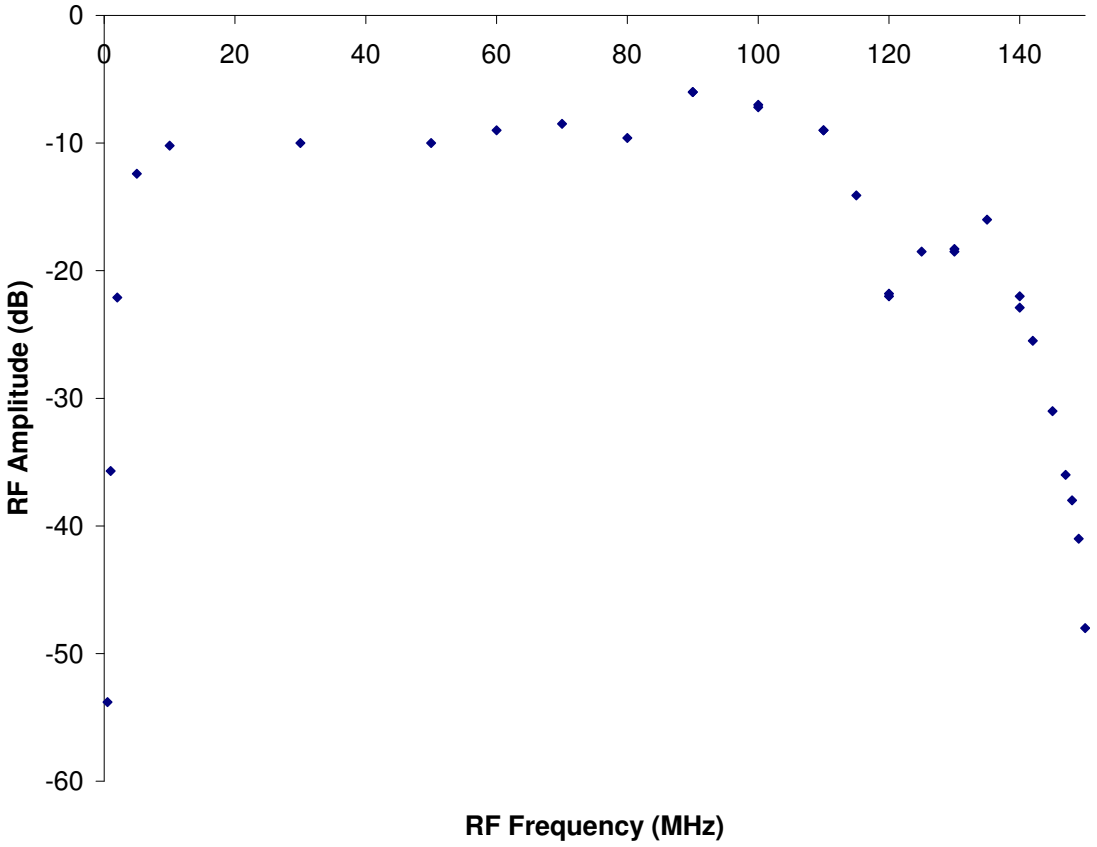

Figure 4.4: A plot of RF amplitude as a function of RF frequency ν_{RF}. The amplitude remains relatively constant except in the region of 0 - 2 MHz and past 115 - 120 MHz.

continuously is an effective way of setting the trap depth of a magnetic trap. This has been done with considerable success, and the RF was used to set the trap depth for all heating measurements in Section 6.2 and Section 6.3. It was not used to set the trap depth for any experiment that also used Zeeman pumping; I describe the reason for this in Section 6.5.

4.7 The Zeeman-Optical Pumping System

The Zeeman-optical pumping system uses the same lasers as the MOT. Beam-splitting cubes are used to siphon off a small amount of laser light from the pump and repump lasers. The Zeeman pump beam must couple, per the description in Section 3.4, $|F = 2\rangle$ to $|F' = 2\rangle$; because of this the Zeeman pump beam has a separate AOM from the MOT pump beam (which couples $|F = 2\rangle$ to $|F = 3\rangle$). Both the +1 and -1 orders of this AOM are used, one for ^{87}Rb and one for ^{85}Rb, to allow for rapid switching of Zeeman pumping lasers for different isotopes. The Zeeman repump beam does not require a separate AOM from the MOT repump, since both beams couple to the same

hyperfine states. While the AOMs also have control over the beam amplitudes, this is generally insufficient to produce the beam strengths desired, so sets of neutral-density filters are placed in the Zeeman pump and repump beam paths depending on which hyperfine state is desired. The mirror configuration for the Zeeman system was designed to minimize the number of additional mirrors needed in proximity to the vacuum cell; as a result, small shifts in the position of certain mirrors can easily cause de-alignment of the Zeeman system.

A 6.5 cm diameter Zeeman coil has been mounted beside the MAT vacuum cell (see Fig. 4.2). A set of two 31 cm $\times$ 36 cm square shim coils have been mounted further out from the cell. These coils are designed to work in tandem to create a magnetic field uniform in direction in the region of the MAT vacuum cell. This gives us our axis of quantization on which the Zeeman pump and repump beams act. A 6-channel gradient coil driver (model E06-020) powers the Zeeman coils.

The precise timing of light activation/deactivation is achieved through the AOMS. When we pump to ^{87}Rb $|3\,3\rangle$ or ^{85}Rb $|2\,2\rangle$, the pump beam is turned off first, while for ^{87}Rb $|2\,-2\rangle$ or ^{85}Rb $|1\,-1\rangle$ the repump beam is turned off first. This is to prevent transitions away from the desired state while allowing atoms in remaining states to continue transitioning into the desired state. Zeeman pumping in its entirety takes approximately 0.8 to 5.5 ms (depending on which state is being pumped). A set of solenoid-powered shutters are used to prevent stray Zeeman laser light from entering the system when Zeeman pumping is not in use, and the MOT pump/repump shutter is closed during Zeeman pumping to prevent the MOT lasers from interfering with pumping. The shutters, however have reaction times that occassionally drift by a considerable amount of time, or cease working entirely. There have been a number of cases when Zeeman pumping had failed due to either μW amounts of stray light from the MOT lasers being let in by a malfunctioning MOT laser shutter, or a lack of Zeeman light from malfunctioning Zeeman shutters.

The combination of drifting mirrors and drifting shutters means the Zeeman pumping system must be periodically optimized in order to maintain pumping efficacy.

Because $|F\,m_F\rangle$ states with the largest m_F numbers (i.e. the stretched states) have, given some magnetic field, the largest Zeeman splittings compared to other $|F\,m_F\rangle$ states, while the gravity potential gradient affects all $|F\,m_F\rangle$ states in the same manner, very shallow traps may hold stretched states, but not $|F\,m_F\rangle$ states with smaller $|m_F|$ numbers. This fact is utilized after Zeeman pumping is completed, when the magnetic trap coil currents are reduced to values low enough so that only stretched states can still be trapped. Optimum values were experimentally determined (see Figs. 4.5 and 4.6). The trap is then allowed to evolve for 200 ms to give enough time for non-stretched state atoms to fall out of the trap. This gravity filtering ensures the final trapped ensemble is a single, pure, $|F\,m_F\rangle$ state.

When optimized, the system results in 60-80% of atoms trapped in the desired stretched state, and negligible amounts trapped in other states. This is around twice as much as the 30-50% reported by Fagnan [13].

The Zeeman pumping process currently in use also appears to raise the average energy of the atoms in the magnetic trap by several mK.

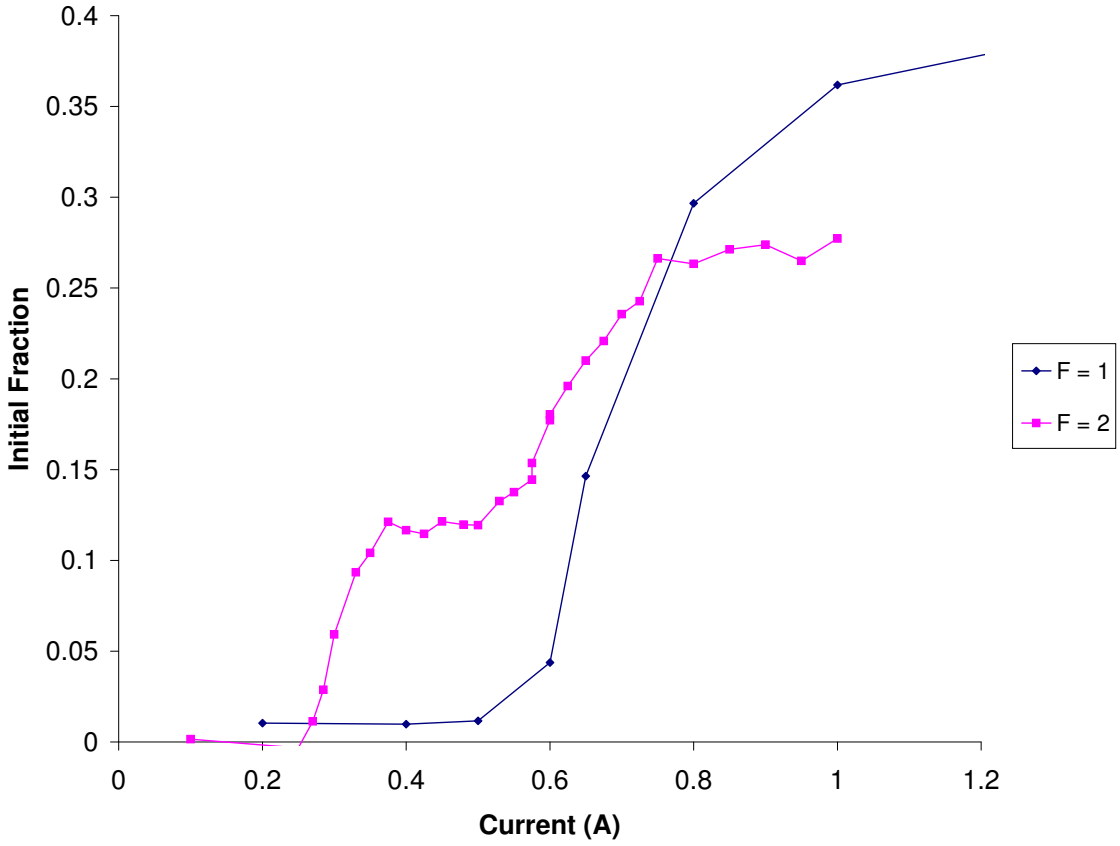

Figure 4.5: A plot of the fraction of the ^{87}Rb $|F=1\rangle$ and $|F=2\rangle$ atoms loaded into the magnetic trap from a MOT as a function of magnetic coil current, experimentally determined in order to find the optimal currents for spin filtering. For $|F=1\rangle$, only $|1\,-1\rangle$ is trappable. For $|F=2\rangle$, $|2\,2\rangle$ becomes trappable at $\sim$0.3 A, and $|2\,1\rangle$ at $\sim$0.6 A. $|2\,0\rangle$, not shown here, becomes trappable at $\sim$7 A.

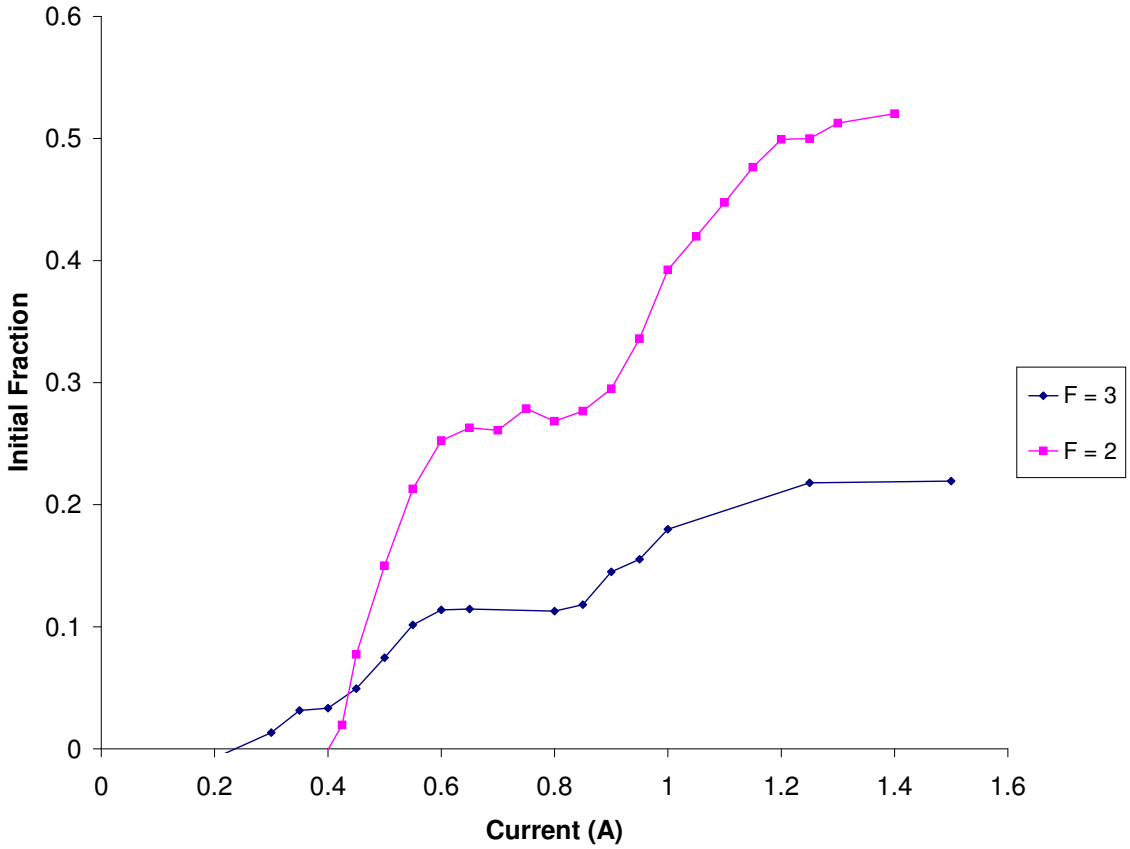

Figure 4.6: A plot of the fraction of the ^{85}Rb $|F=3\rangle$ and $|F=2\rangle$ atoms loaded into the magnetic trap from a MOT as a function of magnetic coil current, experimentally determined in order to find the optimal currents for spin filtering. For $|F=3\rangle$, $|3\,3\rangle$ is trappable at $\sim$0.2 A, $|3\,2\rangle$ at $\sim$0.4 A, $|3\,1\rangle$ at $\sim$0.85 A, and $|3\,0\rangle$ (not shown) at $\sim$4.5 A. For $|F=2\rangle$, $|2\,-2\rangle$ becomes trappable at $\sim$0.3 A, and $|2\,-1\rangle$ at $\sim$0.85 A. No data exists for $|2\,0\rangle$, theoretically estimated to be trappable at currents past $\sim$7 A.

Chapter 5

Numerical Methods and Results

A number of numerical simulators were used during the tenure of my project. One is incomplete at the time of this writing, and the other two were mostly complete before the start of my project. I shall therefore describe each method in brief only.

5.1 Loss Cross-Section Calculator

The loss cross-section calculator, written in FORTRAN77 by David Fagnan, calculates the total and loss cross-section of atoms in a trap due to elastic collisions with background atoms [13]. The code utilizes the theoretical machinery outlined in Chapter 2 to calculate $|f(k,\theta)|^2$, which it uses to determine the loss cross-section σ. The code first finds the value of the coefficients of the Bessel and Neumann functions that asymptotically describe a scattered wavefunction via the logarithmic derivative method outlined by B.R. Johnson [23]. It then converts these values to T-matrix values, which it then uses to calculate the scattering amplitude and total cross-section σ_{total} via Eqs. 2.34 and 2.35 [13]. Finally, it uses Gauss-Legendre integration of Eq. 2.12 to determine the total loss cross-section σ, and Boltzmann averages the total and loss cross-sections to determine $\langle\sigma_{total}v\rangle$ and $\langle\sigma v\rangle$ [13].

Fagnan's original code was utilized and optimized to calculate scattering between trapped Rb and background Ar (to produce the theoretical curve in Fig. 1.1). Aside from changing the atomic mass of the background scatterer and modifying the C_6 and C_{12} interaction values, modifying the code to determine Rb-Rb collisional cross-sections required increasing the number of partial waves used in the calculation by a factor of approximately four for any given velocity. The code was used to determine an Rb-Rb $\langle\sigma v\rangle$ versus trap depth curve (Fig. 1.2), used in the thesis for analyzing the hyperfine dependence data [1].

[1] Note that the Rb-Rb interaction potential is independent of the isotopes being used in our experiment. The difference in ^{87}Rb-^{87}Rb, ^{87}Rb-^{85}Rb and ^{85}Rb-^{85}Rb $\langle\sigma v\rangle$ is solely due to the mass the collision constituents, making this difference 1 - 2% of $\langle\sigma v\rangle$ at best. All Rb-Rb $\langle\sigma v\rangle$ cited in this thesis are for ^{87}Rb-^{87}Rb.

The code has also been modified to perform a number of different calculations, including calculating velocity-averaged heating rates due to elastic background collisions (Eq. 2.20), or a velocity averaged differential cross-section $\left\langle \frac{d\sigma}{d\Omega} \right\rangle$.

5.2 Magnetic Trap Simulator

5.2.1 Overview of the Simulator

At the outset of this project, it was believed that a direct simulation of the atoms in the trap would be the most viable method of investigating heating. A simulator would additionally be able to replicate some of the more complex details of our trap, such as the exact shape of the potential well and Majorana losses. The code, written in Python, is nearing completion.

The simulation begins by creating an ensemble of trapped atoms. These atoms have kinetic energies determined from a Maxwell-Boltzmann distribution, and are distributed in space according to a user-defined function (a Gaussian is currently being used). The simulation then uses the velocity verlet method to simulate how the atoms evolve in the trap over time. The trapped atoms are periodically subjected to collisions, in accordance with the rate of collisions from a background gas of a certain number density and a Maxwell-Boltzmann velocity distribution. The code derives the momentum imparted to the trapped atom in the collision from differential cross-sections. The incident direction of the background particle is assumed to be random, and therefore this momentum is given a random direction and added to the momentum of the trapped particle. This negates the problem (mentioned in Section 2.1.1) of Eq. 2.4 becoming invalid for collisions in which the trapped atom already has significant kinetic energy. Since collisions are treated individually, the simulator also allows us to determine the loss and heating rates in trapped ensembles with a distribution of energies.

Because of how time-consuming calculating cross-sections is, differential cross-section values at various angles and k-values were calculated using a heavily-modified version of the loss cross-section calculator. The simulator runs a two-dimensional spline across these values in order to determine $\frac{d\sigma}{d\Omega}$ for any θ and k.

5.2.2 Changes in the Scattering Amplitude due to Varying the C_{12} Coefficient

The C_{12} value for Rb-Ar collisions was calculated (instead of determined from literature) from the C_6 value (280 atomic units) and assuming a 50 cm^{-1} well - this gave 8.603×10^7 a.u. The same calculation method was initially used for Rb-Rb collisions, giving 2.154×10^{10} a.u. ($C_6 = 4430$ a.u., from Bali *et al.*) for the Rb-Rb C_{12} value, used to create Fig 1.2 [3]. Patil and Tang give a C_{12} value of 1.19×10^{10}, which is the C_{12} value eventually used to calculate differential cross-sections for the simulator [27]. It is the case, however, that the loss and total cross-sections of Rb-Rb collisions are

constant to within an 11% deviation over a wide range of C_{12} values, from 10^2 to 10^{10} (see Fig. 5.1). The same is true for Rb-Ar collisions, which is why it was set somewhat arbitrarily when calculating Rb-Ar $\langle \sigma v \rangle$ with respect to trap depth.

What does change when C_{12} is varied is the shape of the differential cross-section as a function of θ, as seen in Fig. 5.2. At C_{12} values of less than 10^9 a.u., there are significant high frequency oscillations in the differential cross-section across all values of θ. Starting at values of 10^9, the differential cross-section at high values of θ begin to "smooth out", and by 10^{12} the differential cross-section curve appears largely free of oscillations except at angles smaller than $\theta =\sim 0.02$. These changes to the differential cross-section eventually impact the total cross-section, but this occurs only past 5×10^{10}. We believe that the oscillations at low values of C_{12} are due to the inclusion of large numbers of partial waves to allow for convergence of the cross-section values [18]. As the C_{12} value becomes larger, the potential becomes more and more repulsive, which may lead to the changes seen in Fig. 5.2. Why exactly these changes occur when C_{12} passes 10^9 are not entirely clear from my investigation. Because both the loss cross-section calculator and the simulator output aggregate loss rates, we need only worry about total and loss collisional cross-sections. I have thus chosen a value of $C_{12} = 1.19 \times 10^{10}$, in accordance with Patil and Tang, for the simulator calculations. It may be, however, that the difference in differential cross-section due to varying C_{12} value is worth investigation in the future.

5.3 Multi-Channel Loss Cross-Section Calculator

The multi-channel loss cross-section calculator, written in FORTRAN90 by Zhiying Li, calculates the total and loss cross-section of trapped atoms due to collisions with background atoms taking into consideration the hyperfine states of the collision constituents. For the calculations performed for this thesis, the code considers a trapped ^{87}Rb or ^{85}Rb ensemble composed of a single hyperfine state (ex. $|3\,3\rangle$) experiencing collisions with a background gas composed of ^{87}Rb and ^{85}Rb. The distribution of ^{87}Rb and ^{85}Rb $|F\,m_F\rangle$ states is assumed to be uniform, meaning incoming background atoms have an equal probability of being in any ground state $|F\,m_F\rangle$. It includes the contributions to $\langle \sigma v \rangle$ of various hyperfine state changing inelastic collisions, as well as changes to $\langle \sigma v \rangle$ due to the whether the combined spin state of the collision constituents is a triplet or a singlet.

The assumption of a uniform distribution of $|F\,m_F\rangle$ states for the background gas means that the contribution to $\langle \sigma v \rangle$ from the identical particle phenomenon detailed in Section 2.5 would be invariant to changes in trapped ensemble $|F\,m_F\rangle$ state. The effect is also small, as identical constituent collisions represent only a small fraction of all collisions: numerical calculations using a modified version of the loss cross-section calculator indicate that the effect is on the order of 5% of $\langle \sigma v \rangle$. For these reasons, changes in $\langle \sigma v \rangle$ due to identical particle collisions were not included in the calculations.

The resulting calculations verified our $\langle \sigma v \rangle$ calculations: the multichannel $\langle \sigma v \rangle$ deviated only

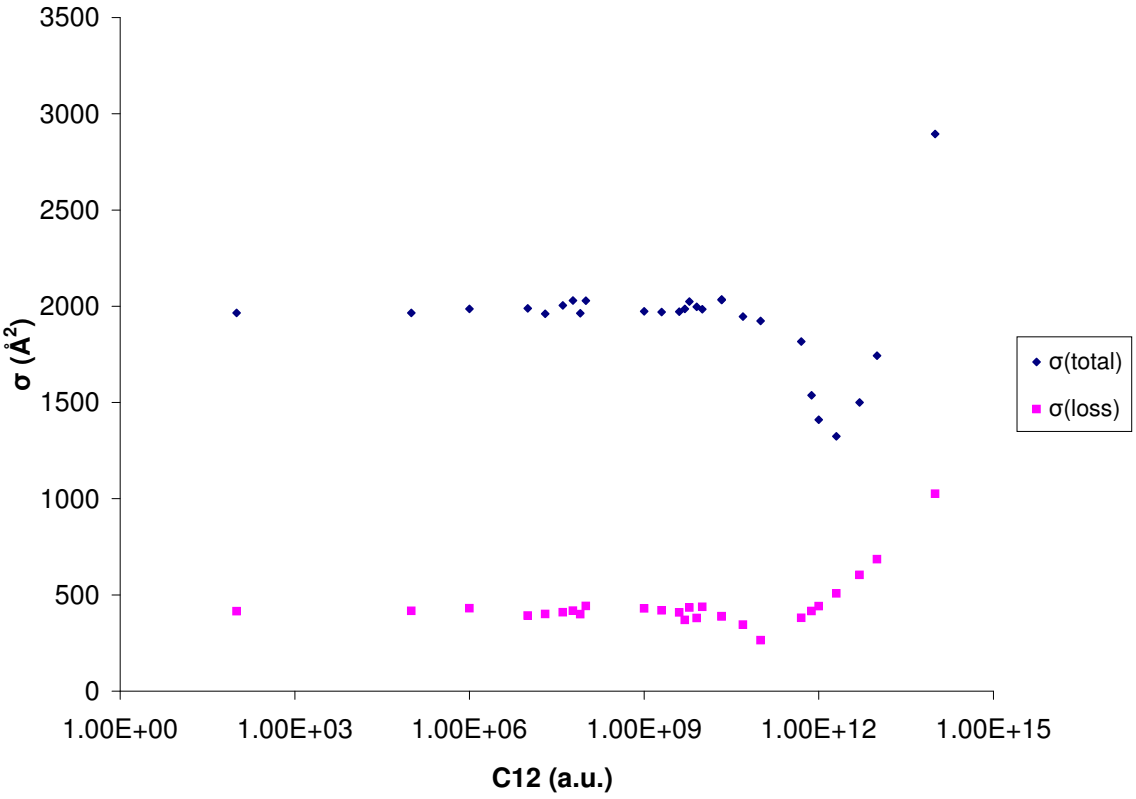

Figure 5.1: A semilog plot of numerically determined σ (loss cross-section) and σ_{total}, for collisions between trapped Rb and background Rb travelling at 293 m/s, as functions of C_{12} value. σ is calculated for a 1 K trap. The value of both σ (loss cross-section) and σ_{total} are constant to within $\sim 10\%$ until $C_{12} \geq\sim 5 \times 10^{10}$ atomic units.

by several percent from the $\langle \sigma v \rangle$ calculated by Fagnan's loss cross-section calculator [21]. The deviation is smaller than the one-sigma error bars reported in our experimental data (Fig. 1.2).

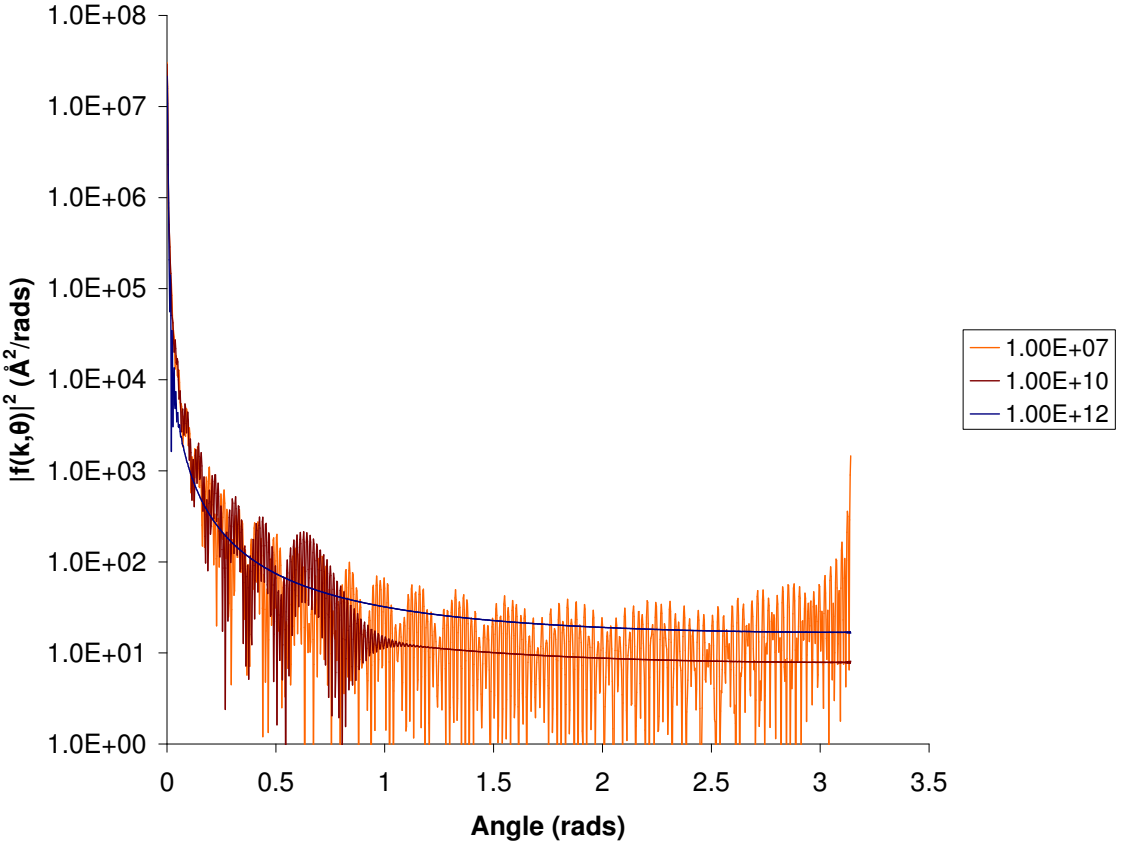

Figure 5.2: A semilog plot of numerically determined $|f(k,\theta)|^2$ as a function of θ for collisions between trapped Rb and background Rb travelling at 293 m/s. Each curve was calculated using a different C_{12}, noted in the legend in atomic units. As C_{12} value increases, the number of oscillations seen in the $|f(k,\theta)|^2$ curve decreases.

Chapter 6

Procedure and Experimental Results

6.1 General Procedure

Our standard method of discerning properties of our magneto-optical trap is by taking a MOT loading curve. This is done by starting with a steady-state MOT ensemble, turning off the magnetic field for 500 ms to eject the ensemble, and then turning the field back on and letting the trap load once again. This trap loading follows Eq. 3.1, and therefore fitting an exponential decay to the curve allows us to determine the loss rate $\langle \Gamma_{total} \rangle$. Fitting a straight line to the section of the loading curve just after the magnetic coils turn back on allows us to estimate the initial MOT loading rate, R. Fig. 6.1 is an example of a MOT loading curve.

The magnetic trap does not use the lasers, and this means we cannot continuously determine the number of trapped atoms via laser fluorescence as we do with the MOT. Instead, we begin with a steady state MOT, further cool the atoms, and then turn off the lasers while simultaneously ramping up the magnetic field gradient from 27.8 G cm^{-1} along the z-axis to the final desired value (typically around 278.5 G cm^{-1} along the z-axis) in 7.5 ms. If Zeeman pumping is used, it is performed immediately before ramping up the magnetic field gradient. The pumping itself takes 0.8 ms, while the gravity filtering takes 200 ms. Once this is complete, the trap is left to evolve on its own for some designated time. At the end of this time, the magnetic field is ramped back down over 15 ms [1], and the lasers are flashed back on, taking a measurement of the ensemble fluorescence, before the magnetic fields are turned off to empty the trap. The magnetic fields are then turned on after 500 ms of wait time, creating a MOT loading curve from which we can determine the initial loading rate R.

From this procedure, a single point along the magnetic trap loss curve is determined (see Fig. 6.2). Unlike the loading curves of Fig. 6.1, loss curves values are normalized to the steady state

[1] This is not enough time for atoms to move across the length of the trap, which is why procedures like RF knifing and Zeeman pumping require more than 100 ms of wait time to ensure all atoms are lost from the trap

MOT value, and therefore represent the fraction of atoms from the original MOT ensemble that were successfully loaded into the magnetic trap and have not been lost over a certain magnetic trap hold time (henceforth referred to as "trapped fraction"). A number of loss-determination curves must then be produced in order to fill out the magnetic trap loss curve.

Rb-Rb collisions were the dominant collisions in our trap for all experiments described in this section.

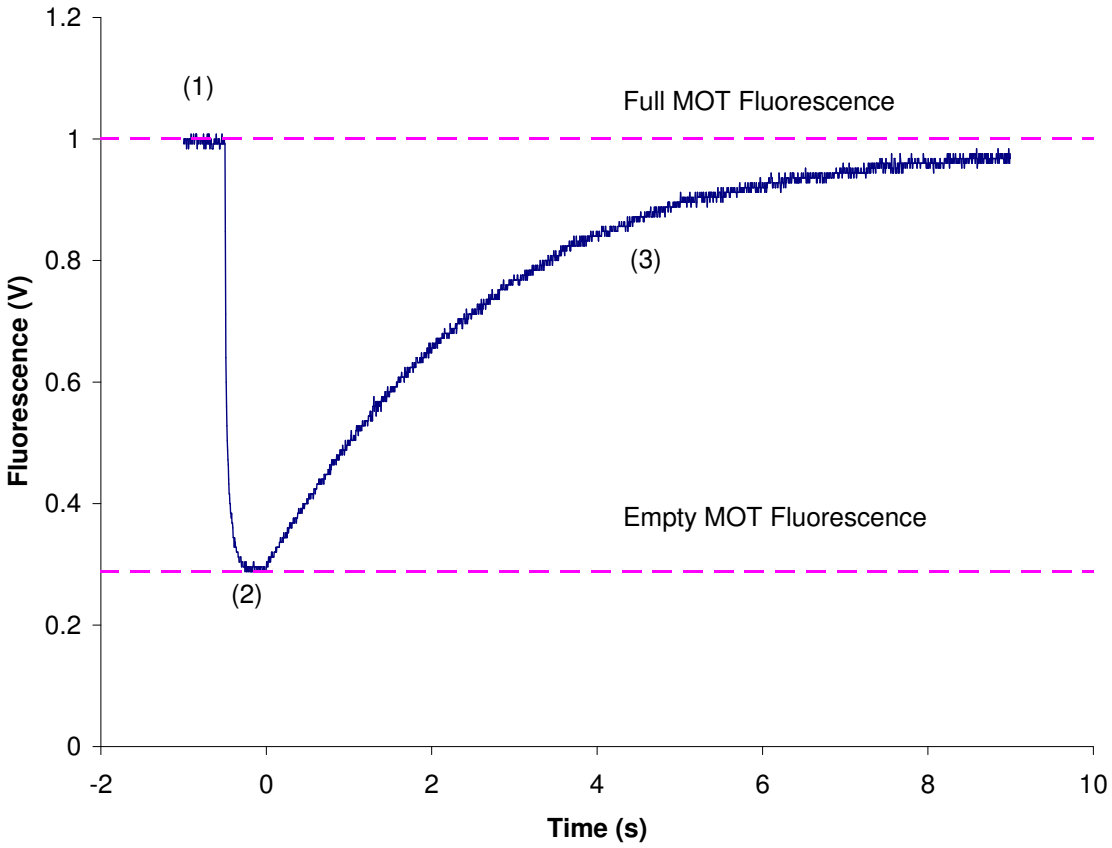

Figure 6.1: An example of a MOT loading curve. The curve is produced by (1) starting with a steady-state MOT ensemble, (2) turning off the magnetic field for 500 ms to eject the ensemble, and then (3) turning the field back on and letting the trap load once again. The fluorescence seen by the photodiode is not zero when there is no trapped ensemble at (2) because some laser light still scatters off the MAT vacuum cell. The resulting curve is an exponential rise from the zero-level at (2) to the MOT steady state fluorescence.

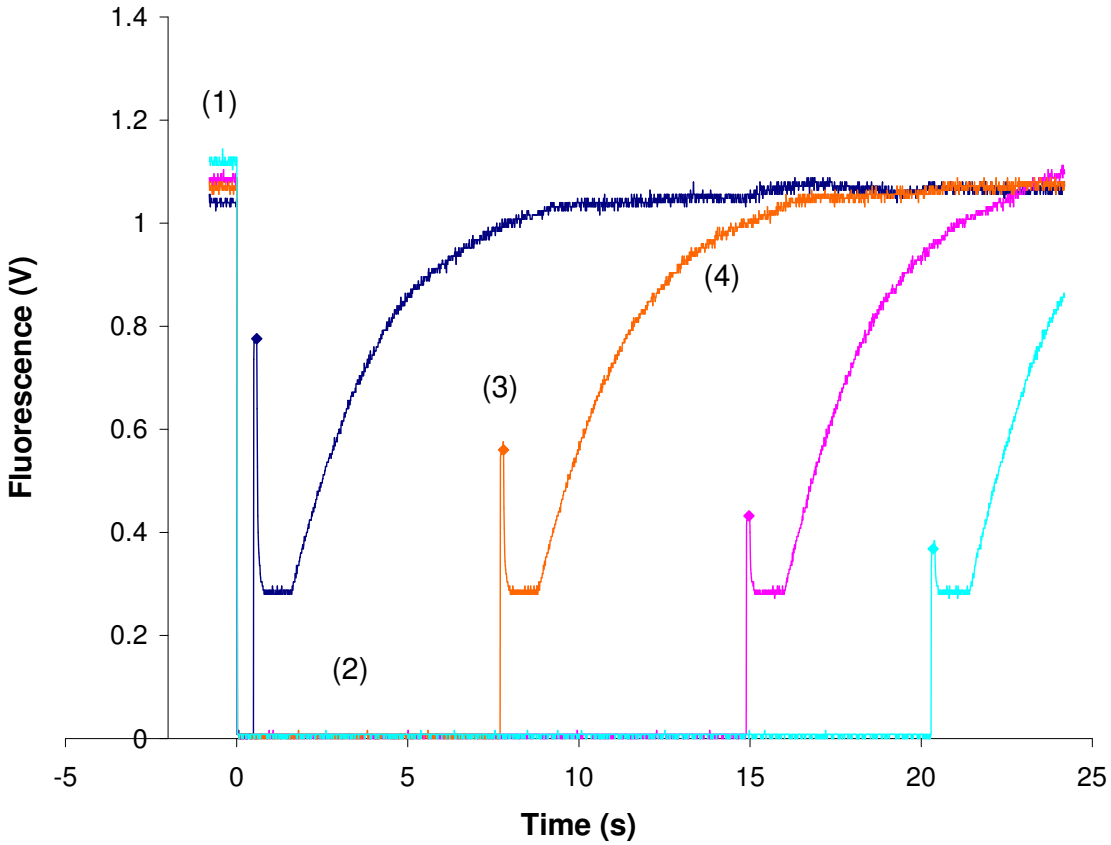

Figure 6.2: An example of a series of magnetic trap loss-determination curves. Each curve (taking the orange curve as our example) begin with a steady state MOT (1). We then cool the atoms, and turn off the lasers while simultaneously ramping up the magnetic field gradient in 7.5 ms. If Zeeman pumping is used, it is performed immediately after that for 200 ms. Once this is complete, the trap is left to evolve on its own (2) for some designated time (during which the lasers are off, so no fluorescence reaches the photodiode). At the end of this time, the magnetic field is ramped back down over 15 ms, the lasers are flashed back on, taking a measurement of the ensemble fluorescence (3), before the magnetic fields are turned off to empty the trap. The magnetic fields are then turned on, creating a MOT loading curve (4). Each of these loss-determination curves determines a single value on a magnetic trap loss curve (the multicoloured diamonds on each curve), which can be strung together to create an exponential decay. Note that the MOT steady state value appears to increase over time - this is possibly due to heating of the magnetic coils. Because we normalize point (3) to the MOT steady state fluorescence to produce a trapped fraction, small amounts of deviation such as seen in this graph can be neglected.

6.2 Measurement of Trap Energy Distribution

The first attempt at deducing the rate of heating in the trap was to measure directly how many atoms of certain energies were being trapped. Sweeping the RF knife from some lower frequency ν to an upper frequency corresponding to an energy above the trap depth eliminates all trapped atoms with energies larger than $E(\mathbf{x})$ (to use terminology defined in Section 3.3). Therefore, varying the lower frequency of this sweep allows us to explore the energy distribution within the trap. Because each RF knife sweep will eliminate all atoms *above* a certain energy, only one point in the distribution can be determined per experimental run, it takes many identical runs to fully map out a trap energy distribution.

We performed a number of experiments using ^{87}Rb $|1,-1\rangle$ where a magnetic trap was held for a certain amount of time, and then the energy distribution of that trap was determined. ^{87}Rb $|1,-1\rangle$ was chosen so that no consideration of the effect Bouyer *et al.* noted, of low RF efficacy due to having to transition trapped atoms across multiple trappable $|F\,m_F\rangle$ states, was needed [6]. The trap depth was chosen to be 3.14 ± 0.84 mK for the experiments so that for every Rb-Rb trap loss collision, there was also one Rb-Rb heating collision, per Eq. 2.19 and Fig. 1.2.

An example of our results is Fig. 6.3. This curve is similar to the metastable He ensemble energy distribution (in a Ioffe-Pritchard trap) found by Browaeys *et al.* using their RF knife [7].

If heating were evident in the trap, the energy distribution determined would have shifted with increasing hold time toward a distribution with higher average energy. Our experiments showed, however, this is not the case, as can clearly be seen in Fig. 6.3. Believing it may be possible that the system was in a sort of steady state where shifts in the energy distribution are not apparent, we then modified the experimental procedure so that at the start of the magnetic trap hold, we used an RF sweep to eliminate the more energetic half of the trapped atoms. The result was an apparent increase in shot noise in the system, but over long periods of time there was still no discernable heating of the atoms (Fig. 6.4). For Fig. 6.3, the total number of trapped atoms had decreased by more than 35% over 8000 ms due to elastic collisions that do result in immediate trap loss, indicating that the other 50% of the trapped atoms have undergone an average of 0.7 heating collisions over the same amount of time. The fact that no change is seen may indicate that the majority of these collisions impart extremely small amounts of energy to the trapped ensemble.

It was eventually deemed, after multiple negative results using this method, that we needed to switch to a method that is aggregate, to more easily distinguish small amounts of heating.

6.3 Measurement of Heated Fraction

A "heated fraction" measurement is an aggregate method of determining the heating rate within a magnetic trap. At the beginning of the magnetic trap hold, all atoms of energy E_{mid} or higher in the trap are eliminated using an RF sweep with lower frequency limit ν for 125 ms. The trap

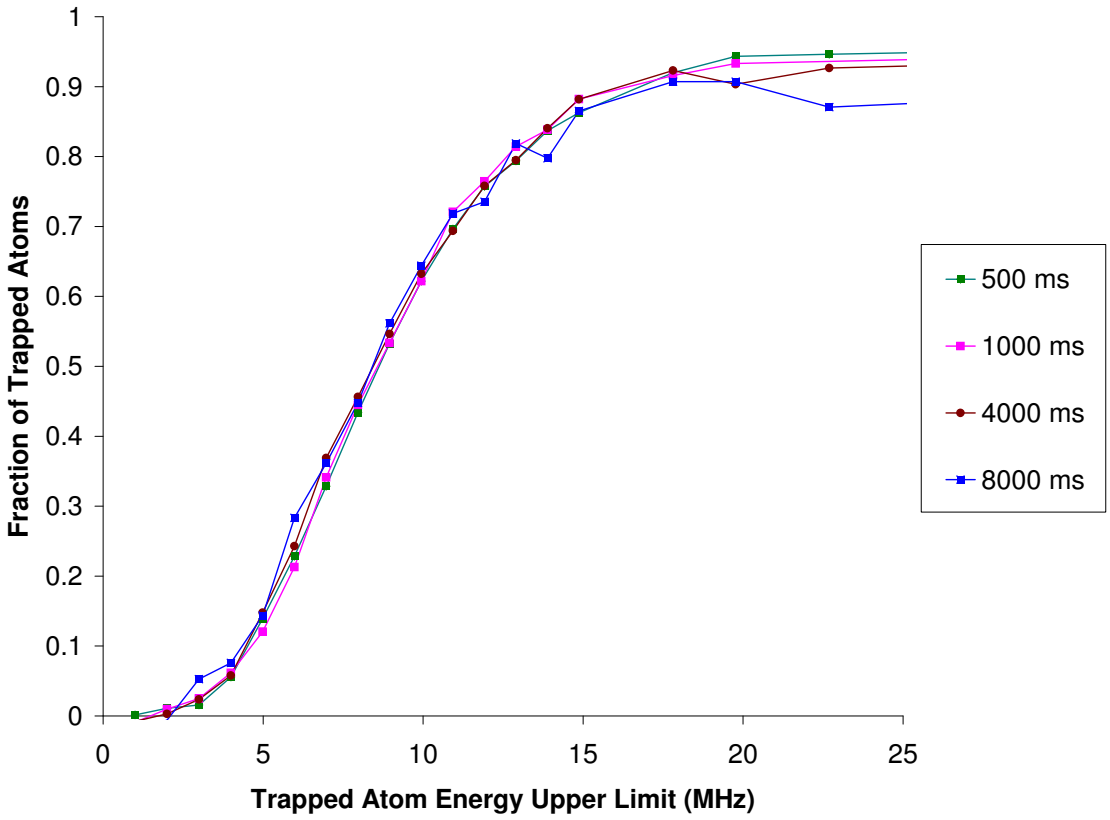

Figure 6.3: Cumulative energy distribution curves of an ^{87}Rb $|1,-1\rangle$ 3.14 ± 0.84 mK magnetic trap at various hold times (denoted in the legend), determined by 125 ms RF sweeps at varying lower frequencies. Each data point on a distribution curve indicates the fraction of atoms trapped with some particular energy (in MHz) or lower (at some time). Over 8000 ms, the total number of trapped atoms decreased by more than 33% (each curve is normalized to the total number of atoms in the trap at the time to eliminate trap loss biases), but no discernable heating is seen.

is then allowed to evolve over some time; during this time, the RF knife can be used to set the trap depth. At the end of this hold time, the RF knife is again swept with lower limit ν for 125 ms, eliminating any atoms that might have been heated past E_{mid} during the hold time. This gives trapped fraction measurement $F_W(t)$. A second experimental run with an identical initial procedure is then performed, but at the end no RF knife is used, giving us $F_O(t)$, the trapped fraction that includes all trapped atoms regardless of energy. The heated fraction is defined as

$$F_H(t) = 1 - \frac{F_W(t)}{F_O(t)}. \tag{6.1}$$

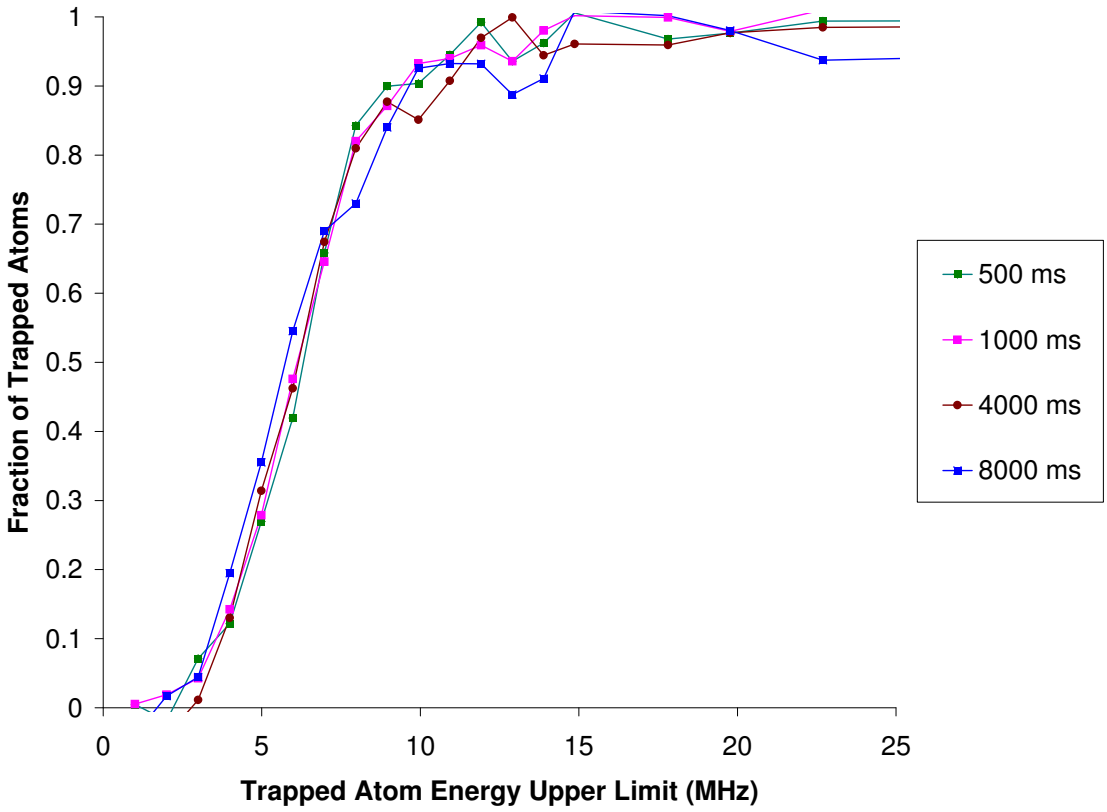

Figure 6.4: Cumulative energy distribution curves of an ^{87}Rb $|1-1\rangle$ 3.14 ± 0.84 mK magnetic trap at various hold times (denoted in the legend), determined by 125 ms RF sweeps at varying lower frequencies. The RF knife was also used to eliminate all atoms of energy 8 MHz or above at the beginning of each trap hold. Each data point on a distribution curve indicates the fraction of atoms trapped with some particular energy (in MHz) or lower (at some time). Over 8000 ms, the total number of trapped atoms decreased by more than 20% (each curve is normalized to the total number of atoms in the trap at the time to eliminate trap loss biases). This lower loss rate may be because the average energy of the trapped atoms is lower and therefore more incoming collisions result in heating rather than trap loss, but due to the significant increase in noise in the distributions it is not possible to determine if any heating has actually occured.

Because initially the RF knife sets $F_W = F_O$, this value can be understood as the fraction of atoms that have migrated from the 0 - E_{mid} energy bin to the E_{mid} - trap depth U_0 energy bin due to heating collisions. Therefore, a very crude estimate of the energy E of the trapped ensemble is

$$E \approx NF_H(t)\frac{U_0 + E_{mid}}{2} + \frac{NE_{mid}}{2}(1 - F_H(t))$$

$$= N(\frac{U_0}{2}F_H(t) + \frac{E_{mid}}{2}), \tag{6.2}$$

where N is the number of atoms in the trap. If we want the heating rate per atom, i.e. the average energy $\langle E \rangle$ imparted to a single trapped atom per second, we take the derivative with respect to time and divide by N:

$$\frac{d\langle E \rangle}{dt} \approx \frac{U_0}{2}\frac{dF_H}{dt}, \tag{6.3}$$

Initial attempts at determining heated fraction over time gave us plots such as Fig. 6.5, which showed two surprising features. The first was that the initial F_H value did not appear to be zero, even though the RF knife was supposed to have eliminated all atoms from the high energy bin. It was initially believed the existence of the non-zero initial heated fraction was because the RF knife was inadvertently heating the rest of the trapped atoms. Heated fraction experiments where the trap depth was not set using the RF knife, however, showed the same non-zero initial F_H. The second was that there was a significant amount of noise when taking the measurements, which suggested that the average of many sets of heated fraction data was needed.

6.3.1 Relationship Between Heated Fraction and Trap Depth

We attempted to determine the relation between F_H and trap depth. This was determined by taking F_H measurements, as detailed above, for a number of different trap depths all set using the RF knife. For the experiment, E_{mid} was set to 13.9 ± 1.1 MHz (0.667 ± 0.053 mK), and an initial RF sweep was used to eliminate all atoms of energy 13.9 MHz or lower for each data run. Each F_H curve was built out of data from five different experimental runs: five sets of F_W and F_O were taken for each point on each F_H curve. From this set, 25 values of F_H are determined. From these 25 values, both the F_H average and an estimate of the shot noise one-sigma error can be found. The resulting F_H curves are plotted in Fig. 6.6. These curves were analyzed with linear best fits on Gnuplot; the results are given in Table 6.1 and plotted in Figs. 6.7 and 6.9.

Let us assume that our trapped ensemble starts with negligible energy (untrue in our traps). From Eq. 2.17, $n_{Bg}\langle qv \rangle$ is a crude first estimate of the rate of heating collisions in the trap, where q is defined in Eq. 2.18. $n_{Bg}\langle qv \rangle$ for a trap of depth E_{mid}, which we designate $n_{Bg}\langle qv \rangle_m$, would be a crude estimate for the rate of collisions that do not impart enough energy into the trapped atoms to elevate them above E_{mid} and be counted as part of the heated fraction. $n_{Bg}\langle qv \rangle$ - $n_{Bg}\langle qv \rangle_m$ would then be a crude measure for the heated fraction rate. We plot the heated fraction rate versus $\langle qv \rangle$ - $\langle qv \rangle_m$ in Fig. 6.8.

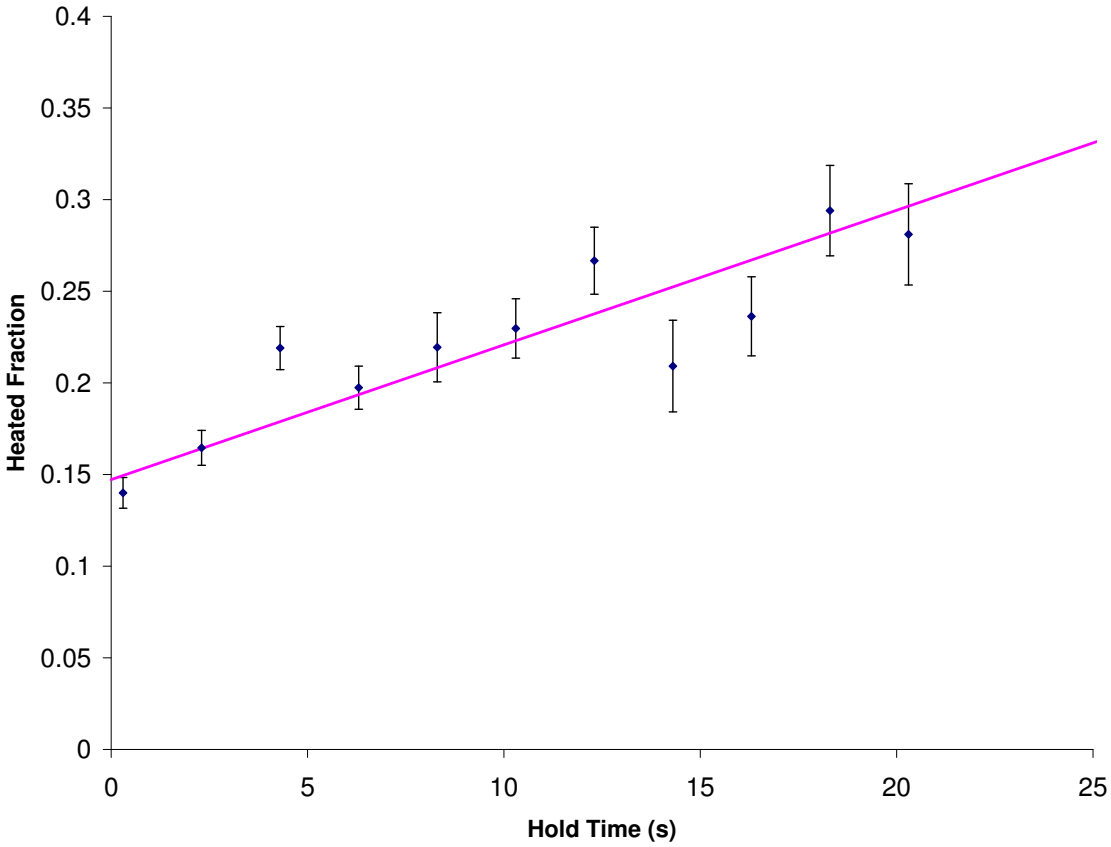

Figure 6.5: Plot of F_H vs. magnetic trap hold time for ^{87}Rb $|1-1\rangle$ in a 1.3 ± 0.14 mK trap. Magnetic coil gradient was set to 5 A, but the 1.3 mK trap depth was set by a continuous RF sweep from 27.53 MHz to 90 MHz over the magnetic trap hold time. An initial RF sweep was used to eliminate all atoms of energy 7.96 ± 0.87 MHz (0.382 ± 0.042 mK) or lower. The error shown is derived from best fitting for the trapped fraction, and is not a measure of the shot noise of the points. A linear best fit performed on Gnuplot, plotted here in magenta, gave an initial fraction of 0.1473 ± 0.0077, and a slope of 0.0073 ± 0.0012 s^{-1}. Using Eq. 6.3, this gives us a heating rate per atom of $\sim$0.2 MHz s^{-1}, or $\sim$9 μK s^{-1}.

Table 6.1: Table of Gnuplot fit results for the F_H curves in Fig. 6.6.

Trap Depth (MHz)	F_H Slope (s^{-1})	$F_H(t=0)$	$d\langle E\rangle/dt$ (MHz s^{-1})	$d\langle E\rangle/dt$ (μK s^{-1})
19.8 ± 1.6	0.0032 ± 0.0010	0.0679 ± 0.0082	0.031 ± 0.010	1.50 ± 0.49
29.5 ± 2.3	0.00370 ± 0.00095	0.1127 ± 0.0093	0.054 ± 0.014	2.62 ± 0.67
39.1 ± 3.1	0.0058 ± 0.0014	0.115 ± 0.014	0.113 ± 0.027	5.4 ± 1.3
57.9 ± 4.6	0.0069 ± 0.00078	0.1296 ± 0.0085	0.200 ± 0.022	9.6 ± 1.1

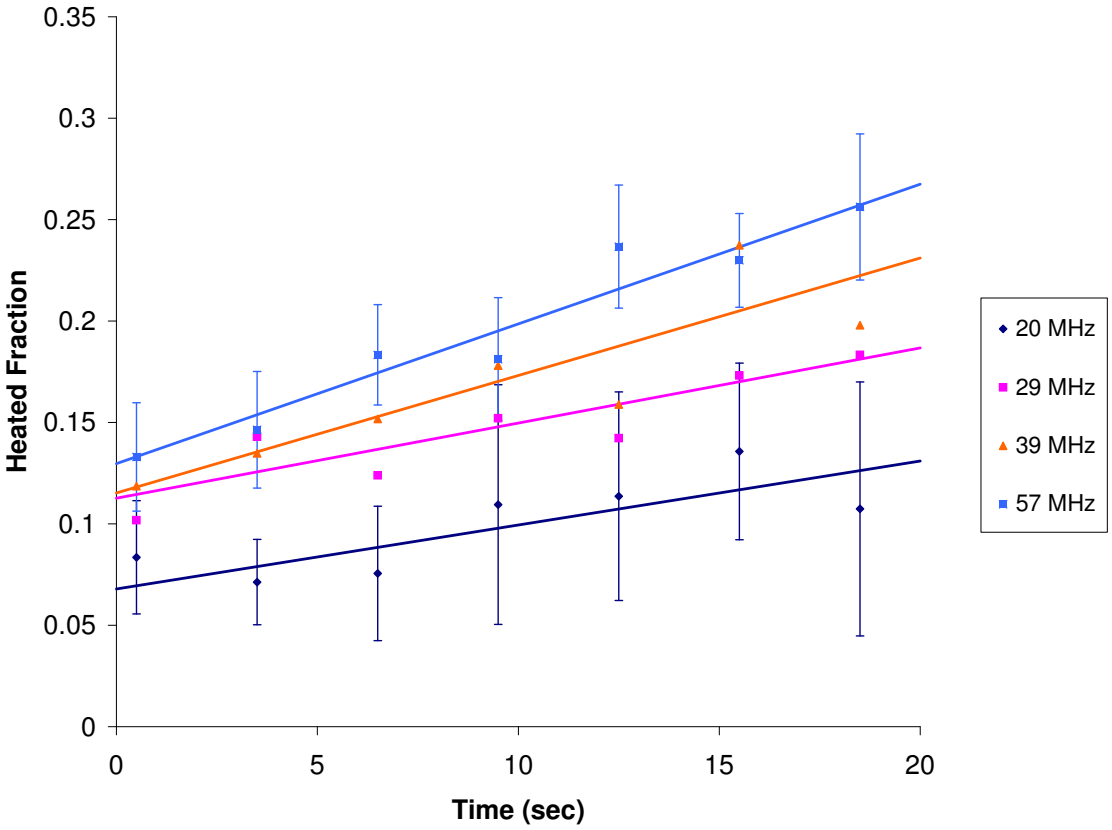

Figure 6.6: Plot of F_H vs. magnetic trap hold time for ^{87}Rb $|1-1\rangle$ curves for traps of varying depth. Magnetic coil gradient was set to 7 A, but the trap depth was set by a continuous RF sweeps. The four depths used were 19.8 ± 1.6 MHz (0.949 ± 0.074 mK), 29.5 ± 2.3 MHz (1.41 ± 0.11 mK), 39.1 ± 3.1 MHz (1.88 ± 0.15 mK) and 57.9 ± 4.6 MHz (2.78 ± 0.22 mK). E_{mid} was set to 13.9 ± 1.1 MHz (0.667 ± 0.053 mK). Error bars for 19.8 and 57.9 MHz F_H curves are included to give a visual example of the level of shot noise in the system.

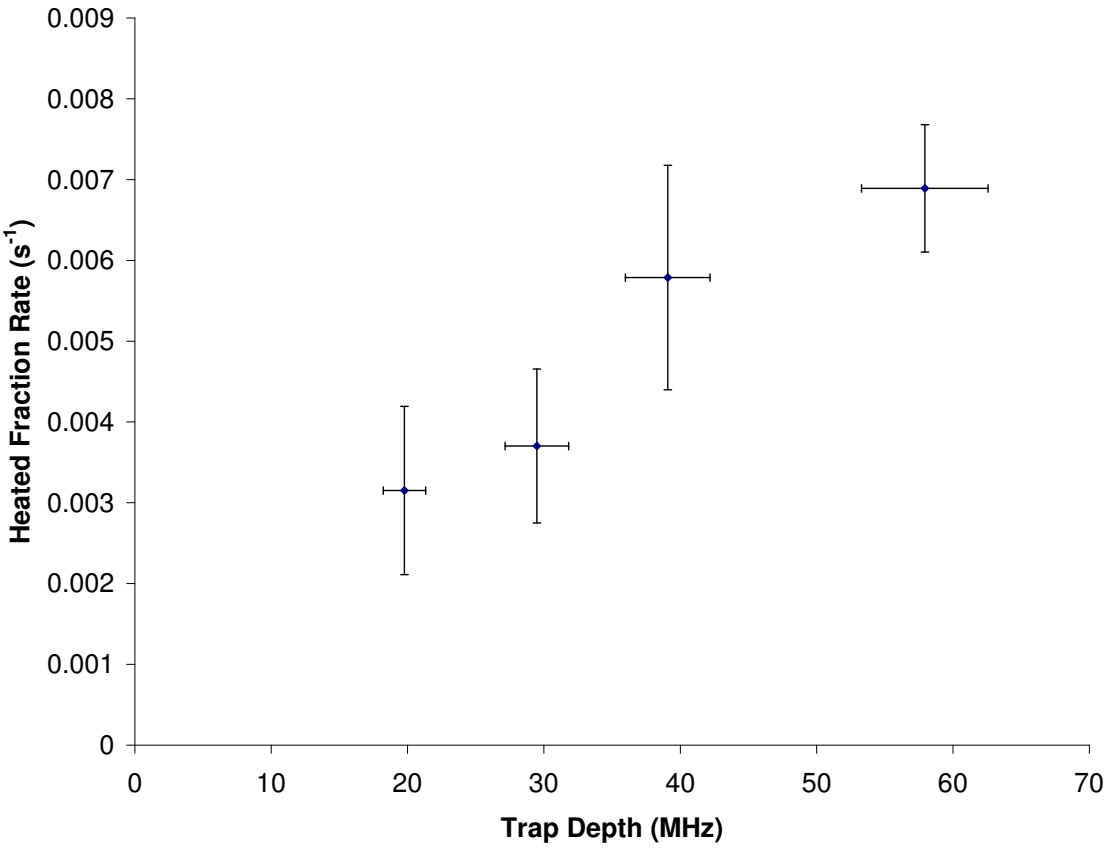

Figure 6.7: Plot of Fig. 6.6 F_H best fit slopes vs. trap depth.

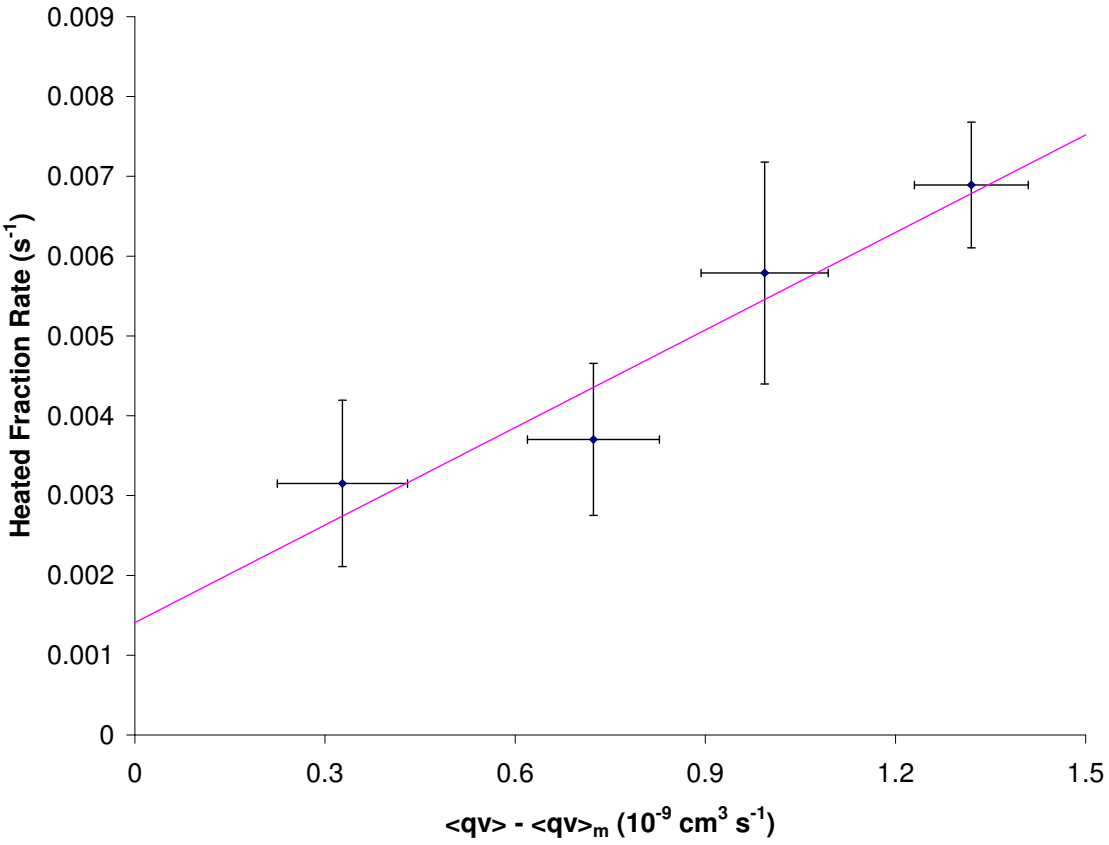

Figure 6.8: Plot of Fig. 6.6 F_H best fit slopes vs. $\langle qv \rangle$ - $\langle qv \rangle_m$. To determine $\langle qv \rangle$ and $\langle qv \rangle_m$, the estimate $\langle qv \rangle$ = $\langle \sigma_{total} v \rangle$ - $\langle \sigma v \rangle$ was used. Theoretically, the relationship between the two values is, to first order, linear, and the slope is n_{Bg}. A linear best fit to the data was performed in Gnuplot, and is plotted alongside the data. The fit's slope is $4.07 \pm 0.75 \times 10^6$ cm^{-3} and intercept is 0.00141 ± 0.00073 s^{-1}.

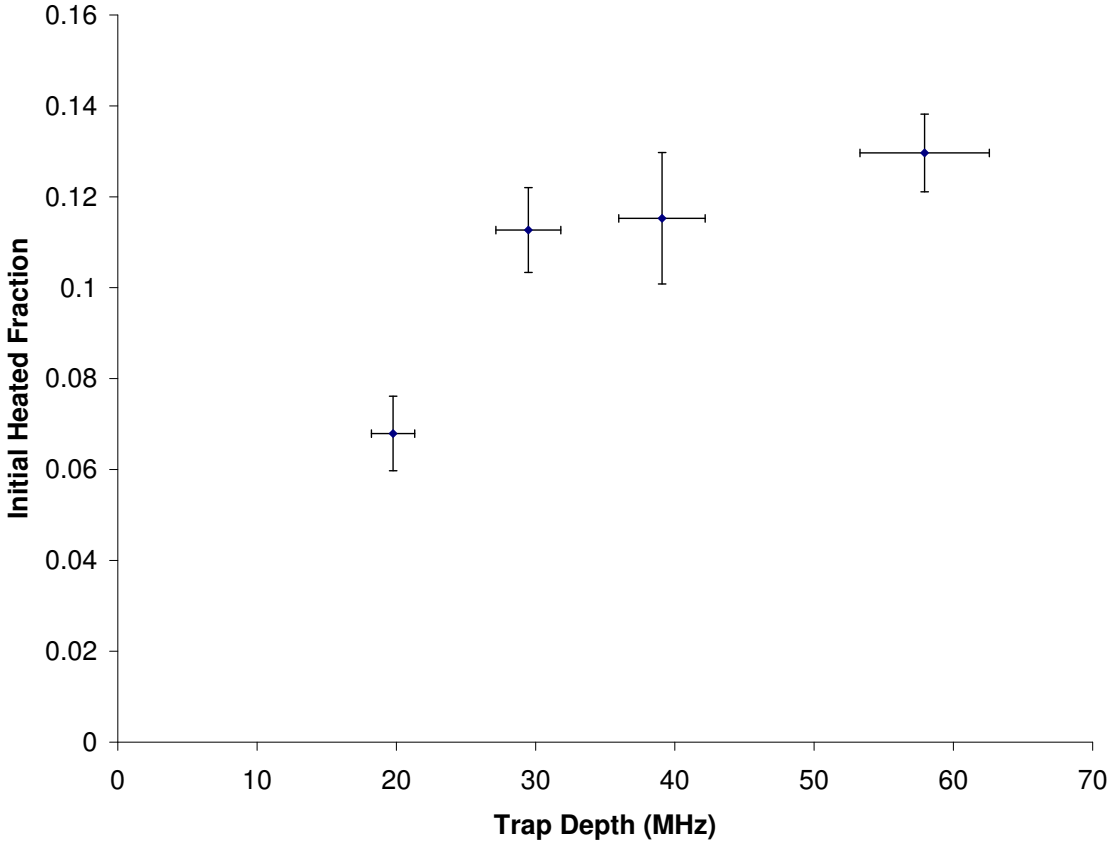

Figure 6.9: Plot of Fig. 6.6 F_H initial value (best fit y-intercept) vs. trap depth.

6.3.2 Relationship Between Heated Fraction and Rb Number Density

We also determined the relationship between F_H and Rb background number density for two different trap depths, 1.30 ± 0.14 mK and 2.00 ± 0.22 mK. E_{mid} was again set to 13.9 ± 1.1 MHz (0.667 ± 0.053 mK). Because the ion and getter pumps actively remove Rb from the system (see Section 4.2), we cannot set Rb number density to a constant level. Instead, we inject Rb into the system, and then take F_H curves over the course of the equilibration process, which naturally varies Rb background number density over time. As Rb pressure cannot directly be measured, MOT loading rate R is used as an indicator of density. All F_H curves were taken multiple times, but because the equilibration process is an exponential decay, fewer data sets were taken of high number density F_H curves compared to low density F_H curves. The resulting curves were analyzed with linear best fitting on Gnuplot. Fit results are plotted in Figs. 6.10 and 6.11. The plot of heated fraction rate vs. MOT loading rate R, Fig. 6.10 appeared to be linear, and therefore linear best fitting was performed on Gnuplot. The results are given in given in Table 6.2.

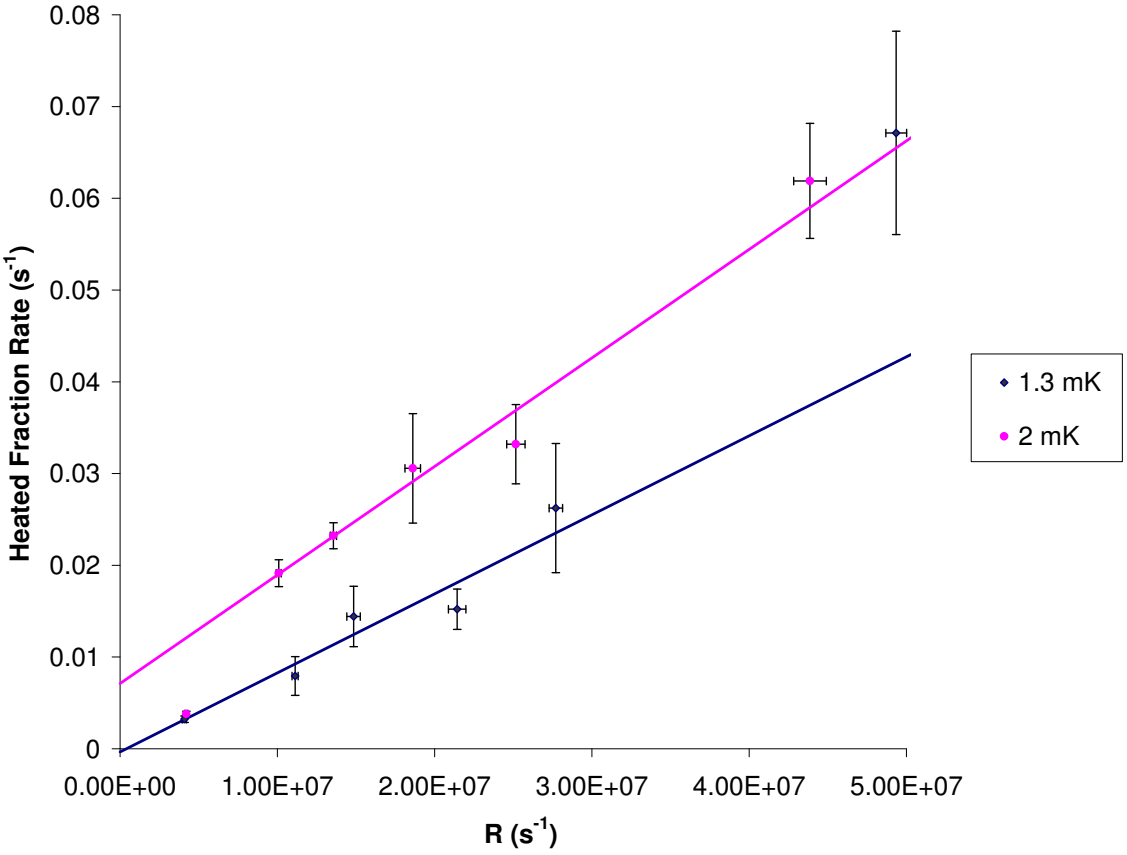

Figure 6.10: Plot of the relationship between F_H rate and MOT loading rate R for a 1.30 ± 0.14 mK trap and 2.00 ± 0.22 mK trap (set using continuous RF knife sweeps with lower frequencies 27.53 and 42.72 MHz, respectively). E_{mid} was set to 0.667 ± 0.053 mK. These data points were determined by performing Gnuplot best fits on F_H curves taken over a number of R values.

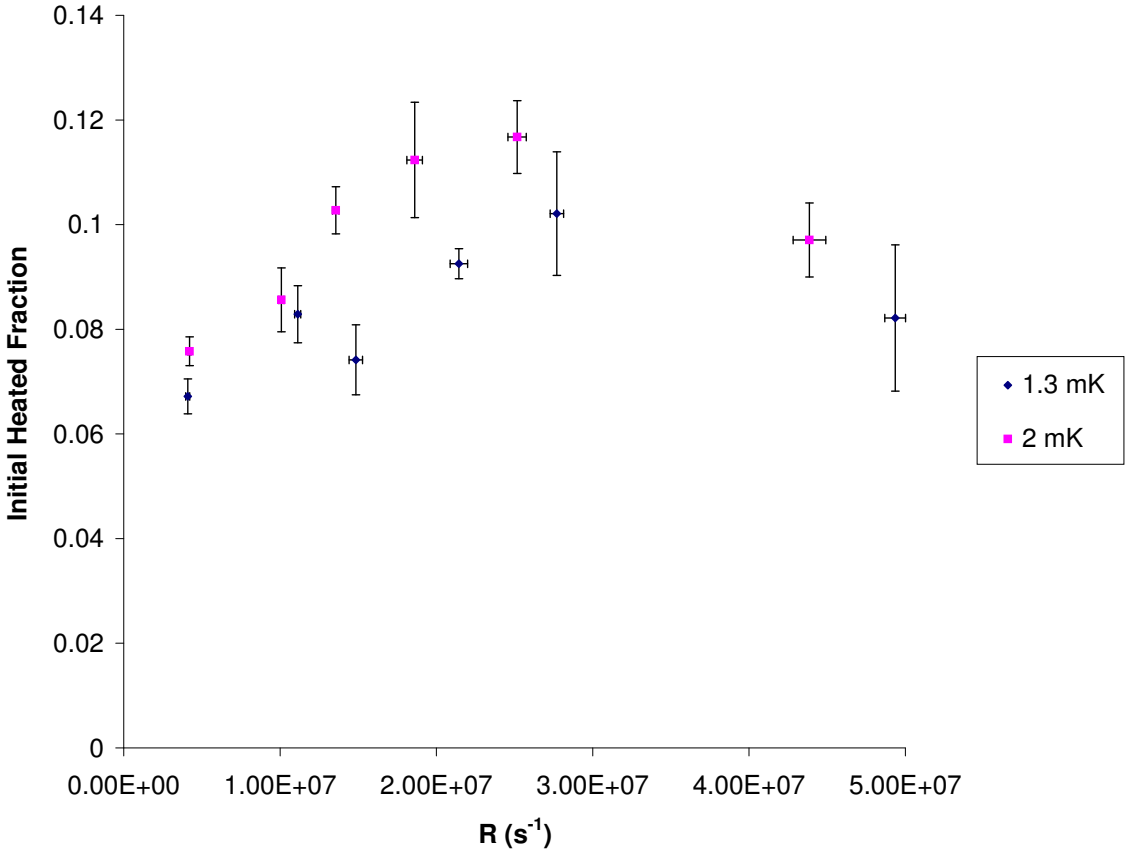

Figure 6.11: Plot of the relationship between $F_H(t=0)$ initial fraction and MOT loading rate R for a 1.30 ± 0.14 mK trap and 2.00 ± 0.22 mK trap (set using continuous RF knife sweeps with lower frequencies 27.53 and 42.72 MHz, respectively). E_{mid} was set to 0.667 ± 0.053 mK. These data points were determined by performing Gnuplot best fits on F_H curves taken over a number of R values.

Table 6.2: Table of Gnuplot fit results for the relationship between F_H rate (denoted F'_H) and MOT loading rate R, for Fig. 6.10. The leftmost 2 mK point was not used in the best fit of the 2 mK data. The relationship between $d\langle E\rangle/dt$ (denoted $\langle E'\rangle$) and MOT loading rate R is also given for each trap in accordance with Eq. 6.4.

Trap Depth (mK)	$dF'_H/dR \times 10^{-7}$	$F'_H(R=0)$	$d\langle E'\rangle/dR$ (μK s^{-2})
1.30 ± 0.14	0.0086 ± 0.0013	-0.00035 ± 0.00080	5.60 ± 1.1
2.00 ± 0.22	0.01183 ± 0.00095	0.0071 ± 0.0013	11.8 ± 1.6

The best fit slopes on Fig 6.10 can be converted to a measure of how $d\langle E\rangle/dt = E'$ changes with R:

$$E' = \frac{d\langle E'\rangle}{dR} R. \tag{6.4}$$

6.4 Measurement of Pure State Loss Rate vs. Rb Pressure

With the Zeeman pumping system, we could determine loss rates without having to consider the ambiguity of trapping multiple $|F\, m_F\rangle$ states in a single magnetic trap. Initial loss rate comparisons taken in December gave the loss rate of ^{85}Rb $|3\,3\rangle$ as 5.4 times greater than $|2\,-2\rangle$ (in a magnetic trap of the same trap depth), and the loss rate of ^{87}Rb$|1\,-1\rangle$ as 1.4 times greater than $|2\,2\rangle$ [5].

We elected to create experimental plots of loss rates of ^{85}Rb $|3\,3\rangle$ and $|2\,-2\rangle$, and ^{87}Rb $|2\,2\rangle$ and $|1\,-1\rangle$, against R, the MOT loading rate [2]. Because R is linearly proportional to the not-measurable Rb background density (Eq. 3.2), the slope of a Γ vs. R plot would be proportional to $\langle\sigma v\rangle$, which multi-channel collisions have shown is independent of hyperfine state [21].

Magnetic trap loss curves at varying values of R were taken at trap depth, for all states, of $\sim$2.8 mK. R was varied by injecting Rb into the system and utilizing the equilibration process to reduce Rb number density in the system over time. The ^{85}Rb rates were measured in February, while the ^{87}Rb was measured in March. The result was a linear relationship (as expected) between Γ and R for all hyperfine states. These plots were all analyzed with linear best fits in Gnuplot. The results are graphed in Figs. 6.12 and 6.13, and best fit values are in Table 6.3.

6.5 Anomalous Results

While data was being taken, two anomalous results were observed. The first is a slight decrease in loss rates in state ^{87}Rb $|1\,-1\rangle$ when Zeeman pumping is being used compared to when Zeeman pumping is not used (only $|1\,-1\rangle$ is trappable for ^{87}Rb $|F=1\rangle$). This decrease seems to vary between days, and can be anywhere from less than 10% up to 30%. It does not seem to vary

[2] Because one of the turbomolecular pumps had failed, the only background gas that was available at the time was Rb, and once the pump system was restored, the use of Rb had already been decided.

Table 6.3: Table of Gnuplot linear best fit results for data plotted in Figs. 6.12 and 6.13. Within error, the slopes of both states match for both ^{85}Rb and ^{87}Rb, as predicted by numerical calculation.

Hyperfine State	$d\Gamma/dR$	$\Gamma(R=0)$
^{85}Rb $\|3\,3\rangle$	0.01975 ± 0.00052	0.0773 ± 0.0040
^{85}Rb $\|2\,-2\rangle$	0.02061 ± 0.00042	0.0036 ± 0.0028
^{87}Rb $\|2\,2\rangle$	0.04763 ± 0.00089	0.0163 ± 0.0016
^{87}Rb $\|1\,-1\rangle$	0.04686 ± 0.00040	0.02021 ± 0.00058

monotonically with trap depth. While energy distribution experiments have shown that Zeeman pumping imparts additional energy into the trap, a hotter ensemble should be lost more quickly and not more slowly. It is unknown if the same effect occurs for other trappable hyperfine states: ^{87}Rb $|1\,-1\rangle$ is the only state where only one $|F\,m_F\rangle$ state is trapped regardless of whether or not Zeeman pumping is used, and so no other states could be tested. Zeeman pumping was used for all states in the measurements of Γ vs. R in section Section 6.4, and so the results from that section presumably are not affected by this phenomenon.

The second is a rapid initial loss of atoms that occurs over the span of approximately two seconds whenever the RF knife and Zeeman pumping are used in tandem (and not seen within noise when only the RF knife or Zeeman pumping is in use). This loss was initially seen in ^{85}Rb, and it was assumed to be due to the atoms having to undergo multiple RF transitions before entering into an untrappable $|F\,m_F\rangle$ state. It, however, can also be observed for ^{87}Rb $|1\,-1\rangle$, as seen in Fig. 6.14. The rate and degree of initial loss varies with current, but the long-term losses are not affected. Attempts were made at subtracting the long-term decay curve from the experimental data, and fitting the resulting clean short-term losses with exponential decays in order to determine the loss rate Γ_{RIL} of these curves. The noise in the subtracted data is high, and the determined Γ_{RIL}s did not within error show any dependence on current (see Fig. 6.15).

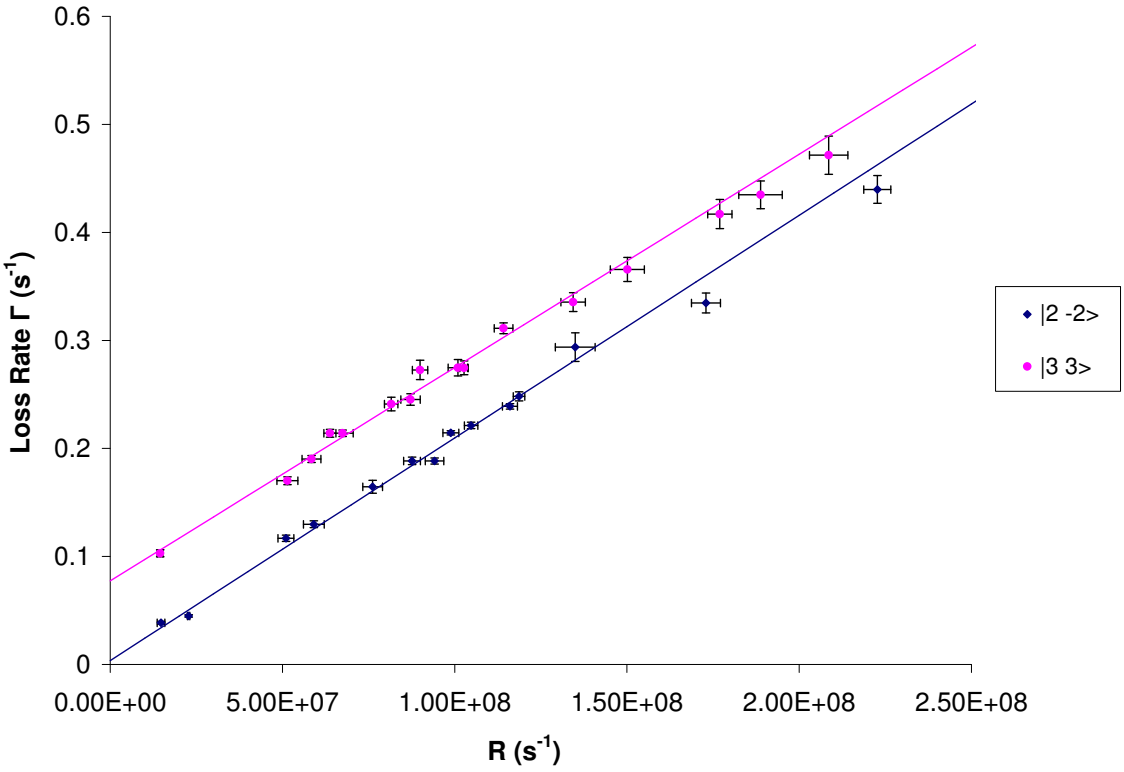

Figure 6.12: Plot of total loss rate Γ vs. MOT loading rate R for ^{85}Rb $|3\,3\rangle$ and $|2\,-2\rangle$ in magnetic traps. Trapping current was set to 2.2 A (a 2.83 ± 0.77 mK trap) for $|3\,3\rangle$, and 3.4 A (a 2.83 ± 0.74 mK trap) for $|2\,-2\rangle$. The RF knife was not used. While there is a y-intercept ($\Gamma(R=0)$) difference between the two lines, their slopes are identical, within error. Linear best fits determined using Gnuplot have been plotted alongside experimental data.

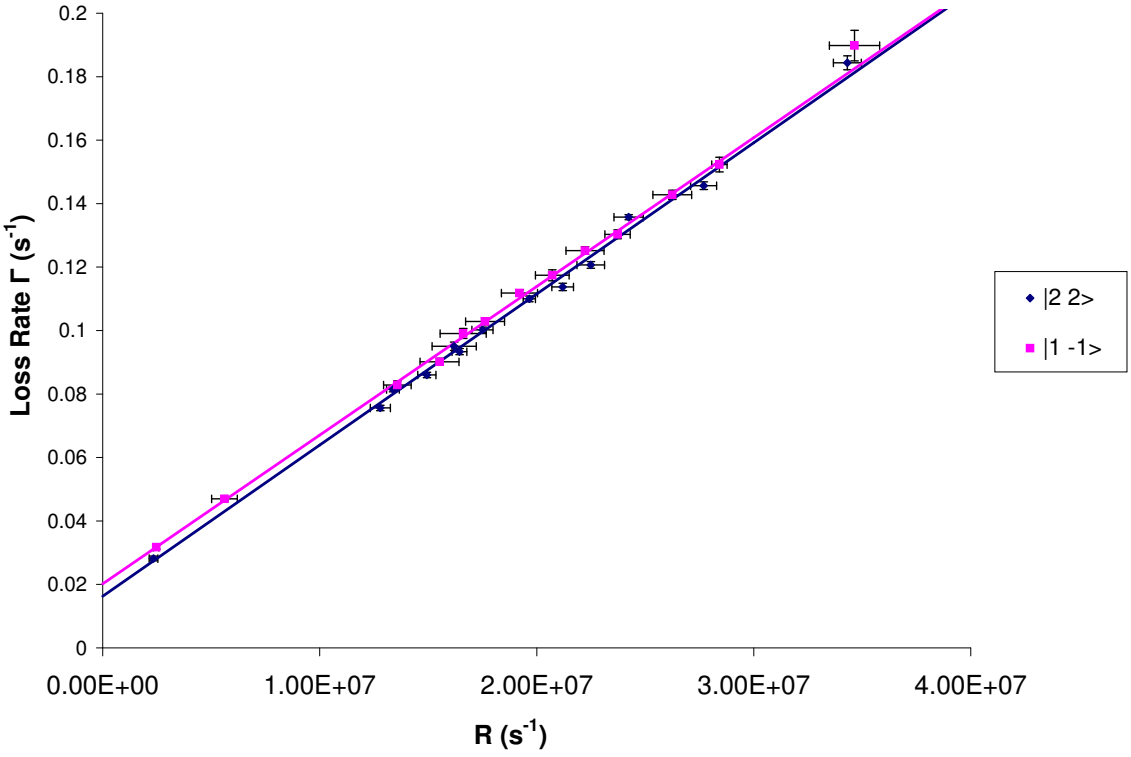

Figure 6.13: Plot of total loss rate Γ vs. MOT loading rate R for ^{87}Rb $|2\,2\rangle$ and $|1\,-1\rangle$ in magnetic traps. Trapping current was set to 4.53 A (a 2.83 ± 0.74 mK trap) for $|1\,-1\rangle$, and 2.2 A (a 2.83 ± 0.77 mK trap) for $|2\,2\rangle$. The RF knife was not used. While there is small a y-intercept ($\Gamma(R=0)$) difference between the two lines, their slopes are identical, within error. Linear best fits determined using Gnuplot have been plotted alongside experimental data.

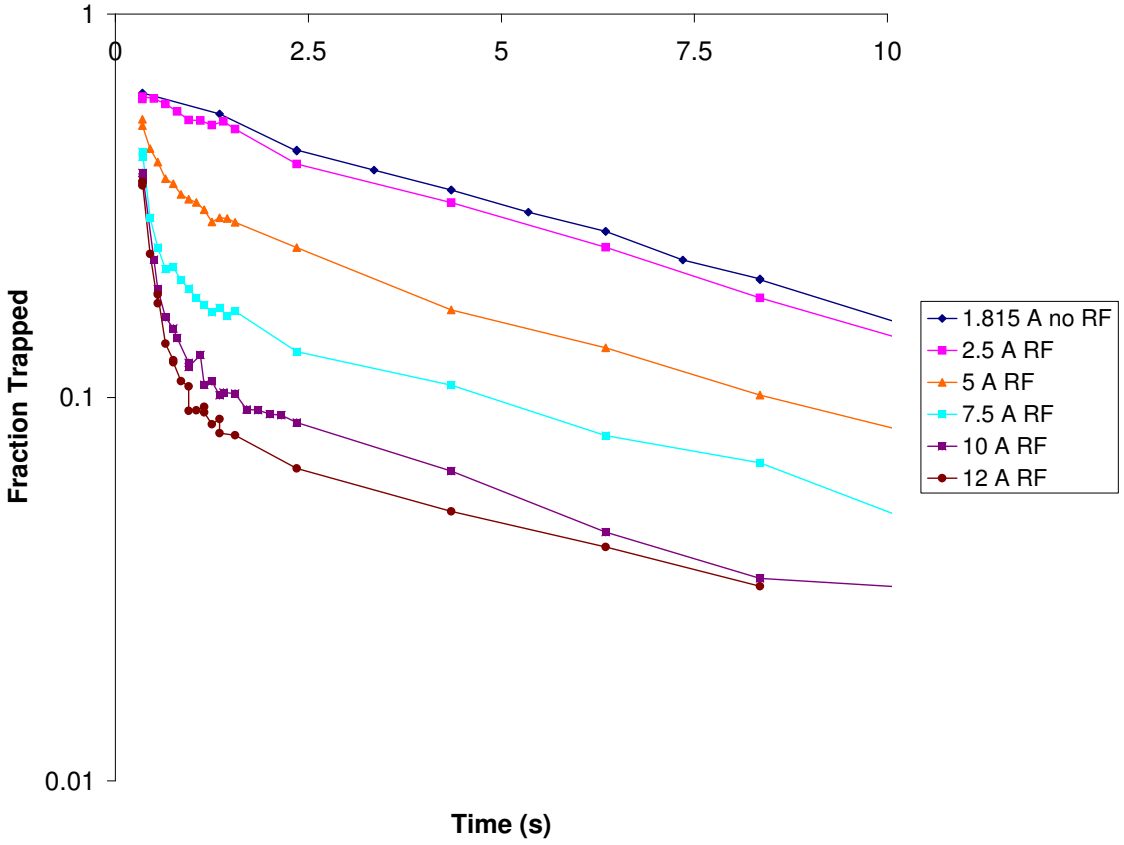

Figure 6.14: An investigation into rapid intial losses from an ^{87}Rb $|1,-1\rangle$ magnetic trap. The trap depth is kept either at 1.00 ± 0.15 mK using the magnetic coils alone at 1.815 A, or at 1 mK using a combination of an RF sweep from 21.0944 MHz to 100 MHz and the magnetic coils at currents 2.5 A or higher. Long-term losses look identical, but a rapid initial loss can be seen for high-currents. Note that at 12 A the trapped fraction reduces to just a few percent in under 2 seconds - this does not occur in an identical trap (using RF sweeping to hold the trap depth) where Zeeman pumping is not used!

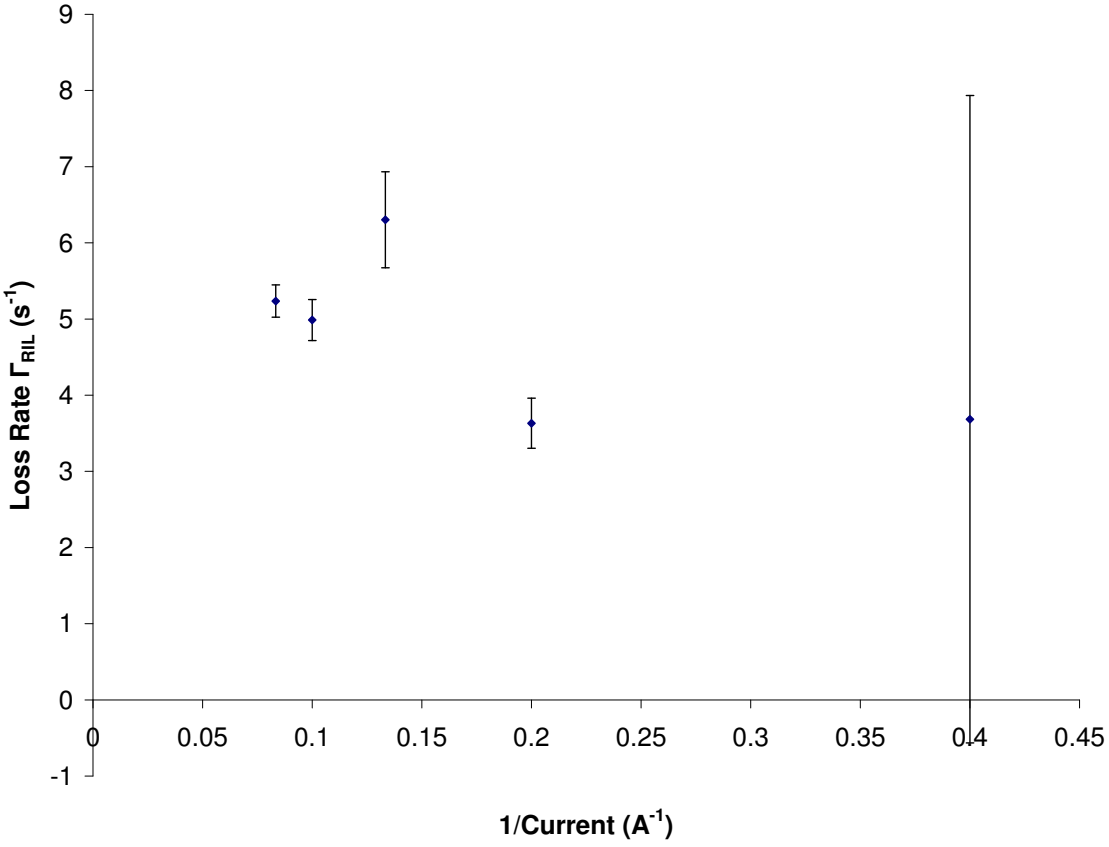

Figure 6.15: A plot of Γ_{RIL}, obtained by fitting exponential decays to the fast initial losses, as a function of A^{-1} (instead of A; see Section 7.3). Unfortunately, the resulting data is ambiguous, but does seem to suggest no dependence of Γ_{RIL} on A^{-1}.

Chapter 7

Discussion

7.1 Measurement of Heated Fraction

The measurements of heating presented in Section 6.3 are internally consistent. For example, the ratio of best fit slopes presented in Table 6.2, 1.4, is consistent, within error, with how heated fraction rate increases with trap depth, seen in Fig. 6.7. They are also consistent, qualitatively, with the theory presented in Chapter 2. We expect that the heated fraction rate dF_H/dt should increase with trap depth, since an increase in trap depth is equivalent to an increase in θ_{min}, which would result in more collisions being heating collisions. Heated fraction rate should also scale with background Rb pressure, as the rate at which Rb-Rb collisions occur is linearly proportional to background Rb.

The crude estimates of $d\langle E\rangle/dt$ indicate that we are in the regime of several μK of heating per second. Of course, as we do not know the Rb pressure in the system, we cannot know if this value truly makes sense compared to other magnetic traps. We are currently investigating various methods to determine Rb background number density.

The fact that $F_H(t=0) \neq 0$ is not easily explainable. It appears to scale with trap depth, but its relation to Rb pressure is, by Fig. 6.11, either significantly more complicated or nonexistent. If it is nonexistent, then $F_H(t=0) \neq 0$ would appear to be a phenomenon related to the trapped atoms rather than background collisions. It is possible the RF knife is not entirely effective in clearing out atoms in 125 ms. Very recent experiments with RF knife sweeping suggest that sweeping from 0 - 100 MHz (which was done to determine the 125 ms interval) may be more effective at clearing atoms than sweeping from 10 - 100 MHz or 20 - 100 MHz. If, however, initial heated fraction does increase with Rb pressure (the left half of Fig. 6.11 could be interpreted in this way), it may be due to low-angle collisions moving a small group of atoms just past E_{cut}. It is important to note that in our measurements the trap is allowed to evolve for a small amount of time before measurements are taken, which may be enough time for these low-angle collisions to shift the energy distribution in the trap.

Unfortunately, heated fraction is a value that has a very complex dependency to the various parameters we set in the trap. It depends on how (at what frequency) the initial cut of energetic atoms is performed, the trap depth of the magnetic trap, and, most importantly, the distribution of energies possessed by the trapped atoms at any given time. It is therefore prohibitive to attempt an analytical derivation of the various dependencies of heated fraction.

Rb-Rb collisions were chosen as the heating collisions to be investigated in our trap. This is because the quantum diffractive turn-off of the Rb-Rb $\langle \sigma v \rangle$ vs. trap depth plot occurs near 1 mK, easily accessible by our magnetic traps and RF knife, which allows us to create traps where a substantial number of collision are heating collisions. The Rb-Ar turn-off is near 10 mK, which is barely reachable by the magnetic coils and unreachable by the RF knife. It may be prudent, however, for future heating work to include experimenting with Rb-Ar collisions not only because results with a second type of collision can support the theory of heating presented in this thesis, but also because it is possible to measure Ar background number density.

The most important next step to studying heated fraction is the creation of the numerical magnetic trap simulator detailed in Section 5.2. As stated earlier, heated fraction is a value that has a very complex dependencies to trap parameters, and this is also true of the relationship between heated fraction and the exact $d\langle E \rangle / dt$ for the magnetic trap, which is ultimately what is desired when measuring trap heating. For this reason, the most effective method of corroborating experimentally determined heated fraction with the elastic scattering theory presented in Chapter 2 is to simulate the evolution of trap energy over time.

7.2 Measurement of Pure State Loss Rate vs. Rb Pressure

From Table 6.3, we can definitively say that the $\langle \sigma v \rangle$ of ^{85}Rb $|3\,3\rangle$ and $|2\,-2\rangle$ are the same, within error. The $\langle \sigma v \rangle$ of ^{87}Rb $|2\,2\rangle$ and $|1\,-1\rangle$ are also the same within error. The differences in loss rates can be explained by a difference in the values of $\Gamma(R=0)$. The initial measurements using Zeeman pumping taken in December are somewhat consistent with this picture. The December data was taken at low R values (corresponding to low Rb background number density), and the ratio of $\Gamma(R=0)$ $|3\,3\rangle$ and $|2\,-2\rangle$ is 21.5, meaning that a factor of 5 difference is easily accomodated. This is not the case for ^{87}Rb: the ratio of $\Gamma(R=0)$ $|2\,2\rangle$ and $|1\,-1\rangle$ is 1.24, and 1.4 is larger than the one-sigma error for this ratio. It could simply be experimental error, but it is also possible that $\Gamma(R=0)$ has changed over time.

We cannot easily compare between isotopes; loading rate R is state-specific, whereas Rb-Rb $\langle \sigma v \rangle$ is between the trapped ensemble and all background Rb. The Rb source for the MOT produces the natural abundance isotope ratio of 2.5932 ± 0.0020 ^{85}Rb for every ^{87}Rb, which suggests that for any trap depth the slope of Γ vs. R for ^{87}Rb should be 2.59 times larger than for ^{85}Rb [1]. From our data, the ratio is 2.341 ± 0.046, close to, but not within error of, 2.5932 ± 0.0020.

While we have experimentally verified our theory on calculating $\langle \sigma v \rangle$, the difference in the

intercept, $\Gamma(R=0)$, remains a mystery. Archival Rb-Ar Γ vs. n_{Ar} data also shows (although not as definitively, since Zeeman pumping had yet to be installed) that while $\langle\sigma v\rangle$ does not change regardless of the hyperfine state being trapped, there are intercept differences. If it is the case that there is a hyperfine dependence for $\langle\sigma v\rangle$ of elastic collisions between trapped Rb and some other background constituent M, the difference in intercept between any two hyperfine states should vary with trap depth, and a plot of this variance should follow the $\langle\sigma v\rangle$ vs. trap depth curve of Rb-M collisions. Alternatively, the reason for the y-intercept difference may be a hitherto unconsidered loss mechanism.

As an aside, it is notable that a Γ vs. R plot could be used to determine the Rb background number density in the system, provided we trust our numerical calculations (Fig. 1.2) and experimental data. Since the slope of such a graph is $\alpha\langle\sigma v\rangle$, where α is some coefficient, and we theoretically know $\langle\sigma v\rangle$, the conversion between R and number density should be α. For a trap at 2.83 mK, the Rb-Rb $\langle\sigma v\rangle$ is 2.9279×10^{-9} cm^3 s^{-1}. Using this value to convert the x-axis for Figs. 6.12 and 6.13, we obtain Figs. 7.1 and 7.2

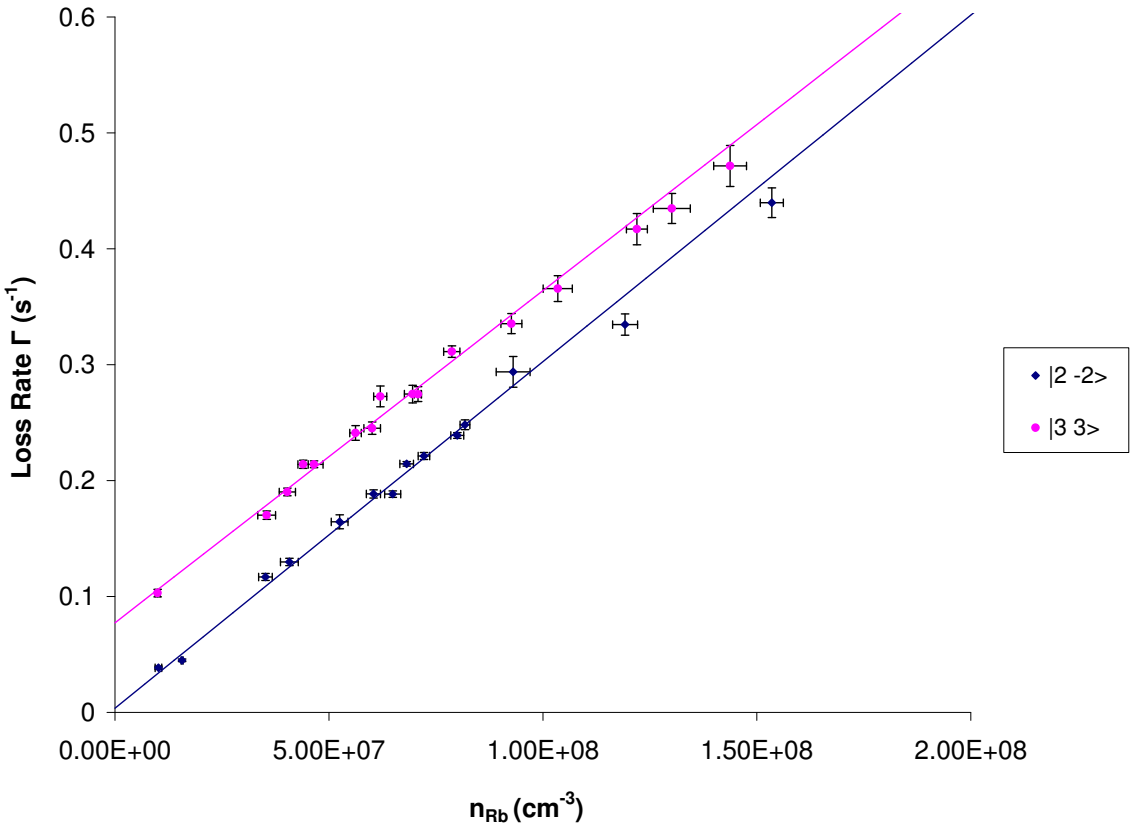

Figure 7.1: Fig. 6.12 with the x-axis rescaled ($\alpha = 0.6893$) from MOT loading rate R to Rb background number density.

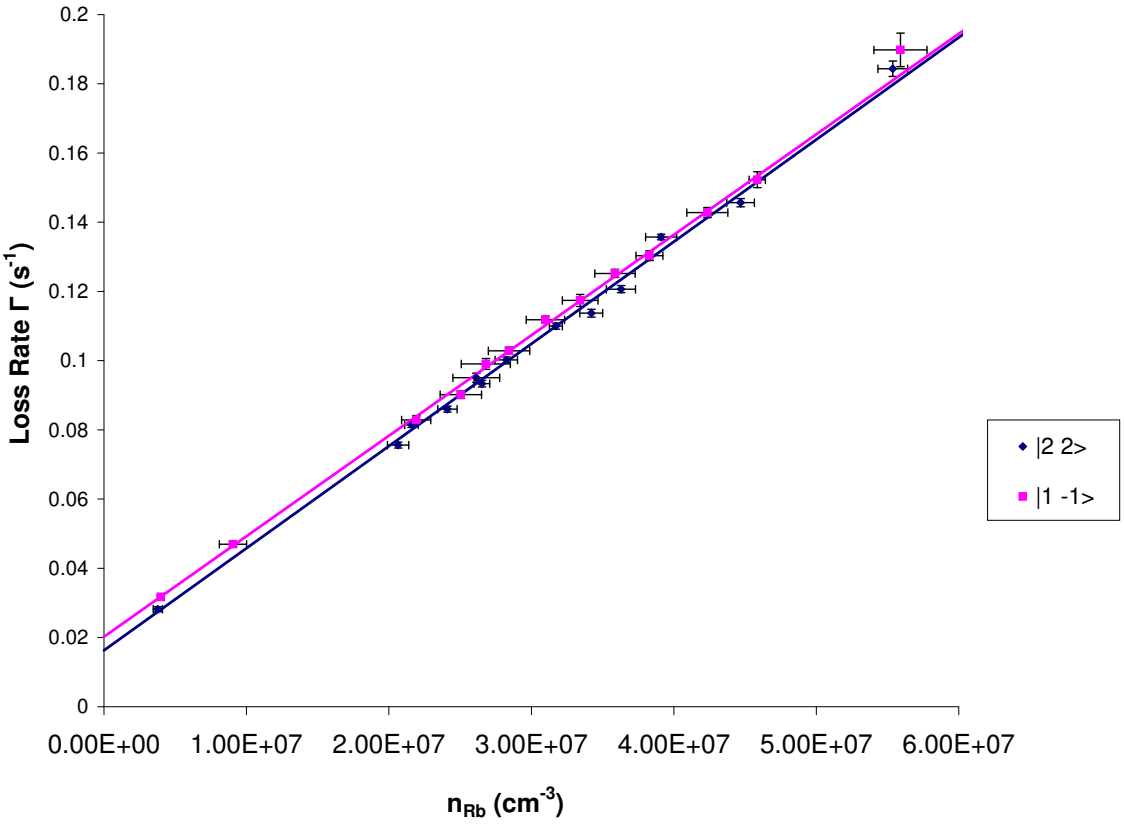

Figure 7.2: Fig. 6.13 with the x-axis rescaled ($\alpha = 1.6138$) from MOT loading rate R to Rb background number density.

7.3 Anomalous Results

One possibility for the anomalous results is Majorana losses. If this is the case, then Eq. 3.11 suggests that the loss rate should scale as the inverse of magnetic gradient. In our trap, this is equivalent to the inverse of current. As mentioned in Section 6.5, we fitted exponential decays to the fast initial losses seen in Fig. 6.14. We then plotted the loss rates from the exponential decays, Γ_{RIL}, versus A^{-1}. The results are ambiguous, as can be seen in Fig. 6.15. One problem with the Majorana loss explanation is that it should be seen when no Zeeman pumping is used. In fact, it should be *more* prominent, since Zeeman pumping is known to impart additional energy into the trap, would make it less likely for trapped atoms to explore the region near the magnetic zero. Experimental results have shown this is not the case, and these rapid initial losses are only prominent when the RF knife and Zeeman pumping operate in tandem.

Another potential explanation is that the Zeeman pumping system excites atoms to energies too high for the RF knife to initially reach. These energetic atoms will eventually (over 1 - 2 seconds) explore the trap and cross a position at which the RF knife can affect them. This is likely the case for 12 A traps, since the trap depth is actually higher than the effective upper limit of the RF knife at around 120 MHz. This cannot be the case, however, for 5 A traps, which can be cleaned in their entirety by the RF knife, and still exhibit rapid initial losses. In these cases, we hypothesize that the Zeeman pumping system can impart kinetic energy to atoms close to the centre of the trap. Atoms with enough energy to reach a potential where the RF knife induces transitions may not reach such potentials until it explores the trap for some time. More thorough testing is needed to determine if this hypothesis is indeed correct.

7.4 Conclusion

We investigated low scattering angle elastic collisions that change the trapped ensemble energy distribution without resulting in immediate trap loss, or "heating collisions", and the dependence of elastic collisional loss cross-sections on the hyperfine state of the trapped rubidium ensemble, in our MAT magnetic trap. Our results show that the average rate of energy imparted to a trapped atom in our system is on the order of 1 μK per second. We also show that the Rb-Rb loss rate slope $\langle \sigma v \rangle$ is invariant of hyperfine state, indicating that any loss dependency on hyperfine state rests with collisions with other species, or other forms of loss.

Chapter 8

Appendix

8.1 List of Data Files Used

The files that contain the data used in this thesis are listed below, for future reference.

- Figs. 1.1, 1.2 - CollisionThesis.xls
- Fig. 4.4 - RF Efficacy Thesis.xls
- Figs. 4.5, 4.6 - 6-25-09 F12 Init Thesis.xls and 10-16-09 F23 Init Thesis.xls
- Figs. 5.1, 5.2 - DCS Thesis.xls
- Figs. 6.3, 6.4 - 12-1-09 RF Data Thesis.xls
- Fig. 6.5 - 1-20-21-2010 Data Thesis.xls
- Table 6.1, Figs. 6.6, 6.7, 6.8, 6.9 - 3-11-10 Data Thesis.xls
- Table 6.2, Figs. 6.10, 6.11 - 3-25-10 Data Thesis.xls
- Table 6.3, Figs. 6.12, 6.13, 7.1, 7.2 - 2-24-25 Data Thesis.xls, 3-18-10 Data Thesis.xls
- Figs. 6.14, 6.15 - 3-10-10 Data Thesis.xls

Bibliography

[1] CRC Handbook of Chemistry and Physics, 90th ed., 2010. Internet Version. → pages 64

[2] M. Anderson, J. Ensher, M. Matthews, C. Wieman, and E. Cornell. Observation of Bose-Einstein Condensation in a Dilute Atomic Vapor. *Science*, 269(3), 1995. → pages 2

[3] S. Bali, K. O'Hara, M. Gehm, S. Granade, and J. Thomas. Quantum-diffractive background gas collisions in atom-trap heating and loss. *Phys. Rev. A*, 60(1), 1999. → pages 9, 11, 12, 38

[4] H. Beijerinck. Rigorous calculation of heating in alkali-metal traps by background gas collisions. *Phys. Rev. A*, 61(033606), 2000. → pages 11, 12

[5] J. Booth. Zeeman Pumping - Results from Dec. 5, 2009. Technical report, University of British Columbia, 2009. → pages 57

[6] P. Bouyer, V. Boyer, S. Murdoch, G. Delannoy, Y. le Coq, A. Aspect, and M. Lécrivain. RF-induced evaporative cooling and BEC in a high magnetic field. In *Bose-Einstein Condensates and Atom Lasers*. 2000. → pages viii, 22, 23, 24, 45

[7] A. Browaeys, A. Robert, J. Sirjean, S. Poupard, D. Nowak, D. Boiron, C. Westbrook, and A. Aspect. Thermalization of magnetically trapped metastable helium. *Phys. Rev. A*, 64 (034703), 2001. → pages 1, 45

[8] J. P. Burke. *Theoretical Investigation of Cold Alkali Atoms*. PhD thesis, University of Colorado, 1999. → pages 15

[9] E. Charron, M. Cirone, A. Negretti, J. Schmiedmayer, and T. Calarco. Theoretical analysis of the implementation of a quantum phase gate with neutral atoms on atom chips. *Phys. Rev. A*, 74(012308), 2006. → pages 2

[10] M. Child. *Molecular Collision Theory*. Dover Publications, Inc., Mineola, New York, 1974. → pages 6, 12

[11] B. Desruelle, V. Boyer, S. Murdoch, G. Delannoy, P. Bouyer, and A. Aspect. Interrupted evaporative cooling of ^{87}Rb atoms trapped in a high magnetic field. *Phys. Rev. A*, 60(3), 1999. → pages 22

[12] P. Djuricanin. Magnetic Coil: Assembly and Instruction Manual. Technical report, University of British Columbia, 2009. → pages 27, 32

[13] D. Fagnan. Study of Collision Cross Section of Ultra-Cold Rubidium using a Magneto-Optic and pure Magnetic Trap, 2009. Undergraduate thesis, University of British Columbia. → pages viii, 1, 3, 7, 12, 16, 17, 18, 20, 22, 27, 28, 31, 34, 37

[14] D. Fagnan, J. Wang, C. Zhu, P. Djuricanin, B. Klappauf, J. Booth, and K. Madison. Observation of quantum diffractive collisions using shallow atomic traps. *Phys. Rev. A*, 80 (022712), 2009. → pages 2, 3, 6, 13

[15] R. Folman, P. Krüger, J. Schmiedmayer, J. Denschlag, and C. Henkel. Microscopic Atom Optics: From Wires to an Atom Chip. *Adv. At., Mol., Opt. Phys.*, 48, 2002. → pages 2

[16] D. J. Griffiths. *Introduction to Quantum Mechanics*. Pearson Prentice Hall, Upper Saddle River, New Jersey, 2nd edition, 2005. → pages 12, 13, 14, 19, 22

[17] B. Klappauf. zeeman_module.py, 2009. Python code. → pages viii, 21

[18] R. Krems. Re: C12 Value for Rb-Rb, 2010. Private communications (e-mail), March 16. → pages 39

[19] K. Ladouceur. Experimental Advances Toward a Compact Dual-Species Laser Cooling Apparatus. Master's thesis, University of British Columbia, 2008. → pages 27, 31

[20] Z. Li. *New mechanisms for external field control of microscopic interactions in ultracold gases*. PhD thesis, University of British Columbia, 2009. → pages 15

[21] Z. Li. Trap loss rates for ^{85}Rb cold gases, 2010. QDG/Theory Group Meeting, February 25th. → pages 40, 57

[22] R. Long, T. Steinmetz, P. Hommelhoff, W. Hansel, T. Hansch, and J. Reichel. Magnetic Microchip Traps and Single-Atom Detection. *Phil. Trans. R. Soc. Lond. A*, 361, 2003. → pages 2

[23] N. Marković. Notes on Scattering Theory. Chalmers University of Technology, 2003. → pages 12, 13, 14, 15, 37

[24] H. J. Metcalf and P. van der Straten. *Laser Cooling and Trapping*. Spring-Verlag, New York, New York, 1999. → pages 1, 16, 17

[25] T. P. Meyrath. *Experiments with Bose-Einstein Condensation in an Optical Box*. PhD thesis, University of Texas at Austin, 2005. → pages 22

[26] NIST. Fundamental Physical Constants from NIST, 2006. Available online at http://physics.nist.gov/cuu/Constants/index.html. → pages vi, 6

[27] S. Patil and K. Tang. Multipolar polarizabilities and two- and three-body dispersion coefficients for alkali isoelectronic sequences. *J. Chem. Phys.*, 106(6), 1997. → pages 38

[28] D. A. Steck. Rubidium 85 D Line Data (revision 2.1.1), 2009. Available online at http://steck.us/alkalidata. → pages 19

[29] D. A. Steck. Rubidium 87 D Line Data (revision 2.1.1), 2009. Available online at http://steck.us/alkalidata. → pages 19

[30] G. K. Woodgate. *Elementary Atomic Structure*. Oxford University Press, New York, New York, 2nd edition, 1983. → pages 19, 22